PUBLICATIONS OF THE ASTRONOMICAL SOCIETY OF THE PACIFIC, **117**:1049–1112, 2005 October


# The Photometric Performance and Calibration of the *Hubble Space Telescope* Advanced Camera for Surveys

M. SIRIANNI,[1,2,3] M. J. JEE,[3] N. BENÍTEZ,[3,4] J. P. BLAKESLEE,[3] A. R. MARTEL,[3] G. MEURER,[3] M. CLAMPIN,[5] G. DE MARCHI,[1,2,6] H. C. FORD,[3] R. GILLILAND,[2] G. F. HARTIG,[2] G. D. ILLINGWORTH,[7] J. MACK,[2] AND W. J. MCCANN[3]

*Received 2004 December 2; accepted 2005 July 6; published 2005 September 27*

**ABSTRACT.** We present the photometric calibration of the Advanced Camera for Surveys (ACS). The ACS was installed in the *Hubble Space Telescope* (*HST*) in 2002 March. It comprises three cameras: the Wide Field Channel (WFC), optimized for deep near-IR survey imaging programs; the High Resolution Channel (HRC), a high-resolution imager that fully samples the *HST* point-spread function (PSF) in the visible; and the Solar Blind Channel (SBC), a far-UV imager. A significant amount of data has been collected to characterize the on-orbit performance of the three channels. We give here an overview of the performance and calibration of the two CCD cameras (WFC and HRC) and a description of the best techniques for reducing ACS CCD data. The overall performance is as expected from prelaunch testing of the camera. Surprises were a better-than-predicted sensitivity in the visible and near-IR for both the WFC and HRC and an unpredicted dip in the HRC UV response at ~3200 Å. On-orbit observations of spectrophotometric standard stars have been used to revise the prelaunch estimate of the instrument response curves to best match predicted and observed count rates. Synthetic photometry has been used to determine zero points for all filters in three magnitude systems and to derive interstellar extinction values for the ACS photometric systems. Due to the CCD internal scattering of long-wavelength photons, the width of the PSF increases significantly in the near-IR, and the aperture correction for photometry with near-IR filters depends on the spectral energy distribution of the source. We provide a detailed recipe to correct for the latter effect. Transformations between the ACS photometric systems and the *UBVRI* and WFPC2 systems are presented. In general, two sets of transformations are available: one based on the observation of two star clusters; the other on synthetic photometry. We discuss the accuracy of these transformations and their sensitivity to details of the spectra being transformed. Initial signs of detector degradation due to the *HST* radiative environment are already visible. We discuss the impact on the data in terms of dark rate increase, charge transfer inefficiency, and "hot" pixel population.

*Online material*: color figures

## 1. INTRODUCTION

The Advanced Camera for Surveys (ACS) was installed in the *Hubble Space Telescope* (*HST*) on 2002 March 7, during Servicing Mission 3B, in the axial bay previously occupied by the Faint Object Camera. ACS was built in a collaborative effort between the Johns Hopkins University, Ball Aerospace and Technologies Corporation, the NASA Goddard Space Flight Center (GSFC), and the Space Telescope Science Institute (STScI). The description of the camera and the philosophy underlying its design are presented in Ford et al. (1998, 2002). The status and the on-orbit performance of the camera are described in Clampin et al. (2002). An overview of the capabilities of ACS is provided in the ACS Instrument Handbook (Pavlovsky et al. 2004, hereafter AIHv5).

The ACS consists of three channels: the Wide Field Channel (WFC), the High Resolution Channel (HRC), and the Solar Blind Channel (SBC). The WFC and HRC have separate optical paths and mirrors (Fig. 1). The WFC is a high-throughput, wide-field imager (202″ × 202″) designed for deep imaging surveys in the optical and near-IR. The WFC provides a factor of 10 gain in discovery efficiency (throughput × field of view) at 8000 Å, compared to the Wide Field Planetary Camera 2 (WFPC2). The primary goal of the WFC design is to maximize the camera throughput in the near-IR, and this has been achieved by using only three reflective optics and by coating the mirrors with Denton protected silver. This configuration provides a reflectivity 50% higher than three aluminum-coated

[1] European Space Agency, Research and Scientific Support Department.
[2] Space Telescope Science Institute, 3700 San Martin Drive, Baltimore, MD 21218.
[3] Department of Physics and Astronomy, Johns Hopkins University, 3400 North Charles Street, Baltimore, MD 21218.
[4] Istituto de Astrofísica de Andalucía, Camino bajo de Huétor 24, Granada 18008, Spain.
[5] NASA Goddard Space Flight Center, Code 681, Greenbelt, MD 20771.
[6] Current address: ESA, Astrophysics Division, Keplerlaan 1, 2200 AG Noordwijk, Netherlands.
[7] UCO/Lick Observatory, University of California, Santa Cruz, CA 95064.

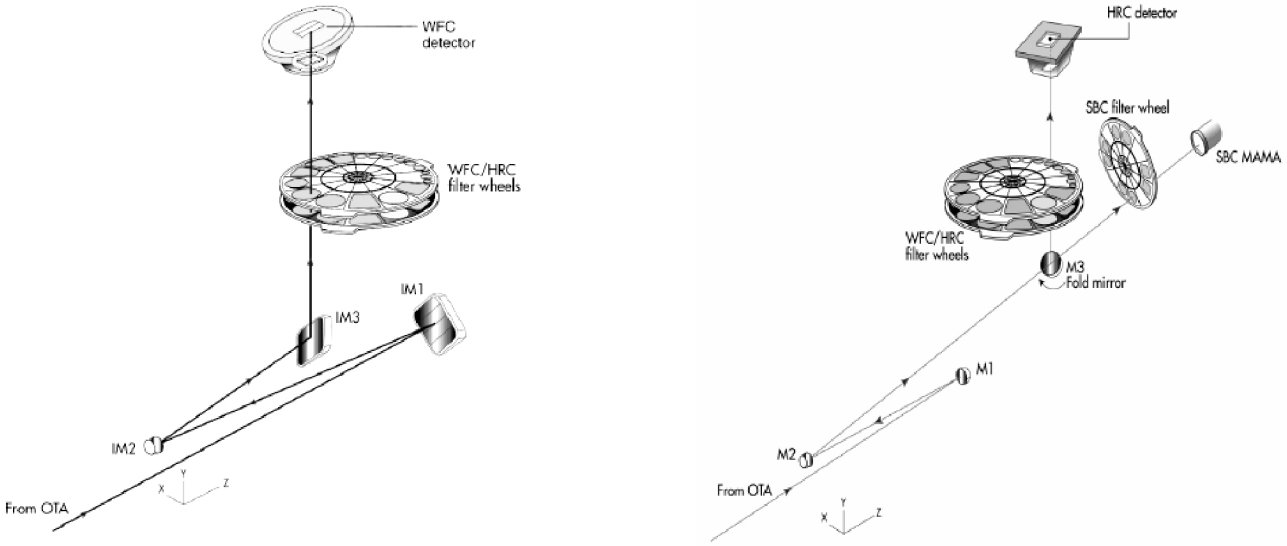


FIG. 1.—Schematic of the optical design for the WFC (*left*) and HRC/SBC (*right*).

mirrors would provide at 800 nm. The three mirrors are designated IM1, IM2, and IM3. The light from the Optical Telescope Assembly (OTA) first encounters IM1, a spherical mirror that images the *HST* pupil onto the IM2. This mirror is an anamorphic asphere figured with the inverse spherical aberration of the *HST* primary mirror, and thus corrects the spherical aberration in the *HST* primary mirror and the field-dependent astigmatism of the *HST* at the center of the WFC field of view (FOV). The light from the IM2 mirror is reflected by a Schmidt-like plate (IM3) through the two filter wheels to the WFC CCDs. The Schmidt plate corrects the astigmatism over the WFC FOV.

In the near-UV (<3700 Å), the reflectivity of the silver coating falls rapidly and sets the lower limit of the spectral range observable with the WFC at about 3000 Å. The f/25 focal length of the WFC gives a plate scale of 0.″05 pixel$^{-1}$ and a near-critical sampling in the *I* band. The focal plane detector array is a mosaic of two Scientific Imaging Technologies (SITe) 2048 × 4096 15 $\mu$m CCDs (Clampin et al. 1998; Sirianni et al. 2000, 2003, 2004). The two CCDs, although physically separated in the focal plane, have been cut from the same silicon wafer and have gone through similar postmanufacturing processes. There is therefore a significant continuity in responsivity across the focal plane array.

The HRC is a near-UV to near-IR high-resolution f/70 imager, which provides critically sampled images in the visible over a 29″ × 26″ field of view, with a resolution of 0.″025 pixel$^{-1}$.

The HRC optical design employs three aluminum-coated mirrors with an $MgF_2$ overcoating. Two mirrors, M1 and M2, shared with the SBC, have a coating optimized for maximum reflectivity at 1216 Å. M2 is an anamorphic asphere figured with the inverse spherical aberration on the *HST* primary mirror, to correct the spherical aberration in the *HST* primary mirror. The third mirror, M3, is a fold mirror with reflectivity optimized at wavelengths longer than 2000 Å, and it is inserted at 45° into the light path to redirect the beam through the two filter wheels to the HRC focal plane array. The HRC detector is a SITe 1024 × 1024 21 $\mu$m CCD (Clampin et al. 1998) based on the Space Telescope Imaging Spectrograph (STIS) CCD (Kimble et al. 1998).

The SBC is a far-UV imager optimized for high throughput at 1216 Å, with a 31″ × 35″ FOV and a plate scale of 0.″032 pixel$^{-1}$. In order to maximize far-UV throughput, the SBC optical design is a two-mirror system with its own independent filter wheel. The two mirrors are shared with the HRC. The SBC is selected when the fold mirror is moved out of the light beam. The SBC uses a STIS-based photon-counting detector with an opaque CsI photocathode Multi-Anode Microchannel Array (MAMA; Quijano et al. 2003).

More detailed descriptions of the instruments are available in a series of papers on an ACS Web page.[8]

In addition to the key design goal of each camera, the other main element that determines the quality of the science that ACS can produce is its filter complement. The complement of ACS filters and dispersers is described by Ford et al. (1996) and is listed in Tables 1 and 2. The ACS optical design allows

[8] See http://acs.pha.jhu.edu/instrument/papers.

TABLE 1
WFC FILTERS

| Filter | Pivot λ (Å) | Width (Å) | PHOTFLAM[a] (ergs s$^{-1}$ cm$^{-2}$ Å$^{-1}$) | Description |
|---|---|---|---|---|
| F435W ..... | 4317.398 | 293.47 | 3.141250E−19 | Johnson *B* |
| F475W ..... | 4744.356 | 420.11 | 1.808802E−19 | SDSS *g′* |
| F502N ..... | 5022.475 | 41.89 | 5.326231E−18 | [O III] |
| F550M ..... | 5581.205 | 163.27 | 3.860100E−19 | Narrov *V* |
| F555W ..... | 5359.547 | 360.02 | 1.955929E−19 | Johnson *V* |
| F606W ..... | 5917.678 | 672.31 | 7.906457E−20 | Broad *V* |
| F625W ..... | 6310.454 | 415.46 | 1.195394E−19 | SDSS *r′* |
| F658N ..... | 6584.015 | 37.15 | 1.999181E−18 | Hα |
| F660N ..... | 6599.374 | 35.53 | 5.347431E−18 | [N II] |
| F775W ..... | 7693.026 | 434.60 | 1.006545E−19 | SDSS *i′* |
| F814W ..... | 8059.761 | 654.64 | 7.072360E−20 | Broad *I* |
| F850LP ..... | 9054.768 | 539.43 | 1.507456E−19 | SDSS *z′* |
| F892N ..... | 8914.875 | 72.95 | 1.542548E−18 | Methane |

[a] Flux density per unit wavelength that generates 1 count s$^{-1}$.

both the WFC and HRC to share two filter wheels. These filter wheels are populated with 17 bandpass filters, a set of five linear ramp filters, a grism, a prism for the HRC, and three visible and three near-UV polarizers. The SBC has its own filter wheel with five long-pass filters, two prisms, a narrow-band Lyα filter, and four opaque positions that act as shutters. The CCD camera filter wheels contain filters of two different sizes. Some filters are full-sized and can be used with both the HRC and the WFC. Others are smaller, giving a full unvignetted FOV with the HRC, but a vignetted area of 72″ × 72″ when used with the WFC. Eleven filters are allocated to broadband imaging from the near-UV to the near-IR. This includes the Sloan *g* (F475W), *r* (F625W), *i* (F775W), and *z* (F850LP) filters.

The two near-UV high-throughput filters F220W and F250W are similar to the F218W and F255W currently in the WFPC2 and provide continuity between the two instruments. These are complemented by one set of broadband *U* (F330W), *B* (F435W), *V* (F555W), broad *V* (F606W), and *I* (F814W) filters, also similar to the WFPC2 filters. To complement these filters, there is a medium-band continuum filter, F550M, which is centered at ∼5500 Å, with a bandwidth of ∼10%.[9]

Narrowband filters for the CCD cameras in ACS take three forms: standard narrowband filters that cover the entire field of view of both cameras, linear ramp filters similar to those in WFPC2, and an HRC-size methane-band filter designed for the observation of the giant planets. The standard narrowband filter complement is Ne V (F344N), [O III] (F502N), Hα (F658N), and [N II] (F606N). The five ramp filters (four narrowband ∼2% and one broadband ∼9%) allow narrow- or medium-band imaging centered at an arbitrary wavelength. The ramp filters cover the wavelength region from ∼3700 Å to ∼1.05 μm. Each is divided into three strips covering ∼500 Å per segment. The desired bandpass is selected by a combination of target position and filter wheel rotation. The central strip of each of the five linear ramp filters can be used with the HRC. The transmittance curve for each filter are available from the authors online.[10] The total throughput curve, including the OTA and the ACS optical elements and detector quantum efficiency, are available via the ACS Web site.[11]

This paper presents data relevant to the photometric performance and calibration of the two CCD cameras of the ACS. Information on the SBC photometric performance is available

[9] When expressed in percentage, the FWHM transmittance is divided by the center wavelength of the band and multiplied by 100%

[10] See http://acs.pha.jhu.edu/instrument/filters/general/Master_Table.html.

[11] See http://acs.pha.jhu.edu/instrument/photometry.

TABLE 2
HRC FILTERS

| Filter | Pivot λ (Å) | Width (Å) | PHOTFLAM[a] (ergs s$^{-1}$ cm$^{-2}$ Å$^{-1}$) | Description |
|---|---|---|---|---|
| F220W ..... | 2255.426 | 187.28 | 8.113312E−18 | Near-UV broadband |
| F250W ..... | 2715.875 | 239.40 | 4.781345E−18 | Near-UV broadband |
| F330W ..... | 3362.675 | 173.82 | 2.236720E−18 | HRC *U* |
| F344N ..... | 3432.847 | 42.62 | 2.139635E−17 | Ne *V* |
| F435W ..... | 4310.986 | 309.68 | 5.368556E−19 | Johnson *B* |
| F475W ..... | 4775.740 | 418.81 | 2.937020E−19 | SDSS *g′* |
| F502N ..... | 5021.072 | 83.01 | 8.034045E−18 | [O III] |
| F550M ..... | 5579.729 | 168.05 | 5.985392E−19 | Narrov *V* |
| F555W ..... | 5355.946 | 357.19 | 3.020066E−19 | Johnson *V* |
| F606W ..... | 5887.935 | 664.88 | 1.278104E−19 | Broad *V* |
| F625W ..... | 6295.498 | 415.31 | 1.973001E−19 | SDSS *r′* |
| F658N ..... | 6581.980 | 162.69 | 3.357119E−18 | Hα |
| F660N ..... | 6582.439 | 468.30 | 8.976461E−18 | [N II] |
| F775W ..... | 7665.083 | 432.03 | 1.949664E−19 | SDSS *i′* |
| F814W ..... | 8115.338 | 703.45 | 1.269102E−19 | Broad *I* |
| F850LP ..... | 9145.236 | 538.95 | 2.286987E−19 | SDSS *z′* |
| F892N ..... | 8913.882 | 270.92 | 2.447032E−18 | Methane |

[a] Flux density per unit wavelength that generates 1 count s$^{-1}$.

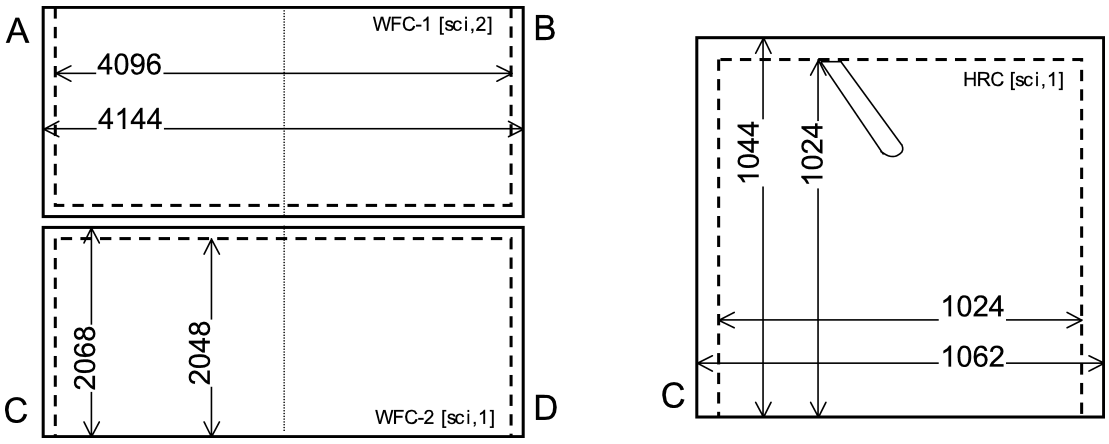


FIG. 2.—Structure of the WFC and HRC chips (not scaled). Dashed lines show the overscan regions; dotted lines show the quadrant division. The dimensions in pixels are shown. The gap between the two WFC chips is about 50 pixel wide. The position of the readout amplifiers used in the default configuration and the approximate size and position of the HRC Fastie finger are also shown.

in AIHv5, Tran et al. (2002a, 2002b), and Sirianni et al. (2002a). Section 2 presents a brief description of the WFC and HRC data and FITS file structure. In § 3 we describe the main steps of the ACS calibration pipeline at STScI, including a discussion of the accuracy of bias and dark subtraction, flat-field normalization, geometric distortion, and charge transfer efficiency. Section 4 describes the spatial variation of the point-spread function (PSF), the encircled energy profile, and the long-wavelength scattered light problem. The analysis of the variation of the encircled energy profile with the effective wavelength is used to estimate the aperture correction in all filters. Section 5 discusses the gain settings and the linearity and saturation of the CCDs. Section 6 presents the absolute flux calibration of ACS. The definition of the photometric system of ACS and the determination of the zero points are presented in § 7. In § 8 we present observed and synthetic photometric transformations between the WFC and the HRC. We also discuss transformations from the ACS photometric system to the *UBVRI* and WFPC2 systems. Sections 9 and 10 discuss the HRC UV red leak and the reddening in the ACS system, respectively. We inserted several sections in the Appendix to include material that can be useful to some readers who are also ACS users. We provide a cookbook for the calibration of point-source photometry, resolved object photometry, and surface photometry, and additional material for transformations to non-ACS photometric systems of stars and galaxy templates.

This document represents our understanding of the CCD cameras of the ACS as of spring 2005. Any of the discussions or results presented here could be subject to revision as our understanding of the ACS evolves.

## 2. ACS DATA FORMAT

The ACS Data Handbook (Pavlovsky et al. 2005, hereafter ADHv4) contains all the information needed to manipulate, process, and analyze data from the ACS. In this section we summarize the key elements of the ACS data structure.

### 2.1. WFC Data

Figure 2 shows a schematic of the WFC focal plane array and readout amplifiers. The WFC focal plane array consists of two mosaicked CCDs (WFC-1 and WFC-2). The imaging area of each of the two chips consists of 4096 columns, each containing 2048 pixels. Each pixel is 15 × 15 $\mu$m in size. The serial register, along one of the 4096 pixel edges of the device, is split in the middle so that the entire device can be read out through either one or both of the amplifiers that terminate each end of the serial register. There are 24 additional extended pixels (physical overscan) on each side of the serial readout register, just before each amplifier. The WFC raw data also contain a virtual overscan of 20 rows, obtained by overclocking after the readout of the last CCD row. In order to minimize the readout time and reduce the number of serial transfers, the default configuration is a 2 amp readout. Hence, each amplifier is used to read a single 2048 × 2048 quadrant. WFC-1 uses amplifiers A and B, and WFC-2 uses amplifiers C and D. The WFC detectors are operated in multi-pinned phase (MPP) mode. MPP is used to hold the signal charge away from the surface Si-$SiO_2$ interface, thus reducing the dark current rate, minimizing surface residual image effects, and providing better charge transfer efficiency. The WFC detectors are operated in MPP mode only during the integration and not during the readout. Ground testing demonstrated that this configuration allows a higher full-well capacity and provides better cosmetics.

The physical separation between the two CCDs is equivalent to 50 pixels, which corresponds to 2.″5. The structure of the data and data products of the ACS calibration pipeline (CALACS; Hack & Greenfield 2000) is based on the previous *HST* instruments' file format and consists of multiextension FITS

files that store science (SCI), data quality (DQ), and error (ERR) arrays. Since WFC data come from two CCD chips, they are treated as separate observations, with a specific SCI, DQ, and ERR array for each chip, and with both chips being stored in the same FITS file. Thus, the array SCI-1 in the FITS extension [1] stores data from WFC-2, and the SCI-2 array in the FITS extension [4] stores WFC-1 data. A more detailed description of the ACS file structure is available in ADHv4. At the end of the CALACS steps, when WFC data are drizzled to combine dithered[12] exposures and/or remove geometric distortion, both chips are included in a single FITS extension.

### 2.2. HRC Data

The imaging area of the HRC consists of 1024 columns, each with 1024 pixels 21 × 21 $\mu$m in size. This CCD has four output amplifiers, one at each end of the two serial registers. The array can therefore be divided into 512 × 512 quadrants to minimize the readout time. The default configuration is a single amplifier readout, namely amplifier C, which was selected for its lower read noise and better cosmetics. The HRC CCD is operated in MPP mode during integration time and readout. There are 19 additional extended pixels (physical overscan) on each side of the serial readout register. The HRC data also contain a virtual overscan; 20 rows on the top of the chip, obtained by overclocking the readout of the last CCD row. The structure of the HRC data is simple; a single HRC exposure comes from a single chip and has only three data extensions. One particularity of all HRC images is the presence of a finger-like shadow departing from one edge of the image (Fig. 2). This is the shadow of a fixed occulting mask, called the "Fastie finger," a 0.″8 wide, 5″ long reflecting finger permanently located at the CCD entrance window. This mask, together with the two coronagraphic circular stops that can be flipped in and out of the light path, constitutes the coronographic capability of the HRC (Krist et al. 2003b).

## 3. ACS DATA TREATMENT

ACS raw data are processed by the ACS calibration pipeline (CALACS) at the STScI. A detailed description of the individual calibration tasks in CALACS is available in ADHv4. Briefly, the CALACS pipeline consists of the following steps performed on the raw CCD scientific data.

1. Subtraction of the bias level.
2. Subtraction of a superbias frame.
3. Subtraction of a superdark frame.
4. Application of a flat field.
5. Cosmic-ray rejection of combined CR-split observations.

The SITe CCDs are very stable; ground testing has shown that their response does not change over time or after thermal cycling. As a consequence, the flat-fielding strategy for the ACS is the same as that adopted for WFPC2 (Holtzman et al. 1995a), which relies on well-characterized high signal-to-noise ratio (S/N) flat fields acquired through all filters during ground testing. Second-order adjustment of the ground flat fields are performed with limited on-orbit observations (see § 3.4). Additional calibration steps are performed using MultiDrizzle (Koekemoer et al. 2002),[13] which applies the correction of the geometric distortion of nondithered images and converts the data units from electrons to electron rates. When multiple dithered observations are available, MultiDrizzle runs the `drizzle` algorithm (Fruchter & Hook 2002) to register them into a single product. In the following sections, we briefly describe the main steps, as well as relevant instrumental effects not treated by the processing.

### 3.1. Subtraction of the Bias Level

#### *3.1.1. WFC*

Normal WFC images are read out using all four amplifiers; therefore, each 2K × 2K quadrant needs to be treated independently in the calibration process. All four amplifiers produce a horizontal ramp in the physical overscan (the region that serves to correct the bias level), extending up to 18 columns toward the active area (Sirianni et al. 2001). Consequently, for accurate bias subtraction, only the last six columns of the leading physical overscan (those adjacent to the active area) are used by CALACS to estimate the bias level of each amplifier. In CALACS, the `doblev` routine creates a $\sigma$-clipped average column of the selected area of the leading physical overscan, performs a linear fit along this column, and subtracts the bias level row by row, using a single fitted value for each. The virtual overscan is not used to estimate the bias level. This region shows large-scale structure that is quadrant and gain dependent. Due to the bias fixed pattern noise, this structure makes the use of the virtual overscan in an automatic routine problematic. Moreover, this region can be contaminated by deferred charge due to degradation in parallel charge transfer efficiency (see § 3.7).

An analysis of the active area in bias frames shows small differences in bias level between the leading physical overscan and the active area (Sirianni et al. 2002b). Ideally, no offset would be seen. This offset varies from amplifier to amplifier, and it can be as large as 3.5 ADU (analog-to-digital converter units).

In principle, if the residual offset between the imaging area and the overscan region were always of the same amplitude, a full-frame superbias subtraction (see § 3.2) would remove any residual difference. Unfortunately, the offset is not constant but shows random variations of the order of a few tenths of

[12] For a detailed description of the advantage of using a camera in *dithering* mode and of *drizzling* as an image-reconstruction technique, see Fruchter & Hook (2002).

[13] Until 2004 September, PyDrizzle (Hack et al. 2003) was used instead of MultiDrizzle.

an ADU. The cause of the residual offsets and their variation with time are still under investigation. They occur at a level below what could have been tested on the ground. They are likely the result of interference between the WFC integrated electronics module and the telescope and/or scientific instruments. The non-MPP readout mode could also play a role. The accuracy of the bias-level subtraction in a single quadrant is limited by this random effect.

The difference between these two bias levels (i.e., the amplitude of the residual offset level) varies between quadrants. Since the bias level is measured in the leading physical overscan and subtracted from the active area of each quadrant, the center of the resulting image shows a "jump" between two adjacent quadrants. This offset is present in all calibration and science frames. Therefore, science images, after bias and dark subtraction, may show a quadrant-to-quadrant jump as large as a few ADUs (see Fig. 1 in Sirianni et al. 2002b). For point-source photometry, the local background is typically subtracted in an annular region, so the residual offset has essentially no impact on the integrated magnitudes. However, if the objects fall right across the jump, the photometry should be considered as suspect. Similarly, extended objects may spread over two or more quadrants, so their surface-brightness profile will suffer from the residual offset. More studies are in progress to better characterize this problem and find a solution or develop a correction to apply directly to the calibration pipeline. At the moment we suggest fitting the sky level in each quadrant separately. A stand-alone code based on the STSDAS `pedsky` task has been written for the first-order removal of the bias offset in observations of sparse fields (Sirianni et al. 2005). This script first reverses the multiplicative flat-field correction, then solves iteratively for the bias differences between the quadrants and removes them, before reapplying the flat field. This script has been used to produce sky flats and for the data reduction of the Ultra Deep Field. It will be made available in the future on the ACS STScI Web site.

Finally, WFC images may show apparent amplifier crosstalk between the four amplifiers, which produces very low level dark "ghosts" that are evident as mirror images of bright objects in the other quadrants. The amplitude of this effect is usually below any scientifically significant level, and shows a dependency on the background level and gain setting. A more detailed characterization of this problem is presented in Giavalisco (2004a, 2004b).

#### *3.1.2. HRC*

HRC images are read out using only one amplifier. As in the case of the WFC, the readout amplifier produces a horizontal ramp in the leading overscan, which extends up to 10 columns toward the active area. The bias level is therefore measured in the last six columns of the leading physical overscan. The task `doblev` removes the bias level row-by-row, as for the WFC quadrants. There is not a significant difference between the bias level in the overscan area and the active area.

### 3.2. Superbias Subtraction

Even after the bias-level subtraction from the overscan, some structure remains in the bias frames. This structure includes real bias pattern and also some dark current. In every image, including the zero-exposure time bias frames, dark counts accumulate for an additional time beyond the integration time, primarily in the time required to read out the detector. Since the WFC is operated in non-MPP readout, the dark-current rate during the readout is higher than during integration time. In order to remove this structure, a superbias is subtracted from each image. Bias frames are being taken as part of the ACS daily monitoring program for each supported gain state. Superbiases are created weekly by combining seven daily frames (Mutchler et al. 2004). There is some evidence for intermittent variations in the WFC bias structure at sub-ADU levels. On a few occasions, some frames have shown bias jumps in one or more quadrants, running for several hundred rows. These effects occur at a few tenths of an ADU level, and they might appear in one or more quadrants simultaneously. The probable source is interference with the electronics by other activities on the spacecraft. At the moment, there is no automatic detection of bias jumps within the calibration pipeline. Although bias jumps at the sub-ADU level are not important for most applications, they might exist in processed data, and we recommend a careful inspection of the data for their presence.

### 3.3. Dark Subtraction

CALACS removes the dark current from each scientific frame by subtracting a superdark frame. Every day, four 1000 s long dark frames are acquired for both the WFC and the HRC. Every 2 weeks, all the daily darks are combined in order to derive an accurate average dark rate for pixels that do not vary. These include normal pixels and "hot" pixels; i.e., pixels that generate a dark current higher than the average. Permanent hot pixels are due to native silicon lattice imperfections or impurities. During on-orbit operations, CCDs are exposed to radiation sources, such as protons and neutrons, that induce lattice damage and therefore generate hot pixels. As a consequence, the population of hot pixels changes on a daily basis. Therefore, the STScI calibration pipeline uses as a baseline a biweekly superdark that is updated with the hot pixel population of a specific day (Mutchler et al. 2004). For each science image, CALACS subtracts the appropriate superdark, which has been multiplied by the exposure time and divided by the gain. Any dark current accumulated during the readout time is automatically removed by the superbias subtraction.

Sirianni et al. (2004) analyzed the evolution of the hot pixel population in 2 yr of on-orbit operation from WFC and HRC dark frames. The number of hot pixels increases linearly with

time. Pixels with a dark current greater than 0.08 $e^-$ pixel$^{-1}$ s$^{-1}$ are flagged has "hot" in the data quality array in the FITS file. For this threshold, Sirianni et al. (2004) report a daily rate of about 47 and 800 new hot pixels for the HRC and WFC, respectively. Most radiation-induced hot pixels can be annealed by elevating the temperature of the CCD, thus allowing the reconstruction of the damaged lattice structure. An analysis of the effectiveness of the monthly annealing process in the first 2 yr of ACS operation shows that the annealing rate of new hot pixels with this threshold has been ~82% and ~86% for the WFC and HRC, respectively. Therefore, the population of permanent hot pixels is growing at a daily rate of about 6 and 140 new pixels for the HRC and WFC, respectively. Currently (2005 April), about 0.9% of the pixels of the WFC and the HRC CCDs are permanently classified as "hot." By comparison, cosmic rays typically impact 1.5%–3% of the pixels in a 1000 s exposure. Hot pixels could, for the most part, be eliminated by the superdark subtraction. However, since the dark current in hot pixels is dependent on the signal level (Janesick 2001), this process is not perfect. Moreover, there are indications that the noise in hot pixels is much higher than the normal shot noise (Riess 2002b). As a consequence, since the location of hot pixels is known from dark frames, they are flagged and discarded during image combinations. Careful planning of the observations, including a dithering strategy, will remove the impact of hot pixels on the science frame. See AIHv5 and ADHv4 for the best strategy for hot-pixel removal.

### 3.4. Flat Field

Appropriate flat-fielding normalizes the system illumination pattern, together with pixel-to-pixel nonuniformities, to generate accurate count rates that are independent of field position. Since in any WFC image each quadrant is read out independently, the ability to combine photometry from different chips/quadrants depends on the accuracy of the cross-quadrant and cross-chip normalization.

Intensive ground testing was devoted to the creation of laboratory flat fields to use for the reduction of on-orbit data by simulating sky illumination of the CCDs. The Refractive Aberrated Simulator/*Hubble* Optical Mechanical Simulator (RAS/HOMS) was used to produce high–S/N flat fields that include both the low-frequency (*L*-flat) and the high-frequency pixel-to-pixel (*P*-flat) structure (Martel & Hartig 2001; Bohlin et al. 2001). The low-order structure of the flats over the FOV is mostly due to the variations in the sensitivity of the CCD detectors. Thickness variations, nonuniform doping, or antireflection coating can result in a different response to incoming photons across the device area. Moreover, since the conversion of photons to electrons occurs at different depths within the CCD photosensitive silicon substrate, depending on the energy of the photons, the "cosmetics" of a flat field strongly depends on the wavelength (see AIHv5). Furthermore, since the filters are close to the focal plane, any variation in the filter transmission also contributes to the *L*-flat structure. The HRC CCD shows a typical sensitivity variation from center to edge of ~10%, while the large-format WFC minimum to maximum sensitivity variation is ~15%. To normalize to unity, the flats were normalized by the average number of counts in the central 1% (in area) of the image. In the case of the WFC frames, the WFC-2 image was divided by the WFC-1 central value, in order to preserve the overall sensitivity difference between the two CCDs across the gap that separates the two chips.

These "ground" flats contain information about the variation in CCD response and spatial structure in filter transmission, and were expected to differ from on-orbit flats principally by the ratio of the real *HST* ACS illumination pattern and the RAS/HOMS illumination pattern. A comparison of the observed count rates for the same star in different positions across the chip, after flat fielding, provides an estimate of the residual errors of the flat field and of the accuracy of the chip-to-chip normalization. Early Servicing Mission Orbital Verification (SMOV) data, of both individual spectrophotometric standards and stellar fields, suggested the presence of a residual low-frequency flat-field structure. There are a variety of plausible approaches to calibrate and remove this effect. However, the easiest methods to implement are either improper or not practical. The internal ACS calibration lamps illuminate the back of the calibration door, which is placed in the light path when a calibration lamp is turned on. Hence, the photons arrive at the detector through a different light path from science observations, bypassing the OTA. This results in a significantly different illumination pattern for internal flats relative to a uniform "sky." So while internal flat-field lamps exist, they are only used to monitor temporal variations. Bright Earth flats prove to be impractical, since they saturate in even the shortest exposures, except when the HRC or the two narrowband filters are employed. Even then, the resulting images are highly structured and streaky in appearance, due to terrestrial and atmospheric features passing through the field of view. The most obvious approach to correcting for a residual *L*-flat structure is to use deep images of "empty" sky fields. However, the creation of sky flats with appropriate S/Ns requires a very large number of images in each filter, in addition to careful masking to remove galaxies, stars, and other sources. Such an effort is currently in progress.

In the interim, a faster approach has been taken by the STScI ACS group. As described by Mack et al. (2002b), a moderately dense star field (NGC 104, in most cases) was observed at typically nine offset positions separated by hundreds of pixels, resulting in flux measurements of each star in nine largely separated positions. Since the entire field of view is well sampled by stars, the flux data are fitted to yield a low-order (fourth order) polynomial *L*-flat, as well as the flat-field–corrected flux of each star. The resulting polynomial is combined with the high spatial frequency structure of the ground flats to make

new "$P+L$" flats, as described by Mack et al. (2002a) and van der Marel (2003). While the original ground-based $P$ flat fields produced photometric errors of the order of $\pm 5\%$ from corner to corner. The new "$P+L$" flats yield a more uniform photometric response (within $\sim$1%) for a given star for any position in the field of view. As more data become available, improvements will be possible with the adoption of sky flats. Updates will be posted on the STScI Web page.

Finally, for the first 2 yr of operation, the ACS filter wheel movements were accurate to one motor step, which leads to an error that can exceed 1% in the flat fields over small regions. For seven filters on the WFC and six on the HRC with the worst blemishes, flat fields are available as a function of the filter wheel offset step (Bohlin et al. 2003). CALACS automatically selects the appropriate flat field corresponding to the offset step of each observation. On 2004 March the flight software was updated to make the filter wheel movements completely accurate.

### 3.5. Cosmic-Ray Rejection

As with any other *HST* instrument, the ACS is subject to cosmic rays and protons from the Earth's radiation belts. Cosmic rays usually generate significant quantities of electrons in more than one pixel. A first characterization of the cosmic rays in ACS images (Riess 2002a) shows that the fraction of pixels affected by cosmic rays varies between 1.5% and 3% during a 1000 s exposure for both the HRC and WFC. As a consequence, great care must be taken in planning and analyzing ACS observations to minimize the impact of cosmic rays on science images.

Cosmic-ray rejection in ACS frames can be performed in CALACS with the task `acsrej` or with MultiDrizzle. ADHv4 describes in great detail the two different techniques. Small offsets, even of the order of a few tenths of a pixel between pairs of images, can lead to apparent changes near a bright target that swamp expected Poisson differences. If large enough, these offsets can cause an incorrect flagging and rejection of the center of stars, mistaking the peak of a star for a cosmic ray. This problem is particularly severe for undersampled images. Optimization of the cosmic-ray removal process may require fine-tuning of the image alignment process (Mack et al. 2002a).

### 3.6. Geometric Distortion

By design, the ACS focal plane arrays are tilted with respect to incoming rays (20° for the WFC and 31° for the HRC). The result of this design is an image of the sky that is distorted in two different ways: (1) the pixels are elongated with a scale smaller along the radial direction of the OTA field of view than along the tangential direction, and (2) the pixel area varies across the detector.

The distortion affects astrometry and therefore the ability to register images taken at different pointings. Moreover, since the distortion causes pixels to have different effective areas as a function of their position, photometry and flat fielding are also affected. The geometrical area of each pixel is imprinted in the flat field, as well as the photometric sensitivity. PyDrizzle accounts for these effects, and the final geometric corrected output is photometrically and astrometrically corrected. *If, however, flat-fielded images are analyzed prior to the geometric correction with PyDrizzle, the effective area of each pixel must be accounted for when doing integrated photometry*. The correct total flux can be recovered by multiplying the flat-fielded images by the appropriate pixel area map. Once this correction has been applied and the image transformed in $e^{-}$ s$^{-1}$, the same zero point as that applied to drizzled data products can be used to transform to absolute flux units.

The calibration of the geometric distortion in the ACS detectors has been discussed in detail by Meurer et al. (2002, 2003) and Anderson (2002). Dithered observations of the rich NGC 104 star cluster have been used to calibrate the distortion. A fourth-order polynomial solution was found adequate for characterizing the distortion to an average rms accuracy of $\simeq$0.05 and $\simeq$0.03 pixels for the WFC and HRC, respectively, over the entire field of view of the two cameras. Although the main distortion characterization was performed using F475W data, the wavelength dependency of the solution has been checked with complementary observations in F775W (WFC and HRC) and F220W (HRC). A marginal increase in the rms in the redder filter was observed for the WFC, and little or no increase for the HRC. A more significant increase in the rms fit (up to 0.11 pixels) was observed in the UV HRC filter F220W, quite likely due to the elongation of 0.″1 of the UV PSF. Similar elongation has also been observed in SBC PSFs and can be attributed to the optics of either the ACS HRC/SBC mirrors or the *HST* OTA (Hartig et al. 2003).

Until 2004 September, the geometric distortion was removed by PyDrizzle in CALACS, using the correction table provided by Meurer et al. (2002), which provides an adequate solution for most of the applications that require an accuracy of the order of 0.1 pixels. A more sophisticated solution that includes a wavelength dependency based on the Anderson (2002) and Anderson & King (2004) results was implemented in CALACS at the end of 2004 September as part of MultiDrizzle (Koekemoer et al. 2002). The coefficients of the fit of the geometric distortion, and the scripts to transform these coefficients into a pixel area map, are available on the STScI/ACS Web page.

### 3.7. Charge Transfer Efficiency

Charge transfer is one of the basic steps of CCD operation. Electrons are transferred from the pixel where they are collected to the readout amplifier. During the transfer of charge from one pixel to the next, defects in the silicon can result in traps that remove small amounts of charge from the charge packet. The charge transfer efficiency (CTE) measures the effectiveness of

the charge transfer in a CCD, and it is typically measured as the fraction of charge transferred per pixel transfer.

CTE degradation is well known to affect data from previous *HST* cameras, such as WFPC2 and STIS. Several detailed studies characterizing CTE degradation and the formulation of empirical-correction formulae for WFPC2 and STIS have been published (Whitmore et al. 1999; Stetson 1998; Saha et al. 2000; Dolphin 2000b; Goudfrooij & Kimble 2002).

The total amount of charge lost increases with the number of pixel transfers. Therefore, even if ACS has a better CTE per pixel than WFPC2, the impact of CTE degradation is expected to be larger in ACS data, given the greater number of transfers (2048 for WFC and 1024 for HRC vs. 800 for WFPC2).

During on-orbit operations, CCDs are subject to radiation damage that degrades their ability to transfer charges. CTE degradation can lead to photometric inaccuracy (the magnitude of an object will depend on the position on the chip), astrometric shifts (the shape of the PSF is altered), and a decrease in discovery (the brightness of an object is reduced, and deferred charges can increase the noise in the background). A comprehensive discussion of the type of radiation damage is beyond the scope of this document. Excellent review papers on the subject can be found in the literature (e.g., Janesick et al. 1991; Hopkinson 1991). The principal factor that influences the charge transfer is the presence of spurious potential pockets and defects in the silicon lattice structure. These defects, more generically called traps, act as trapping sites for the transient electrons: part of the electrons contained in the signal packet can be trapped, and if they are released quickly, they rejoin the main packet of charge, but if they fall out of the traps at a slower rate than they go into the traps, they are left behind. The net CTE loss depends on the trap constants, their relevant variables, and the number density of traps (see Cawley et al. 2001 for a detailed description of the trap characteristics).

In order to reduce the impact of CTE degradation, the ACS CCDs, by design, incorporate a minichannel—a narrow extra-doped channel inside the buried channel. The higher potential, due to the extra doping, is designed to store and transfer small charge packets ($< 7\text{–}10 \times 10^3\ e^-$) entirely within the minichannel. The possibility of interaction between the charge packet and the traps in the buried channel is therefore minimized, resulting in a significant improvement of the CTE at these low signal levels.

A poor CTE has a strong impact on high-precision photometry. One of the major manifestations of a severely degraded CTE is the presence of tails of charge apparently streaming out of stellar point sources, in a direction away from the serial register. These tails are due to the release of trapped charges on timescales slightly longer than the readout clocking rate. Not all trapped charges are released within a few milliseconds; some traps release the charges in much longer timescales and contribute to the background noise of that same exposure or a subsequent one. This complex mechanism of capture and release, which depends on numerous factors (such as temperature, signal size, readout rate, and background level), can result in nonlinearity across the device, reduced image quality, reduced sensitivity, and a loss in spatial resolution. The effect of poor CTE on extended sources has been examined by Riess (2000) by subtracting pairs of images of galaxies observed near and far from the output amplifier. As one would expect, the charge is lost primarily from the leading edge of the galaxy image (the one closer to the readout amplifier). The trailing edge does not suffer significant loss, because the traps it sees are filled. It actually might see an increase in signal, due to deferred charges. The resulting asymmetry of extended objects may not have negligible consequences for statistical measurements of galaxy morphology, position angle, axial ratio, and asymmetry concentration (e.g., such as required for weak gravitational lensing studies of field galaxies). The net loss to a measured galaxy magnitude has small dependence on the size of the aperture used; it is usually in good agreement with the photometric loss expected for point-source photometry.

Several programs monitor the CTE performance of the CCDs in ACS. They are based either on calibration images taken with internal lamps (Sirianni et al. 2003, 2004; Mutchler & Sirianni 2005) or on the analysis of the cosmic-ray tails in dark images (Riess 2002b). These tests can track variations in CTE on a timescale of a few weeks. Monitoring CTE degradation is fairly easy, but the calculation of a correction formula based on stellar photometry and on the number of parallel and serial transfers in the CCDs is more difficult. There are several aspects to take into account: background level, signal strength of the source, photometric technique, etc. A large amount of data is necessary to constrain all dependencies. Riess (2003) and Riess & Mack (2004) have presented correction formulae to correct photometric losses as a function of a source's position, flux, background, time, and aperture size in ACS CCDs.

Riess (2003) found that the observed photometric losses in the WFC (HRC) range from $0.0\% \pm 0.2\%$ ($\sim$1%) for bright stars ($\sim 10^5\ e^-$) on a significant background ($\sim$tens of $e$) to as much as 7%–10% (5%–6%) for faint stars (a few hundred $e$) and a faint background ($<5\ e^-$). The observed dependence of the parallel transfer CTE loss (YCTE) versus stellar flux suggests a power-law relation that was utilized in the correction formula. Such a formula includes the dependence on the position, stellar flux, background level, and time of observation. At the moment, the correction formula does not include a dependence on the number of serial transfers. In general, the contribution of CTE degradation in the serial direction to the total charge loss is minimal, due to the faster readout clocking, as demonstrated by prelaunch testing. While internal calibration data already show a degradation even in the serial direction, it is still too weak to be detected with stellar photometry. Future observations will allow better constraints on the correction for CTE loss in both directions.

In the future, the effects of CTE degradation can be mitigated using the postflash capability included in the ACS. A relatively

low amount of charge is added to the general background, thus mitigating the effects of CTE degradation. However, the addition of this charge will of course elevate the background contribution of the noise. Also, the HRC can be operated in 4 amp readout, thus reducing the maximum number of parallel transfers from 1024 to 512.

## 4. THE ACS POINT-SPREAD FUNCTION

A detailed analysis of the image quality of the ACS cameras has been presented by Clampin et al. (2002) and Hartig et al. (2003). The latter also discusses the stray light characteristics, describing several ghost images and scattered light features. Naturally, observed PSFs vary with wavelength, field position, and time. Variations within the FOV arise from a combination of defocus, coma, astigmatism, and charge diffusion. Time variations occur from focus changes and spacecraft jitter during the exposures.

### 4.1. Spatial Variations

In general, PSF field-dependent variations in the ACS cameras are less severe than in other *HST* cameras. Krist (2003a) performed a very detailed study of the WFC and HRC field-dependent PSF variations due to optical and detector effects. Residual optical aberrations reduce the flux within the core of the PSF and redistribute it into the wings, degrading the encircled energy (EE). In the ACS WFC, PSF core width and ellipticity variations across the field are large enough to be a concern in the case of very small aperture photometry. Therefore, when performing PSF-fitting photometry, it is more appropriate to assume a spatially variable PSF when computing a PSF model or when fitting stars to the PSF model itself. In the smaller FOV of the HRC, the PSF can essentially be regarded as constant.

The major cause of alterations of the FWHM across the FOV is the blurring caused by the detector charge diffusion. All ACS CCDs are thinned backside-illuminated devices; therefore, the electrodes are on the rear face of the chip. Since the depth at which a photon is absorbed within the epitaxial layer is proportional to the wavelength, blue photons generate electrons at the top of the photosensitive layer. If the electric field is weak at the depth at which the electrons are generated, they may move and be collected into adjacent pixels. Charge diffusion is expected to be greater in the thicker regions of the CCD, and the largest variations in charge diffusion across the FOV are seen at the short wavelengths. Thickness variations in the ACS CCDs have been derived from fringe flat fields obtained during ground tests of the camera (Walsh et al. 2002, 2003). These results show that the CCD thickness varies between 12.6 and 17 $\mu$m in the WFC and 12.5 and 16.0 $\mu$m in the HRC.

Analytical modeling of the PSF in any FOV position for both ACS CCD cameras is possible with Tiny Tim.[14] Krist (2003a) developed a specific blurring kernel to reproduce the amount of charge diffusion observed, and these corrections have been implemented in the latest release of his software.

Dithering is a well-established technique for *HST* imaging, and has many advantages, such as improving the sampling of the PSF and mitigating the impact of hot pixels and detector blemishes (see ADHv4). The choice of a kernel for drizzling can change the shape of the core of the PSF. All our data were processed with the default linear kernel, but a different kernel is possible, depending on the data and scientific objectives. For example, if a square kernel is applied to a single image, with the parameters set to perform a bilinear interpolation, the output image will have strongly correlated noise, in addition to a degraded resolution. In all cases in which correlated noise is a major concern, a more different drizzle kernel should be considered. For example, the ACS Science Team pipeline (Blakeslee et al. 2003a) processes all Guaranteed Time Observer (GTO) data with the Lanczos3 kernel, which produces a sharper PSF core and a significant decrease in the apparent noise correlation in adjacent pixels.

### 4.2. Encircled Energy Curves

In order to measure the EE profile (i.e., the fraction of total source counts as a function of the aperture radius), we used the very high S/N observation of the spectrophotometric standard stars used for the zero-point determinations (see § 7). All stars are near the center of the chip. In the case of the WFC, the star was first centered in WFC-1 and then in WFC-2. In all cases, a couple of images have been taken for cosmic-ray rejection. The images have been processed with CALACS, and the geometric distortion has been removed with PyDrizzle.

The PSF of any instrument extends essentially to infinity. The far-field PSF can be measured only with very high S/N observations of isolated stars. Still, it is impossible to measure the flux beyond a certain radius without incurring systematic errors due to background determination, large-scale flat-field residual errors, nearby objects in the field, or detector edges. We have chosen to normalize the EE curves to the light at a 5.″5 circular radius aperture. An analysis of PSFs of saturated and unsaturated stars in all filters shows that this aperture is a safe assumption for measuring the total flux within an "infinite" aperture. It is also the maximum radius allowed for most of the images with stars centered in the HRC FOV, due to the presence of the Fastie finger.

One of the most difficult tasks for the proper measurement of encircled energy at large apertures is the determination of the sky background. In order to minimize the impact of errors on the sky background determination, we used the following technique in all cases for which multiple observations were

[14] Tiny Tim (J. Krist) is available online at http://www.stsci.edu/software/tinytim.

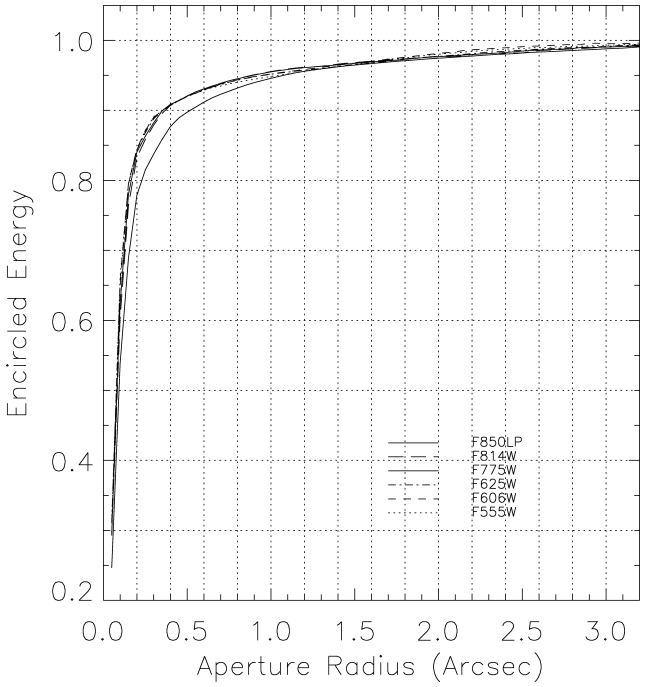


FIG. 3.—Comparison of EE profiles derived from multiple observations of two white dwarfs in visual and near-IR filters of the WFC.

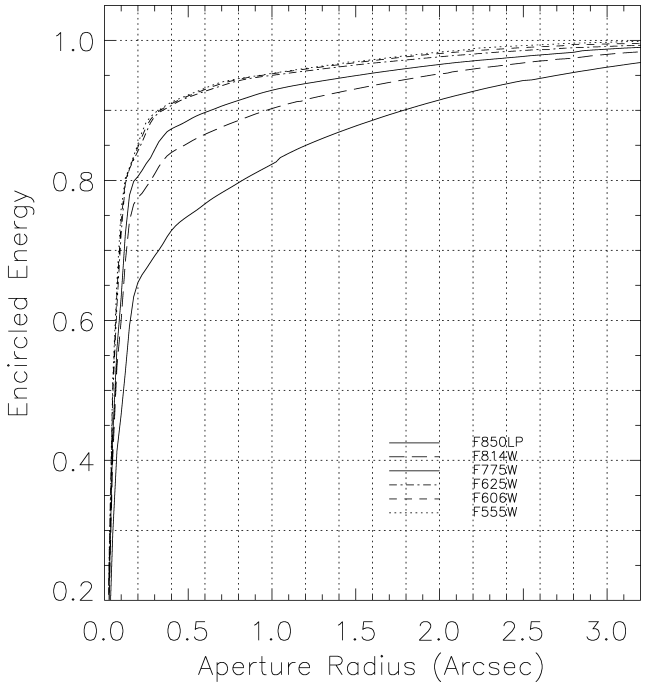


FIG. 4.—Comparison of EE profiles derived from multiple observations of two white dwarfs in visual and near-IR filters of the HRC.

available. First, using the information in the DQ array, we masked out the defective pixels in the SCI. This allowed us to exclude bad pixels or pixels masked by aperture features (such as the Fastie finger in the HRC) when performing statistics on the sky and the photometry. Then for each observation and for each filter, we determined the mode sky level in the sky annulus (from 6″ to 8″ for the WFC and from 5.″6 to 6.″5 for the HRC) and used this value to derive the total counts inside the 5.″5 radius aperture. Under the assumption that the flux of a standard is constant and that for a large aperture the major source of error should only be the Poisson noise, we calculated the median value of all determinations of total flux and calculated the appropriate sky level in each image that would be necessary to reproduce the median flux level. We then used the new sky level to perform the aperture photometry with DAOPHOT in a wide range of aperture radii.

The mean EE curves for different broadband filters are plotted as a function of aperture radius in Figure 3 for the WFC and Figure 4 for the HRC.

All curves are normalized to the mean value at 5.″5; however, in order to show in more detail the structure of the curves at smaller radii, only the values for the inner 3″ are plotted. The EE values for the broadband filters are tabulated, along with errors, in Tables 3 and 4. In order to better sample the impact of the long-wavelength halo in the near-IR (see § 4.3), we also include the narrowband filter F892N, whose effective wavelength falls between F814W and F850LP. The errors in these tables are the standard deviations from the different observations.

There are some variations between different observations. The main one is a commanded focus change obtained by means of a movement (3.6 $\mu$m) of the *HST* secondary mirror on 2002 December 2. This focus change has slightly modified the PSF in all wavelengths, but the most significant variation is seen in HRC-UV PSFs, which show a slightly sharper core. Normal thermally induced variations of the *HST* focus (breathing) may typically produce, within a single orbit, a displacement of the secondary mirror comparable to the one commanded in 2002 December. We therefore chose to average the EE profiles before and after the focus change, to create the mean EE curves. The larger errors at small-aperture radii in the EE curves of the HRC/UV filters reflect this variation in the PSF. On the other hand, the average PSFs at the center of WFC-1 and WFC-2 are remarkably similar, and we decided to combine the two data sets to improve the statistics.

Running PyDrizzle with different kernels produces PSF profiles that are significantly different only in the core of the PSF (0–10 pixels). The aperture corrections calculated with the EE can be applied to the photometric data, regardless of the choice of kernel, for aperture radii larger than 10 pixels.

### 4.3. Long-Wavelength Scattered Light

All ACS CCD detectors suffer from scattered light at long wavelengths. They are thinned backside-illuminated CCDs

TABLE 3
ENCIRCLED ENERGY: WFC

| APERTURE RADIUS | | | | | | | | | | |
|---|---|---|---|---|---|---|---|---|---|---|
| Pixels | Arcsec | F435W 4323.36[a] | F475W 4725.23 | F555W 5342.00 | F606W 5834.71 | F625W 6273.77 | F775W 7662.67 | F814W 7992.32 | F850LP 9013.50 | F892N 8914.36 |
| 1 ..... | 0.05 | 0.289 ± 0.011 | 0.318 ± 0.006 | 0.311 ± 0.005 | 0.313 ± 0.003 | 0.312 ± 0.004 | 0.296 ± 0.001 | 0.293 ± 0.009 | 0.246 ± 0.004 | 0.241 ± 0.002 |
| 2 ..... | 0.10 | 0.626 ± 0.011 | 0.669 ± 0.006 | 0.662 ± 0.003 | 0.656 ± 0.005 | 0.648 ± 0.004 | 0.623 ± 0.005 | 0.603 ± 0.006 | 0.538 ± 0.001 | 0.546 ± 0.007 |
| 3 ..... | 0.15 | 0.775 ± 0.004 | 0.801 ± 0.003 | 0.795 ± 0.002 | 0.796 ± 0.003 | 0.795 ± 0.002 | 0.780 ± 0.003 | 0.764 ± 0.004 | 0.689 ± 0.003 | 0.711 ± 0.007 |
| 4 ..... | 0.20 | 0.832 ± 0.002 | 0.850 ± 0.002 | 0.843 ± 0.001 | 0.845 ± 0.001 | 0.844 ± 0.000 | 0.840 ± 0.001 | 0.833 ± 0.002 | 0.779 ± 0.002 | 0.802 ± 0.004 |
| 5 ..... | 0.25 | 0.859 ± 0.000 | 0.876 ± 0.002 | 0.871 ± 0.001 | 0.871 ± 0.000 | 0.868 ± 0.001 | 0.863 ± 0.001 | 0.858 ± 0.001 | 0.815 ± 0.000 | 0.835 ± 0.001 |
| 6 ..... | 0.30 | 0.875 ± 0.000 | 0.890 ± 0.002 | 0.891 ± 0.000 | 0.890 ± 0.001 | 0.888 ± 0.000 | 0.882 ± 0.001 | 0.879 ± 0.000 | 0.837 ± 0.001 | 0.858 ± 0.000 |
| 7 ..... | 0.35 | 0.884 ± 0.001 | 0.900 ± 0.002 | 0.899 ± 0.001 | 0.900 ± 0.000 | 0.899 ± 0.000 | 0.899 ± 0.001 | 0.895 ± 0.001 | 0.858 ± 0.001 | 0.878 ± 0.000 |
| 8 ..... | 0.40 | 0.892 ± 0.001 | 0.907 ± 0.002 | 0.908 ± 0.000 | 0.908 ± 0.001 | 0.907 ± 0.000 | 0.909 ± 0.001 | 0.907 ± 0.001 | 0.877 ± 0.001 | 0.895 ± 0.000 |
| 9 ..... | 0.45 | 0.900 ± 0.000 | 0.914 ± 0.002 | 0.915 ± 0.000 | 0.914 ± 0.000 | 0.914 ± 0.000 | 0.914 ± 0.001 | 0.914 ± 0.001 | 0.889 ± 0.001 | 0.906 ± 0.000 |
| 10 ..... | 0.50 | 0.906 ± 0.000 | 0.920 ± 0.002 | 0.920 ± 0.000 | 0.920 ± 0.000 | 0.920 ± 0.000 | 0.921 ± 0.001 | 0.920 ± 0.001 | 0.897 ± 0.001 | 0.912 ± 0.000 |
| 11 ..... | 0.55 | 0.912 ± 0.000 | 0.925 ± 0.002 | 0.924 ± 0.001 | 0.925 ± 0.000 | 0.924 ± 0.000 | 0.926 ± 0.001 | 0.926 ± 0.001 | 0.905 ± 0.001 | 0.917 ± 0.000 |
| 12 ..... | 0.60 | 0.916 ± 0.001 | 0.930 ± 0.002 | 0.929 ± 0.001 | 0.929 ± 0.000 | 0.929 ± 0.000 | 0.931 ± 0.001 | 0.931 ± 0.001 | 0.912 ± 0.001 | 0.923 ± 0.000 |
| 13 ..... | 0.65 | 0.920 ± 0.001 | 0.934 ± 0.002 | 0.933 ± 0.001 | 0.933 ± 0.000 | 0.933 ± 0.000 | 0.935 ± 0.001 | 0.935 ± 0.001 | 0.918 ± 0.001 | 0.927 ± 0.000 |
| 14 ..... | 0.70 | 0.923 ± 0.001 | 0.937 ± 0.002 | 0.935 ± 0.001 | 0.938 ± 0.000 | 0.937 ± 0.000 | 0.939 ± 0.001 | 0.939 ± 0.001 | 0.923 ± 0.001 | 0.930 ± 0.000 |
| 15 ..... | 0.75 | 0.926 ± 0.001 | 0.940 ± 0.002 | 0.938 ± 0.001 | 0.941 ± 0.000 | 0.940 ± 0.000 | 0.942 ± 0.001 | 0.942 ± 0.001 | 0.927 ± 0.001 | 0.934 ± 0.000 |
| 16 ..... | 0.80 | 0.929 ± 0.001 | 0.943 ± 0.002 | 0.940 ± 0.001 | 0.944 ± 0.000 | 0.943 ± 0.000 | 0.945 ± 0.001 | 0.945 ± 0.001 | 0.932 ± 0.001 | 0.937 ± 0.000 |
| 17 ..... | 0.85 | 0.931 ± 0.001 | 0.945 ± 0.002 | 0.942 ± 0.001 | 0.946 ± 0.000 | 0.946 ± 0.000 | 0.948 ± 0.001 | 0.948 ± 0.001 | 0.936 ± 0.001 | 0.940 ± 0.000 |
| 18 ..... | 0.90 | 0.934 ± 0.001 | 0.948 ± 0.002 | 0.944 ± 0.001 | 0.948 ± 0.000 | 0.948 ± 0.000 | 0.950 ± 0.001 | 0.951 ± 0.001 | 0.940 ± 0.001 | 0.943 ± 0.000 |
| 19 ..... | 0.95 | 0.937 ± 0.001 | 0.950 ± 0.002 | 0.946 ± 0.001 | 0.950 ± 0.000 | 0.950 ± 0.000 | 0.953 ± 0.001 | 0.953 ± 0.001 | 0.943 ± 0.001 | 0.945 ± 0.000 |
| 20 ..... | 1.00 | 0.940 ± 0.001 | 0.952 ± 0.002 | 0.948 ± 0.001 | 0.952 ± 0.000 | 0.952 ± 0.000 | 0.955 ± 0.001 | 0.955 ± 0.001 | 0.946 ± 0.001 | 0.947 ± 0.000 |
| 25 ..... | 1.25 | 0.952 ± 0.001 | 0.968 ± 0.000 | 0.957 ± 0.001 | 0.960 ± 0.000 | 0.959 ± 0.000 | 0.962 ± 0.001 | 0.962 ± 0.000 | 0.958 ± 0.001 | 0.957 ± 0.000 |
| 30 ..... | 1.50 | 0.964 ± 0.001 | 0.974 ± 0.002 | 0.965 ± 0.001 | 0.967 ± 0.000 | 0.965 ± 0.000 | 0.967 ± 0.001 | 0.968 ± 0.001 | 0.965 ± 0.001 | 0.963 ± 0.001 |
| 35 ..... | 1.75 | 0.973 ± 0.001 | 0.983 ± 0.002 | 0.973 ± 0.001 | 0.974 ± 0.000 | 0.972 ± 0.000 | 0.972 ± 0.001 | 0.973 ± 0.001 | 0.970 ± 0.001 | 0.968 ± 0.001 |
| 40 ..... | 2.00 | 0.980 ± 0.001 | 0.989 ± 0.002 | 0.980 ± 0.001 | 0.981 ± 0.000 | 0.977 ± 0.000 | 0.977 ± 0.001 | 0.976 ± 0.000 | 0.974 ± 0.001 | 0.972 ± 0.001 |
| 45 ..... | 2.25 | 0.983 ± 0.001 | 0.994 ± 0.002 | 0.985 ± 0.001 | 0.987 ± 0.001 | 0.982 ± 0.000 | 0.980 ± 0.001 | 0.980 ± 0.001 | 0.978 ± 0.001 | 0.976 ± 0.001 |
| 50 ..... | 2.50 | 0.986 ± 0.001 | 0.997 ± 0.002 | 0.989 ± 0.001 | 0.991 ± 0.001 | 0.986 ± 0.000 | 0.985 ± 0.001 | 0.982 ± 0.000 | 0.982 ± 0.001 | 0.979 ± 0.001 |
| 55 ..... | 2.75 | 0.991 ± 0.001 | 0.998 ± 0.002 | 0.991 ± 0.001 | 0.994 ± 0.001 | 0.989 ± 0.000 | 0.988 ± 0.001 | 0.987 ± 0.001 | 0.985 ± 0.001 | 0.982 ± 0.001 |
| 60 ..... | 3.00 | 0.993 ± 0.001 | 1.000 ± 0.002 | 0.993 ± 0.001 | 0.995 ± 0.001 | 0.991 ± 0.000 | 0.990 ± 0.001 | 0.990 ± 0.001 | 0.988 ± 0.001 | 0.984 ± 0.001 |
| 65 ..... | 3.25 | 0.995 ± 0.001 | 1.001 ± 0.001 | 0.995 ± 0.001 | 0.996 ± 0.001 | 0.994 ± 0.000 | 0.993 ± 0.000 | 0.991 ± 0.001 | 0.991 ± 0.001 | 0.986 ± 0.001 |
| 70 ..... | 3.50 | 0.995 ± 0.001 | 1.001 ± 0.001 | 0.996 ± 0.001 | 0.997 ± 0.001 | 0.997 ± 0.001 | 0.995 ± 0.000 | 0.994 ± 0.000 | 0.994 ± 0.001 | 0.989 ± 0.001 |
| 75 ..... | 3.75 | 0.997 ± 0.000 | 1.003 ± 0.001 | 0.996 ± 0.001 | 0.999 ± 0.001 | 0.997 ± 0.001 | 0.995 ± 0.000 | 0.996 ± 0.001 | 0.996 ± 0.001 | 0.989 ± 0.000 |
| 80 ..... | 4.00 | 0.997 ± 0.001 | 1.002 ± 0.001 | 0.998 ± 0.001 | 0.998 ± 0.001 | 0.998 ± 0.001 | 0.998 ± 0.001 | 0.997 ± 0.001 | 0.997 ± 0.001 | 0.992 ± 0.000 |
| 85 ..... | 4.25 | 0.999 ± 0.000 | 1.002 ± 0.001 | 1.000 ± 0.000 | 0.999 ± 0.001 | 0.999 ± 0.001 | 0.999 ± 0.001 | 0.999 ± 0.001 | 0.997 ± 0.000 | 0.993 ± 0.000 |
| 90 ..... | 4.50 | 1.000 ± 0.000 | 1.002 ± 0.001 | 0.999 ± 0.001 | 1.000 ± 0.001 | 1.000 ± 0.001 | 1.000 ± 0.001 | 0.999 ± 0.001 | 1.000 ± 0.001 | 0.995 ± 0.000 |
| 95 ..... | 4.75 | 1.000 ± 0.001 | 1.001 ± 0.001 | 1.000 ± 0.001 | 1.000 ± 0.001 | 1.000 ± 0.001 | 1.000 ± 0.001 | 1.000 ± 0.001 | 1.001 ± 0.000 | 0.997 ± 0.001 |
| 100 ..... | 5.00 | 0.999 ± 0.000 | 1.001 ± 0.001 | 1.001 ± 0.000 | 1.001 ± 0.001 | 1.001 ± 0.001 | 1.001 ± 0.000 | 1.000 ± 0.001 | 1.001 ± 0.000 | 0.997 ± 0.000 |
| 110 ..... | 5.50 | 1.000 ± 0.000 | 1.000 ± 0.000 | 1.000 ± 0.000 | 1.000 ± 0.000 | 1.000 ± 0.000 | 1.000 ± 0.000 | 1.000 ± 0.000 | 1.000 ± 0.000 | 1.000 ± 0.000 |

[a] Average effective wavelength (Å) for the two spectrophotometric standard stars, both white dwarfs.

TABLE 4
ENCIRCLED ENERGY: HRC

| Aperture Radius | | | | | | | | | | | | | |
|---|---|---|---|---|---|---|---|---|---|---|---|---|---|
| Pixels | Arcsec | F220W 2244.64[a] | F250W 2702.15 | F330W 3356.23 | F435W 4317.55 | F475W 4756.77 | F555W 5338.72 | F606W 5806.35 | F625W 6258.62 | F775W 7634.95 | F814W 8037.84 | F850LP 9104.70 | F892N 8910.36 |
| 1 ..... | 0.025 | 0.235 ± 0.014 | 0.245 ± 0.013 | 0.250 ± 0.011 | 0.254 ± 0.005 | 0.230 ± 0.005 | 0.222 ± 0.002 | 0.221 ± 0.006 | 0.208 ± 0.003 | 0.171 ± 0.004 | 0.158 ± 0.002 | 0.109 ± 0.003 | 0.118 ± 0.001 |
| 2 ..... | 0.050 | 0.506 ± 0.010 | 0.534 ± 0.010 | 0.542 ± 0.008 | 0.532 ± 0.003 | 0.523 ± 0.006 | 0.514 ± 0.003 | 0.505 ± 0.004 | 0.490 ± 0.003 | 0.433 ± 0.001 | 0.403 ± 0.008 | 0.294 ± 0.006 | 0.324 ± 0.003 |
| 3 ..... | 0.075 | 0.623 ± 0.007 | 0.655 ± 0.006 | 0.679 ± 0.005 | 0.687 ± 0.005 | 0.678 ± 0.002 | 0.656 ± 0.003 | 0.640 ± 0.003 | 0.620 ± 0.003 | 0.560 ± 0.001 | 0.534 ± 0.001 | 0.413 ± 0.008 | 0.453 ± 0.002 |
| 4 ..... | 0.100 | 0.686 ± 0.007 | 0.720 ± 0.003 | 0.736 ± 0.004 | 0.762 ± 0.003 | 0.764 ± 0.001 | 0.759 ± 0.002 | 0.742 ± 0.004 | 0.723 ± 0.003 | 0.632 ± 0.002 | 0.599 ± 0.001 | 0.465 ± 0.007 | 0.498 ± 0.005 |
| 5 ..... | 0.125 | 0.733 ± 0.001 | 0.762 ± 0.002 | 0.775 ± 0.002 | 0.791 ± 0.001 | 0.796 ± 0.001 | 0.803 ± 0.001 | 0.799 ± 0.002 | 0.795 ± 0.002 | 0.723 ± 0.002 | 0.683 ± 0.001 | 0.526 ± 0.007 | 0.561 ± 0.005 |
| 6 ..... | 0.150 | 0.758 ± 0.002 | 0.788 ± 0.001 | 0.805 ± 0.000 | 0.813 ± 0.001 | 0.813 ± 0.002 | 0.818 ± 0.002 | 0.818 ± 0.002 | 0.816 ± 0.003 | 0.779 ± 0.002 | 0.742 ± 0.000 | 0.592 ± 0.008 | 0.631 ± 0.006 |
| 7 ..... | 0.175 | 0.771 ± 0.001 | 0.803 ± 0.001 | 0.825 ± 0.002 | 0.837 ± 0.001 | 0.833 ± 0.002 | 0.835 ± 0.001 | 0.832 ± 0.001 | 0.829 ± 0.002 | 0.798 ± 0.001 | 0.766 ± 0.001 | 0.634 ± 0.007 | 0.669 ± 0.006 |
| 8 ..... | 0.200 | 0.782 ± 0.002 | 0.814 ± 0.001 | 0.837 ± 0.003 | 0.858 ± 0.000 | 0.853 ± 0.003 | 0.852 ± 0.001 | 0.847 ± 0.001 | 0.842 ± 0.001 | 0.805 ± 0.002 | 0.775 ± 0.001 | 0.654 ± 0.005 | 0.683 ± 0.006 |
| 9 ..... | 0.225 | 0.791 ± 0.002 | 0.823 ± 0.001 | 0.846 ± 0.003 | 0.870 ± 0.001 | 0.868 ± 0.003 | 0.869 ± 0.001 | 0.863 ± 0.001 | 0.855 ± 0.001 | 0.814 ± 0.002 | 0.782 ± 0.002 | 0.665 ± 0.005 | 0.691 ± 0.006 |
| 10 ..... | 0.250 | 0.801 ± 0.002 | 0.830 ± 0.002 | 0.853 ± 0.003 | 0.875 ± 0.002 | 0.877 ± 0.003 | 0.883 ± 0.001 | 0.876 ± 0.001 | 0.869 ± 0.001 | 0.824 ± 0.001 | 0.790 ± 0.002 | 0.674 ± 0.005 | 0.697 ± 0.006 |
| 11 ..... | 0.275 | 0.811 ± 0.002 | 0.837 ± 0.002 | 0.858 ± 0.003 | 0.881 ± 0.002 | 0.883 ± 0.003 | 0.890 ± 0.000 | 0.887 ± 0.001 | 0.882 ± 0.001 | 0.832 ± 0.001 | 0.799 ± 0.002 | 0.683 ± 0.004 | 0.705 ± 0.006 |
| 12 ..... | 0.300 | 0.821 ± 0.002 | 0.844 ± 0.002 | 0.863 ± 0.003 | 0.887 ± 0.001 | 0.888 ± 0.003 | 0.896 ± 0.001 | 0.894 ± 0.001 | 0.891 ± 0.001 | 0.844 ± 0.001 | 0.809 ± 0.002 | 0.692 ± 0.004 | 0.713 ± 0.006 |
| 13 ..... | 0.325 | 0.829 ± 0.002 | 0.852 ± 0.002 | 0.868 ± 0.003 | 0.892 ± 0.001 | 0.893 ± 0.003 | 0.900 ± 0.001 | 0.899 ± 0.002 | 0.897 ± 0.001 | 0.855 ± 0.002 | 0.819 ± 0.002 | 0.700 ± 0.004 | 0.720 ± 0.006 |
| 14 ..... | 0.350 | 0.836 ± 0.002 | 0.859 ± 0.002 | 0.873 ± 0.003 | 0.895 ± 0.001 | 0.897 ± 0.003 | 0.904 ± 0.001 | 0.903 ± 0.002 | 0.900 ± 0.001 | 0.863 ± 0.001 | 0.828 ± 0.002 | 0.709 ± 0.004 | 0.728 ± 0.006 |
| 15 ..... | 0.375 | 0.842 ± 0.002 | 0.865 ± 0.002 | 0.878 ± 0.003 | 0.899 ± 0.001 | 0.900 ± 0.003 | 0.908 ± 0.001 | 0.906 ± 0.002 | 0.903 ± 0.001 | 0.870 ± 0.001 | 0.835 ± 0.002 | 0.720 ± 0.004 | 0.739 ± 0.006 |
| 16 ..... | 0.400 | 0.848 ± 0.002 | 0.869 ± 0.002 | 0.883 ± 0.003 | 0.902 ± 0.001 | 0.903 ± 0.003 | 0.912 ± 0.001 | 0.909 ± 0.002 | 0.907 ± 0.001 | 0.873 ± 0.001 | 0.840 ± 0.001 | 0.728 ± 0.004 | 0.748 ± 0.006 |
| 17 ..... | 0.425 | 0.854 ± 0.002 | 0.874 ± 0.002 | 0.888 ± 0.003 | 0.905 ± 0.001 | 0.906 ± 0.003 | 0.914 ± 0.001 | 0.912 ± 0.001 | 0.910 ± 0.001 | 0.877 ± 0.001 | 0.843 ± 0.001 | 0.735 ± 0.004 | 0.753 ± 0.006 |
| 18 ..... | 0.450 | 0.859 ± 0.002 | 0.878 ± 0.002 | 0.892 ± 0.003 | 0.908 ± 0.001 | 0.909 ± 0.003 | 0.917 ± 0.001 | 0.915 ± 0.001 | 0.914 ± 0.001 | 0.879 ± 0.001 | 0.847 ± 0.001 | 0.740 ± 0.004 | 0.756 ± 0.006 |
| 19 ..... | 0.475 | 0.865 ± 0.002 | 0.882 ± 0.002 | 0.895 ± 0.003 | 0.911 ± 0.001 | 0.912 ± 0.003 | 0.919 ± 0.001 | 0.918 ± 0.001 | 0.916 ± 0.001 | 0.882 ± 0.001 | 0.850 ± 0.001 | 0.745 ± 0.004 | 0.760 ± 0.006 |
| 20 ..... | 0.500 | 0.870 ± 0.002 | 0.886 ± 0.002 | 0.898 ± 0.003 | 0.915 ± 0.001 | 0.915 ± 0.003 | 0.922 ± 0.001 | 0.920 ± 0.001 | 0.919 ± 0.001 | 0.886 ± 0.001 | 0.853 ± 0.001 | 0.749 ± 0.004 | 0.764 ± 0.006 |
| 25 ..... | 0.625 | 0.895 ± 0.002 | 0.904 ± 0.002 | 0.910 ± 0.003 | 0.927 ± 0.001 | 0.928 ± 0.003 | 0.934 ± 0.001 | 0.932 ± 0.001 | 0.929 ± 0.001 | 0.899 ± 0.001 | 0.868 ± 0.001 | 0.771 ± 0.004 | 0.784 ± 0.006 |
| 30 ..... | 0.750 | 0.919 ± 0.002 | 0.921 ± 0.002 | 0.921 ± 0.003 | 0.934 ± 0.001 | 0.935 ± 0.003 | 0.943 ± 0.001 | 0.941 ± 0.002 | 0.939 ± 0.001 | 0.910 ± 0.001 | 0.881 ± 0.001 | 0.789 ± 0.004 | 0.801 ± 0.006 |
| 35 ..... | 0.875 | 0.939 ± 0.002 | 0.936 ± 0.001 | 0.932 ± 0.003 | 0.941 ± 0.001 | 0.941 ± 0.003 | 0.948 ± 0.001 | 0.948 ± 0.002 | 0.946 ± 0.001 | 0.920 ± 0.001 | 0.892 ± 0.001 | 0.807 ± 0.003 | 0.818 ± 0.006 |
| 40 ..... | 1.000 | 0.952 ± 0.002 | 0.951 ± 0.001 | 0.942 ± 0.003 | 0.948 ± 0.001 | 0.947 ± 0.003 | 0.953 ± 0.001 | 0.952 ± 0.002 | 0.950 ± 0.001 | 0.929 ± 0.001 | 0.903 ± 0.001 | 0.823 ± 0.003 | 0.831 ± 0.006 |
| 45 ..... | 1.125 | 0.961 ± 0.002 | 0.962 ± 0.001 | 0.952 ± 0.003 | 0.954 ± 0.001 | 0.953 ± 0.003 | 0.957 ± 0.001 | 0.957 ± 0.002 | 0.954 ± 0.001 | 0.935 ± 0.001 | 0.911 ± 0.001 | 0.842 ± 0.001 | 0.846 ± 0.006 |
| 50 ..... | 1.250 | 0.967 ± 0.002 | 0.969 ± 0.001 | 0.961 ± 0.003 | 0.960 ± 0.001 | 0.958 ± 0.003 | 0.962 ± 0.001 | 0.961 ± 0.002 | 0.958 ± 0.001 | 0.940 ± 0.001 | 0.918 ± 0.001 | 0.855 ± 0.001 | 0.858 ± 0.006 |
| 55 ..... | 1.375 | 0.971 ± 0.002 | 0.975 ± 0.002 | 0.968 ± 0.003 | 0.964 ± 0.001 | 0.963 ± 0.003 | 0.966 ± 0.001 | 0.964 ± 0.001 | 0.961 ± 0.001 | 0.945 ± 0.001 | 0.925 ± 0.001 | 0.867 ± 0.001 | 0.869 ± 0.005 |
| 60 ..... | 1.500 | 0.975 ± 0.002 | 0.979 ± 0.002 | 0.973 ± 0.002 | 0.970 ± 0.001 | 0.968 ± 0.003 | 0.969 ± 0.001 | 0.968 ± 0.001 | 0.965 ± 0.001 | 0.950 ± 0.001 | 0.931 ± 0.001 | 0.878 ± 0.001 | 0.879 ± 0.005 |
| 65 ..... | 1.625 | 0.977 ± 0.002 | 0.982 ± 0.002 | 0.977 ± 0.003 | 0.975 ± 0.001 | 0.972 ± 0.003 | 0.973 ± 0.001 | 0.972 ± 0.001 | 0.968 ± 0.001 | 0.954 ± 0.001 | 0.936 ± 0.001 | 0.888 ± 0.001 | 0.888 ± 0.005 |
| 70 ..... | 1.750 | 0.980 ± 0.002 | 0.984 ± 0.002 | 0.980 ± 0.002 | 0.979 ± 0.001 | 0.976 ± 0.003 | 0.977 ± 0.001 | 0.975 ± 0.001 | 0.971 ± 0.001 | 0.958 ± 0.001 | 0.942 ± 0.001 | 0.897 ± 0.000 | 0.897 ± 0.005 |
| 75 ..... | 1.875 | 0.981 ± 0.002 | 0.986 ± 0.002 | 0.984 ± 0.002 | 0.982 ± 0.001 | 0.979 ± 0.003 | 0.980 ± 0.001 | 0.978 ± 0.001 | 0.974 ± 0.001 | 0.962 ± 0.001 | 0.947 ± 0.001 | 0.906 ± 0.000 | 0.905 ± 0.005 |
| 80 ..... | 2.000 | 0.983 ± 0.002 | 0.988 ± 0.002 | 0.984 ± 0.002 | 0.984 ± 0.002 | 0.982 ± 0.003 | 0.983 ± 0.001 | 0.981 ± 0.001 | 0.976 ± 0.001 | 0.966 ± 0.001 | 0.952 ± 0.001 | 0.915 ± 0.000 | 0.913 ± 0.005 |
| 85 ..... | 2.125 | 0.985 ± 0.002 | 0.989 ± 0.002 | 0.987 ± 0.002 | 0.986 ± 0.001 | 0.985 ± 0.003 | 0.986 ± 0.001 | 0.984 ± 0.001 | 0.979 ± 0.001 | 0.969 ± 0.001 | 0.957 ± 0.001 | 0.923 ± 0.001 | 0.919 ± 0.004 |
| 90 ..... | 2.250 | 0.987 ± 0.002 | 0.990 ± 0.002 | 0.988 ± 0.002 | 0.988 ± 0.001 | 0.987 ± 0.003 | 0.989 ± 0.000 | 0.986 ± 0.001 | 0.981 ± 0.001 | 0.972 ± 0.001 | 0.961 ± 0.001 | 0.930 ± 0.001 | 0.926 ± 0.004 |
| 95 ..... | 2.375 | 0.988 ± 0.002 | 0.991 ± 0.002 | 0.989 ± 0.002 | 0.989 ± 0.001 | 0.988 ± 0.003 | 0.991 ± 0.000 | 0.988 ± 0.001 | 0.984 ± 0.001 | 0.974 ± 0.001 | 0.964 ± 0.000 | 0.937 ± 0.001 | 0.932 ± 0.004 |
| 100 ..... | 2.500 | 0.989 ± 0.002 | 0.992 ± 0.002 | 0.990 ± 0.002 | 0.990 ± 0.001 | 0.990 ± 0.003 | 0.992 ± 0.000 | 0.990 ± 0.001 | 0.985 ± 0.001 | 0.977 ± 0.001 | 0.968 ± 0.001 | 0.943 ± 0.001 | 0.938 ± 0.004 |
| 110 ..... | 2.750 | 0.991 ± 0.002 | 0.993 ± 0.002 | 0.992 ± 0.002 | 0.992 ± 0.001 | 0.992 ± 0.002 | 0.995 ± 0.000 | 0.993 ± 0.001 | 0.989 ± 0.001 | 0.982 ± 0.001 | 0.974 ± 0.000 | 0.952 ± 0.001 | 0.948 ± 0.004 |
| 120 ..... | 3.000 | 0.993 ± 0.001 | 0.995 ± 0.002 | 0.994 ± 0.001 | 0.993 ± 0.001 | 0.994 ± 0.002 | 0.997 ± 0.000 | 0.995 ± 0.001 | 0.991 ± 0.001 | 0.987 ± 0.000 | 0.980 ± 0.001 | 0.962 ± 0.001 | 0.957 ± 0.004 |
| 130 ..... | 3.250 | 0.995 ± 0.001 | 0.996 ± 0.002 | 0.995 ± 0.001 | 0.993 ± 0.000 | 0.995 ± 0.002 | 0.999 ± 0.000 | 0.996 ± 0.001 | 0.993 ± 0.001 | 0.991 ± 0.000 | 0.984 ± 0.000 | 0.970 ± 0.001 | 0.964 ± 0.004 |
| 140 ..... | 3.500 | 0.996 ± 0.001 | 0.996 ± 0.001 | 0.996 ± 0.001 | 0.995 ± 0.000 | 0.997 ± 0.002 | 1.000 ± 0.000 | 0.997 ± 0.001 | 0.995 ± 0.001 | 0.993 ± 0.000 | 0.988 ± 0.001 | 0.977 ± 0.001 | 0.970 ± 0.004 |
| 150 ..... | 3.750 | 0.997 ± 0.001 | 0.997 ± 0.001 | 0.996 ± 0.001 | 0.997 ± 0.001 | 0.998 ± 0.002 | 0.999 ± 0.001 | 0.998 ± 0.001 | 0.996 ± 0.001 | 0.994 ± 0.001 | 0.991 ± 0.000 | 0.982 ± 0.001 | 0.976 ± 0.003 |
| 160 ..... | 4.000 | 0.998 ± 0.001 | 0.997 ± 0.001 | 0.997 ± 0.001 | 0.998 ± 0.000 | 0.998 ± 0.001 | 0.999 ± 0.001 | 0.998 ± 0.001 | 0.997 ± 0.001 | 0.996 ± 0.001 | 0.993 ± 0.000 | 0.987 ± 0.001 | 0.981 ± 0.002 |
| 170 ..... | 4.250 | 0.998 ± 0.001 | 0.999 ± 0.001 | 0.998 ± 0.001 | 0.998 ± 0.000 | 0.998 ± 0.001 | 1.000 ± 0.000 | 0.999 ± 0.000 | 0.997 ± 0.001 | 0.996 ± 0.000 | 0.995 ± 0.000 | 0.990 ± 0.001 | 0.985 ± 0.002 |
| 180 ..... | 4.500 | 0.999 ± 0.001 | 0.999 ± 0.001 | 0.998 ± 0.000 | 0.998 ± 0.000 | 0.998 ± 0.001 | 0.999 ± 0.001 | 0.999 ± 0.000 | 0.998 ± 0.001 | 0.997 ± 0.000 | 0.996 ± 0.000 | 0.994 ± 0.001 | 0.988 ± 0.002 |
| 190 ..... | 4.750 | 0.998 ± 0.000 | 0.999 ± 0.000 | 0.998 ± 0.001 | 0.999 ± 0.001 | 0.999 ± 0.001 | 1.000 ± 0.000 | 0.999 ± 0.000 | 0.998 ± 0.001 | 0.998 ± 0.000 | 0.997 ± 0.000 | 0.996 ± 0.001 | 0.992 ± 0.002 |
| 200 ..... | 5.000 | 0.999 ± 0.001 | 0.999 ± 0.001 | 0.999 ± 0.001 | 1.000 ± 0.000 | 0.999 ± 0.000 | 1.000 ± 0.000 | 1.000 ± 0.000 | 0.999 ± 0.001 | 0.999 ± 0.000 | 0.999 ± 0.000 | 0.998 ± 0.001 | 0.996 ± 0.001 |
| 210 ..... | 5.250 | 1.000 ± 0.000 | 1.000 ± 0.000 | 1.000 ± 0.000 | 1.000 ± 0.000 | 1.000 ± 0.000 | 1.000 ± 0.000 | 1.000 ± 0.000 | 0.999 ± 0.000 | 1.000 ± 0.000 | 1.000 ± 0.000 | 0.999 ± 0.000 | 0.998 ± 0.000 |
| 220 ..... | 5.500 | 1.000 ± 0.000 | 1.000 ± 0.000 | 1.000 ± 0.000 | 1.000 ± 0.000 | 1.000 ± 0.000 | 1.000 ± 0.000 | 1.000 ± 0.000 | 1.000 ± 0.000 | 1.000 ± 0.000 | 1.000 ± 0.000 | 1.000 ± 0.000 | 1.000 ± 0.000 |

[a] Average effective wavelength (Å) for the two spectrophotometric standard stars, both white dwarfs.

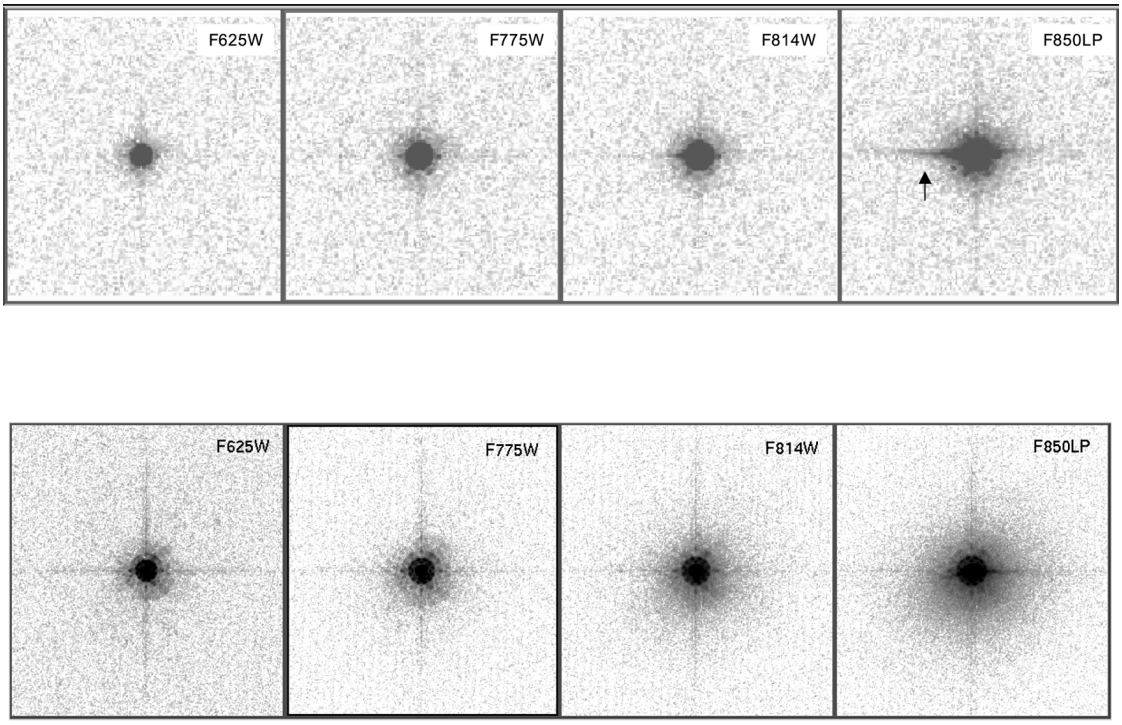


FIG. 5.—WFC (*top*) and HRC (*bottom*) images (7″.5 × 7″.5) taken through the near-IR broadband filters, showing the long-wavelength scattered halo. The halo grows considerably in the HRC from left to right. The antihalation aluminum layer of the WFC effectively reduces the halo in the WFC, but it gives rise to a spike in the row direction toward the edge containing amplifiers AC, as indicated by the arrow.

and consequently are relatively transparent to the near-IR–wavelength photons. A 16 $\mu$m–thinned CCD transmits ~5% of 8000 Å photons and ~85% of 1 $\mu$m photons. In the case of SITe CCDs, the transmitted long-wavelength light illuminates and scatters in the CCD header, a soda glass substrate. It is then reflected back from the header's metalized rear surface and re-illuminates the CCD's front-side photosensitive surface (Sirianni et al. 1998). The fraction of integrated light in the scattered light halo increases as a function of wavelength. The onset of the halos occurs at a wavelength of ~7500 Å. The HRC CCD scatters the near-IR light into a broad halo centered on the target; the intensity of the halo increases with the wavelength and reaches about 20% of the total energy at 1 $\mu$m (Fig. 5).

In order to rectify the long-wavelength halo, the WFC CCDs incorporate a special antihalation aluminum layer between the front side of the CCD and its glass substrate (Sirianni et al. 1998). While this layer is effective at suppressing the IR halo, it appears to give rise to a relatively strong spike in the row direction toward the edge containing amplifiers A and C, as illustrated in Figure 5. This feature, probably due to scatter from the CCD channel stop structure, contains ~20% of the PSF energy at 1 $\mu$m but is almost insignificant at 8000 Å (Hartig et al. 2003).

The EE profiles change naturally with the wavelength in any diffraction-limited optical system. However, at the onset of the long-wavelength halo, the PSF becomes broader than expected. Figures 3 and 4 show the variation of the EE profile for the standard stars as a function of the filter in the visible and near-IR for the WFC and HRC, respectively. In the case of the WFC, the long-wavelength halo is effectively suppressed by the antihalation aluminum layer; the EE profiles of all filters from F555W to F814W overlap nicely, and only the F850LP EE shows sign of broadening, with ~2.3% less flux in a 0″.5 radius aperture than in the same aperture in F814W. The effect of the scattered light is more severe for the HRC (Fig. 4), in which the broadening of the PSF is clearly visible at F775W and increases at longer wavelengths. With respect to the flux contained in a 0″.5 radius aperture in the F625W filter, the HRC F775W, F814W, and F850LP PSFs respectively contain about 3.3%, 8.5%, and 16.9% less flux.

The same mechanism responsible for the variation of the intensity and extension of the halo as a function of the wavelength is also responsible for the variation of the shape of the PSF as a function of the color of the source. The spectral energy distribution (SED) of two stars with different colors is different within any given bandpass. If we take as an example the F850LP filter and we observe a hot star and a cold star that produce the same total counts in this filter, more long-wavelength photons are collected from the red star than from the

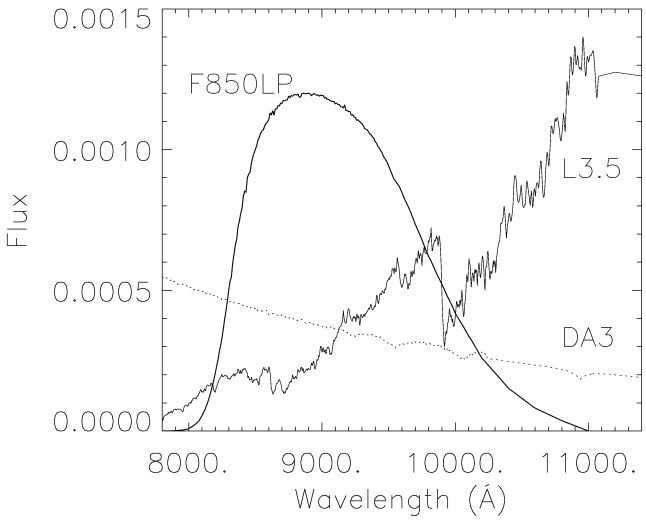


FIG. 6.—SED of the hot GRW+70 (DA3) star (*dotted line*) and the cold 2M0036+18 (L3.5) dwarf star (*solid line*), normalized to produce the same arbitrary magnitude within the HRC F850LP filter (also shown). The wavelength-dependent contribution to counts within the same passband changes dramatically for these stars. The effective wavelength is 9107 Å for GRD +70 and 9445 Å for 2M0036+18.

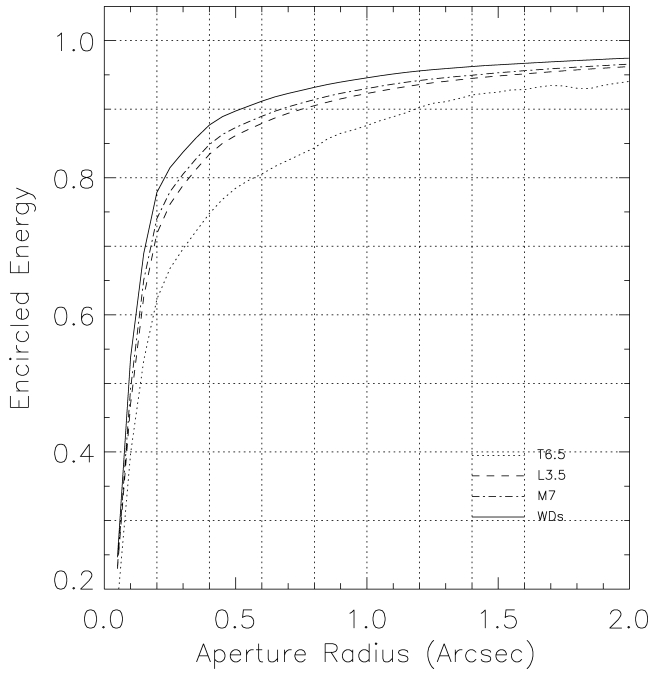


FIG. 7.—Variation of the EE in the WFC F850LP filter for different types of stars.

blue star (see Fig. 6). As a result, the number of photons transmitted by the F850LP filter that are scattered in the CCD substrate is larger for the red star than for the blue star. The PSF for the red star will therefore be broader than that of the blue star. The effective wavelength is a source-dependent passband parameter that represents the mean wavelength of the detected photons and can be used to estimate *shifts* of the average wavelength due to source characteristics (e.g., temperature, reddening, and redshift); it is defined as[15]

$$\lambda_{\rm eff} \equiv \frac{\int f_\lambda(\lambda) P(\lambda) \lambda^2 \, d\lambda}{\int f_\lambda(\lambda) P(\lambda) \lambda \, d\lambda},$$

where $P(\lambda)$ is the dimensionless passband transmission curve and $f_\lambda(\lambda)$ is the flux distribution of the object, usually in ergs $\mathrm{cm}^{-2}\ \mathrm{s}^{-1}\ \text{Å}^{-1}$. The term $\lambda_{\rm eff}$ can be used to estimate the impact of the light scattering on the aperture correction for any observation.

In order to characterize the ACS throughput in the near-IR and the PSF in the filters affected by the long-wavelength halo, a set of intrinsically red stars have been observed with both the HRC and WFC (Gilliland & Riess 2002). We used these three stars with spectral types M, L, and T to calculate the near-IR EE curves. For the M and T stars, flux-calibrated spectra are available from the literature, whereas for the L dwarf a STIS spectrum has been acquired. Spectrophotometric data are used to get information on the wavelength distribution of the flux in the near-IR filters (i.e., to calculate the effective wavelength). Gilliland & Riess (2002) compared the observed flux of the three standard stars within an aperture of 2.″8 with the prediction of the ACS exposure time calculator and provided a provisional quantum efficiency correction in the near-IR. We derived the EE profile from these stars using the same data, but as in the case of the EE of the standard stars, the curves have been normalized to the counts in a 5.″5 radius aperture. Figures 7 and 8 show how the EE profile changes with spectral type in F850LP for the WFC and HRC, respectively. We did not include the curve for the T6.5 star in Figure 8, because it was impossible to obtain an accurate profile up to 5.″5. It should be noted that although Figure 3 shows a broadening only for the WFC F850LP EE, this does not mean that only this filter can be affected by scattered light at long wavelengths. Those curves have been determined from the observations of two spectrophotometric standard stars, both hot white dwarfs. Although its effect is greatly reduced by the antihalation correction, light scattering also occurs when a very red object is imaged through the F775W and F814W WFC filters. From Figures 7 and 8 it is evident that for all filters affected by the long-wavelength light scattering, the aperture correction will be different for objects with different colors (see § 4.5).

The first assessment of the scientific impact of this PSF artifact in the near-IR was made by Sirianni et al. (1998) and Gilliland & Riess (2002). The presence of an extended halo centered on the core of the target has the obvious effect of

[15] This definition includes the factor $\lambda/hc$ to convert the energy flux to photon flux as appropriate for photon-counting detectors.

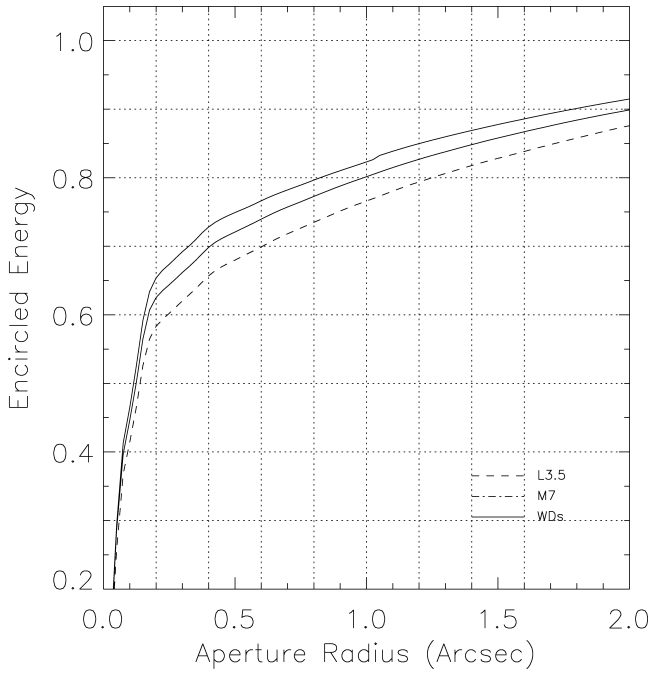


FIG. 8.—Variation of the EE in the HRC F850LP filter for different types of stars.

reducing the S/N and the limiting magnitude of the camera in the near-IR. The halo can also have an impact on the photometry of very crowded fields. The effects of the long-wavelength halo should also be taken into account when performing morphological studies. The apparent size of a resolved object in any near-IR filter can increase with the intrinsic color of the source.

In general, the effects of the PSF red halo should also be considered in doing surface photometry of extended objects, as significant biases may occur. For example, Tonry et al. (1997, 2001) found that the $(V - I)$ colors of their ground-based survey galaxies measured with thinned SITe CCDs (such as used in the ACS) were too red by several hundredths of a magnitude or more. The bias was attributed to this fraction of the *I*-band light of the standard stars being lost to the red halo. Since the galaxy photometry was measured over larger areas, they appeared too red with respect to the standards. Reobservation of the galaxies with thick CCDs was undertaken to ensure accurate photometry.

In the case of the ACS, we have calibrated the standard-star photometry to an infinite radius, so the integrated colors of extended objects within very large apertures should be correct. However, a bias may still occur for measurements of small-aperture colors or gradients, especially for the HRC. Michard (2002) has done experiments convolving model early-type galaxies with empirical PSFs that included the CCD red halo. He found that the bias was large enough to reverse the sense of some $(V - I)$ gradients; the effect on colors involving the $z$ band would be even greater. Michard recommended convolving each image with the PSF from the other bandpass before attempting to measure galaxy color maps. Blakeslee et al. (2003b) took the opposite approach in measuring ACS/WFC $(i - z)$ colors of faint early-type galaxies within the galaxy effective radii. They deconvolved the images in each bandpass, using empirical WFC PSFs and an implementation of the CLEAN algorithm (Högbom 1974), which preserves total flux; the mean color correction for their sample was +0.05 mag, and twice this for the most compact galaxies. Thus, there are various approaches to the problem, but proper care is required to achieve accurate galaxy colors.

### 4.4. Aperture Correction

In order to reduce errors due to the residual flat-fielding error and background variations, and to increase the S/N, the two most popular photometric techniques, aperture photometry and PSF-fitting photometry, are usually performed by measuring the flux within a small radius around the center of the source. This measurement must be tied to the total count rates by applying an aperture correction. This correction could be the major source of systematic errors in the calibration of PSF fluxes.

For all the photometric calibration measurements, we decided to use an aperture of 5″.5 radius. This allowed us to estimate the total flux of spectrophotometric standard stars and apply corrections to the response curve of the instrument (see § 6). Our zero points are based on such measurements, and therefore they refer to this fiducial aperture. However, such a large aperture can be used only for bright and isolated sources and is impractical for most science observations.

A definition of zero points linked to a smaller aperture is often more convenient. For example, WFPC2 zero points are historically defined in relation to the flux in an aperture of radius 0″.5 (Holtzman et al. 1995a). Using a noninfinite zero point implies an additional correction to the zero point for surface photometry. This corresponds to the aperture correction from 0″.5 to nominal infinity, which amounts to 0.1 mag for WFPC2, irrespective of filters (Holtzman et al. 1995a). But even a 0″.5 aperture is impractical for point-source photometry in a number of situations (photometry of crowded stellar fields, faint objects or targets with an uneven background), and smaller apertures need to be used, with the consequent need for aperture corrections. In all these circumstances, it is also impossible to measure the aperture correction from any smaller aperture radius to "infinity."

A WFPC2-like approach for the zero-point definition is less practical for ACS because, in both HRC and WFC, the aperture correction from 0″.5 to "infinity" fluctuates from filter to filter, with variations up to 15%. In § 7 we therefore provide zero points for the fiducial aperture (5″.5), which can be used directly for surface photometry. This choice is also dictated by the fact that the photometric calibration defined by STScI and returned

by SYNPHOT traditionally refers to an "infinite" aperture, allowing a better conversion between point sources and extended sources.

As part of the ACS calibration we have determined the count rate conversion from an intermediate aperture to "infinity." In Table 5 we provide the aperture correction from 0.″5 to "infinity" (AC05) derived from the EE profiles listed in Tables 3 and 4. The offset between photometry within a smaller aperture and photometry with a 0.″5 radius aperture can be easily determined and added to the value listed in Table 5. This is usually done by measuring a few bright stars in an uncrowded region of the FOV and applying the offset to all photometric measurements. If we define the observed magnitude as

$$\mathrm{OBMAG} = -2.5 \times \log(\text{total count rate } [e^- \ \mathrm{s}^{-1}]), \quad (1)$$

then for point-source photometry, equation (1) becomes

$$\mathrm{OBMAG} = -2.5 \times \log(\text{count rate at } r \leq 0.''5 \ [e^- \ \mathrm{s}^{-1}]) - \mathrm{AC05}, \quad (2)$$

where AC05 is listed in Table 5. The AC05 values are derived from the photometry of the two spectrophotometric standards stars used in this paper. They are both hydrogen white dwarfs and therefore are not suitable for deriving the aperture correction for stars with much redder colors (see § 4.5).

One problem that must be addressed is that the variation of the PSF as a function of position on the image may require the application of different aperture corrections for different regions of the FOV. Of course, how the photometry is carried out determines how seriously the results are affected by the space and temporal variations of the PSF. If the aperture used is large enough (about 0.″5 in radius), then the aperture correction will be both small and fairly constant. When performing photometry in a small aperture, however, the assumption of a single aperture correction applied to all photometry in the entire chip may lead to large systematic errors. To minimize this effect, an empirical mapping of the aperture correction should be applied. An appropriate data set will eventually be available, but meanwhile it may be possible to compute a suite of PSF models using Tiny Tim. Unfortunately, the current version of Tiny Tim does not model the residual long-wavelength halo in the WFC, and the HRC PSF models include only a rough estimate of the long-wavelength scattered light.

Our determination of the EE profiles, and therefore of the aperture correction, is based on aperture photometry and on the measurement of the sky level within an annulus far from the object (from 6″ to 8″ for WFC and from 5.″6 to 6.″5 for HRC) in order to estimate the "true" sky level. If a smaller annulus is chosen, closer to the center of the object, the sky level will include more light from the wings of the stars, and therefore the sky-subtracted counts will be lower. From the EE tabulated in this paper or from PSFs created with Tiny Tim and assuming a stable PSF, it is possible to calculate the correction to apply to a measurement with any choice of sky annulus to correct it for the true sky level.

TABLE 5
APERTURE CORRECTION FROM 0.″5 APERTURE RADIUS TO INFINITE (AC05)

| | HRC | | WFC | |
|---|---|---|---|---|
| FILTER | Mag | Error | Mag | Error |
| F220W ..... | 0.151 | 0.002 | ... | ... |
| F250W ..... | 0.132 | 0.002 | ... | ... |
| F330W ..... | 0.117 | 0.003 | ... | ... |
| F334N ..... | 0.113 | 0.004 | ... | ... |
| F435W ..... | 0.097 | 0.001 | 0.107 | 0.004 |
| F475W ..... | 0.096 | 0.004 | 0.095 | 0.002 |
| F502N ..... | 0.093 | 0.001 | 0.094 | 0.001 |
| F550M ..... | 0.092 | 0.001 | 0.083 | 0.001 |
| F555W ..... | 0.088 | 0.001 | 0.092 | 0.001 |
| F606W ..... | 0.090 | 0.002 | 0.088 | 0.000 |
| F625W ..... | 0.092 | 0.001 | 0.088 | 0.001 |
| F658N ..... | 0.098 | 0.001 | 0.085 | 0.003 |
| F660N ..... | 0.110 | 0.001 | 0.090 | 0.003 |
| F775W ..... | 0.132 | 0.001 | 0.087 | 0.001 |
| F814W ..... | 0.172 | 0.002 | 0.087 | 0.001 |
| F850LP ..... | 0.314 | 0.006 | 0.117 | 0.000 |
| F892N ..... | 0.293 | 0.009 | 0.100 | 0.002 |

NOTE.—OBMAG = −2.5 log (count rate $r \leq 0.''5$ [$e^-$ $\mathrm{s}^{-1}$]) − AC05.

Finally, we must stress that accurate aperture corrections are a function of time and location on the chip. A blind application of the data presented in this paper should be avoided, especially at small radii; and when using small apertures for the photometry, the aperture correction should be derived for each frame on which measurements are made. Avoiding this necessary step can introduce systematic errors in the photometry up to several percent. The tables provided here should be used to estimate approximate aperture corrections when it is otherwise impossible to determine such corrections directly from the image.

### 4.5. Aperture Correction in the Near-IR

In order to assess when the broadening of the PSF due to the long-wavelength halo should be taken into account and to estimate the aperture correction for red stars, we combined the information from the EE profiles of all the stars used for the characterization of the long-wavelength light scattering. We first calculated the effective wavelength in all filters for each star.

The effective wavelength can change significantly within the same filter; for instance, in the WFC F850LP there is a difference of ~760 Å between the effective wavelength of the hot white dwarfs and the cold T dwarf. Then we calculated the aperture correction from a few selected aperture radii to the nominal infinite aperture using the EE profile of each star. We finally correlated the aperture correction and the effective wavelength for each filter/aperture combination, as shown in Figures 9 and 10 for WFC and HRC, respectively, for a few

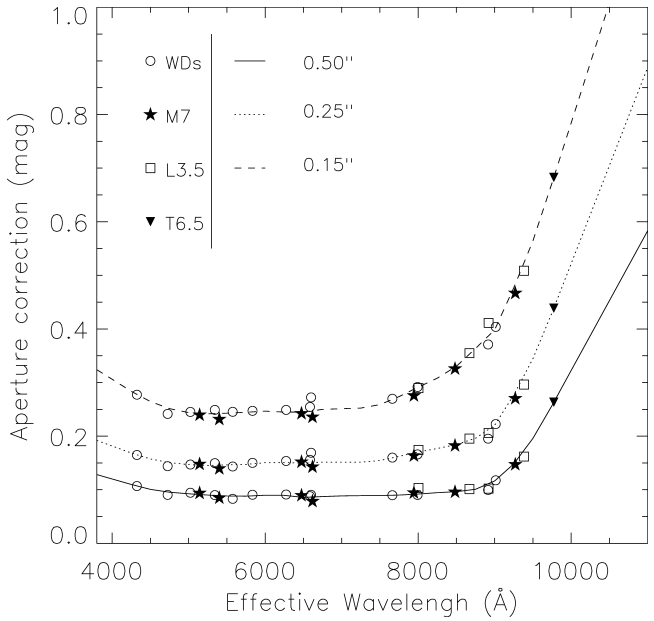


FIG. 9.—Aperture corrections vs. effective wavelength for the WFC. Three different aperture radii are shown here. The aperture correction is from the selected aperture to the nominal infinite aperture. Different stars are represented with different symbols.

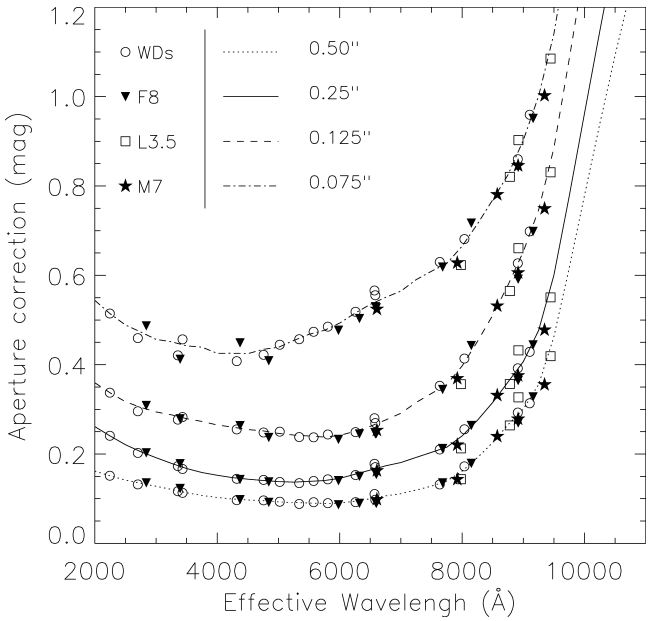


FIG. 10.—Same as Fig. 9, but for the HRC.

selected apertures (3, 5, and 10 pixel radii, equivalent to 0.″125, 0.″25, and 0.″5 for WFC; and 3, 5, 10, and 20 pixel radius, equivalent to 0.″075, 0.″125, 0.″25, and 0.″50 for the HRC). The values for each star are represented with a different symbol. Not all the stars have a complete set of observations in all filters. For each star we display only the points relative to broadband and narrowband filters for which it was possible to determine an EE profile up to 5.″5. For any choice of aperture radii, there is a fairly smooth variation of the aperture correction as a function of wavelength. For both the WFC and the HRC, the aperture correction is fairly uniform in the visible but increases in the blue and in the near-IR. The increase of aperture correction in the blue is due to charge diffusion (see § 4.2), while the increase in the red is due to the long-wavelength halo (see § 4.3). Naturally, the smaller the aperture, the stronger the variation in aperture correction with the effective wavelength. In Tables 6 and 7 we list the aperture correction to the fiducial aperture for a regular grid of effective wavelengths and several aperture radii obtained after interpolation of the plotted data.

In order to use these tables, the effective wavelength for a specific observation needs to be calculated. If an empirical spectrum or a model of the SED of the object is available, the effective wavelength can be easily calculated for any filter, for example with the task CALCPHOT in SYNPHOT. Table 8 lists the effective wavelengths of a sample of stars of different spectral types in the near-IR filters for WFC and HRC.

If the SED of the object is totally unknown but observations with the same ACS camera in at least two filters exist, it is still possible to get an estimate of the effective wavelength. First the count rates of the target should be measured in both filters using the same aperture radii and in such a way that the instrumental color for the selected apertures can be calculated:

$$\mathrm{color}_r = -2.5 \log \left[ \frac{(\mathrm{count\ rate})_{\mathrm{flt1},\,r}}{(\mathrm{count\ rate})_{\mathrm{flt2},\,r}} \right],$$

where flt1 and flt2 are the two filters and $r$ is the radius of the aperture where both fluxes have been measured. Then a color$_r$ versus effective wavelength relation can be created with SYNPHOT for any combination of filters and aperture radii using an atlas of synthetic spectra covering a large range of spectral types. Several spectral atlases are available in STSDAS, but any atlas can be used. Both effective wavelength and color$_r$ can be computed with the routine CALCPHOT in SYNPHOT. In fact, a new keyword "`aper`" has been implemented to call for the encircled energy tables in the OBSMODE for ACS. This keyword allows one to estimate the flux of a star within a selected aperture and not just the total flux in an infinite aperture, which is the default for SYNPHOT.

As an example we show in Figure 11 the color$_r$ versus effective wavelength relation for three near-IR filters for the WFC using the color$_r$ F814W–F850LP and an aperture of $r = 0.''5$. In order to produce this plot, we ran CALCPHOT using the

TABLE 6
WFC Effective Wavelength Aperture Correction Relation

| Effective Wavelength[a] (Å) | Aperture Radius | | | | | | | | | | | |
|---|---|---|---|---|---|---|---|---|---|---|---|---|
| | 0.″10 | 0.″15 | 0.″20 | 0.″25 | 0.″30 | 0.″40 | 0.″50 | 0.″60 | 0.″80 | 1.″00 | 1.″50 | 2.″00 |
| 3500 ..... | 0.651 | 0.351 | 0.246 | 0.208 | 0.184 | 0.162 | 0.140 | 0.129 | 0.113 | 0.096 | 0.061 | 0.044 |
| 3750 ..... | 0.610 | 0.328 | 0.233 | 0.195 | 0.173 | 0.152 | 0.130 | 0.119 | 0.104 | 0.088 | 0.056 | 0.038 |
| 4000 ..... | 0.566 | 0.306 | 0.218 | 0.182 | 0.161 | 0.140 | 0.120 | 0.108 | 0.093 | 0.080 | 0.049 | 0.031 |
| 4250 ..... | 0.521 | 0.284 | 0.204 | 0.169 | 0.149 | 0.128 | 0.110 | 0.099 | 0.083 | 0.071 | 0.042 | 0.024 |
| 4500 ..... | 0.481 | 0.265 | 0.192 | 0.157 | 0.139 | 0.117 | 0.101 | 0.089 | 0.074 | 0.063 | 0.036 | 0.019 |
| 4750 ..... | 0.454 | 0.251 | 0.183 | 0.151 | 0.131 | 0.111 | 0.095 | 0.083 | 0.069 | 0.057 | 0.034 | 0.016 |
| 5000 ..... | 0.443 | 0.244 | 0.182 | 0.147 | 0.129 | 0.107 | 0.093 | 0.081 | 0.067 | 0.056 | 0.035 | 0.018 |
| 5250 ..... | 0.446 | 0.242 | 0.182 | 0.145 | 0.127 | 0.105 | 0.091 | 0.079 | 0.065 | 0.055 | 0.035 | 0.019 |
| 5500 ..... | 0.451 | 0.243 | 0.183 | 0.146 | 0.125 | 0.104 | 0.088 | 0.078 | 0.063 | 0.053 | 0.034 | 0.019 |
| 5750 ..... | 0.458 | 0.244 | 0.183 | 0.147 | 0.125 | 0.102 | 0.088 | 0.076 | 0.061 | 0.051 | 0.034 | 0.019 |
| 6000 ..... | 0.461 | 0.247 | 0.183 | 0.151 | 0.127 | 0.105 | 0.089 | 0.079 | 0.063 | 0.052 | 0.035 | 0.021 |
| 6250 ..... | 0.461 | 0.245 | 0.183 | 0.151 | 0.128 | 0.105 | 0.089 | 0.079 | 0.063 | 0.053 | 0.038 | 0.024 |
| 6500 ..... | 0.468 | 0.245 | 0.180 | 0.150 | 0.125 | 0.101 | 0.086 | 0.075 | 0.059 | 0.050 | 0.035 | 0.024 |
| 6750 ..... | 0.474 | 0.250 | 0.182 | 0.152 | 0.128 | 0.102 | 0.087 | 0.076 | 0.060 | 0.051 | 0.036 | 0.025 |
| 7000 ..... | 0.490 | 0.251 | 0.184 | 0.151 | 0.130 | 0.104 | 0.088 | 0.078 | 0.061 | 0.051 | 0.038 | 0.026 |
| 7250 ..... | 0.507 | 0.252 | 0.188 | 0.151 | 0.134 | 0.104 | 0.089 | 0.078 | 0.061 | 0.051 | 0.038 | 0.026 |
| 7500 ..... | 0.523 | 0.259 | 0.193 | 0.155 | 0.136 | 0.105 | 0.089 | 0.078 | 0.060 | 0.051 | 0.036 | 0.026 |
| 7750 ..... | 0.533 | 0.274 | 0.197 | 0.162 | 0.139 | 0.106 | 0.091 | 0.078 | 0.061 | 0.050 | 0.036 | 0.026 |
| 8000 ..... | 0.538 | 0.291 | 0.200 | 0.170 | 0.143 | 0.108 | 0.092 | 0.079 | 0.061 | 0.051 | 0.036 | 0.027 |
| 8250 ..... | 0.549 | 0.308 | 0.205 | 0.177 | 0.147 | 0.111 | 0.094 | 0.081 | 0.064 | 0.052 | 0.038 | 0.027 |
| 8500 ..... | 0.584 | 0.330 | 0.217 | 0.184 | 0.155 | 0.114 | 0.096 | 0.083 | 0.065 | 0.053 | 0.038 | 0.029 |
| 8750 ..... | 0.639 | 0.364 | 0.238 | 0.196 | 0.168 | 0.122 | 0.101 | 0.087 | 0.068 | 0.056 | 0.039 | 0.029 |
| 9000 ..... | 0.687 | 0.398 | 0.270 | 0.220 | 0.191 | 0.141 | 0.117 | 0.100 | 0.079 | 0.064 | 0.043 | 0.032 |
| 9250 ..... | 0.768 | 0.477 | 0.328 | 0.277 | 0.237 | 0.180 | 0.149 | 0.128 | 0.099 | 0.080 | 0.052 | 0.038 |
| 9500 ..... | 0.874 | 0.564 | 0.409 | 0.345 | 0.302 | 0.237 | 0.196 | 0.171 | 0.134 | 0.106 | 0.066 | 0.050 |
| 9750 ..... | 0.989 | 0.673 | 0.505 | 0.431 | 0.384 | 0.308 | 0.257 | 0.229 | 0.180 | 0.140 | 0.083 | 0.065 |
| 10000 ..... | 1.106 | 0.784 | 0.605 | 0.522 | 0.473 | 0.384 | 0.323 | 0.291 | 0.229 | 0.176 | 0.101 | 0.081 |
| 10250 ..... | 1.224 | 0.896 | 0.704 | 0.613 | 0.558 | 0.461 | 0.387 | 0.351 | 0.278 | 0.213 | 0.118 | 0.096 |
| 10500 ..... | 1.340 | 1.008 | 0.804 | 0.705 | 0.645 | 0.537 | 0.453 | 0.412 | 0.327 | 0.249 | 0.136 | 0.113 |
| 10750 ..... | 1.454 | 1.120 | 0.904 | 0.796 | 0.733 | 0.612 | 0.517 | 0.473 | 0.376 | 0.285 | 0.154 | 0.129 |
| 11000 ..... | 1.572 | 1.231 | 1.003 | 0.888 | 0.820 | 0.689 | 0.584 | 0.535 | 0.425 | 0.321 | 0.171 | 0.145 |

[a] Values for $\lambda < 4300$ Å and $\lambda > 9800$ Å are extrapolated.

Bruzual, Perrson, Gunn, and Stryker (BPGS) stellar atlas[16] available in STSDAS to calculate the effective wavelength and the synthetic color$_r$ with $r = 0.''5$. We also plot in Figure 11 the position of the five stars used for the EE study. This approach can be applied to any camera, color, and aperture. From plots of this type it is possible to estimate the effective wavelength of an object and get the aperture correction from any choice of aperture radius to the nominal "infinite" aperture from Tables 6 and 7.

In order to better quantify the impact that the near-IR scattered light has on ACS photometry, we present two cases in Appendix C, the first one for a high-redshift galaxy and the second for point-source photometry of an extremely red star.

## 5. GAIN, LINEARITY, AND SATURATION

Both WFC and HRC can be operated at multiple gain settings, nominally at 1, 2, 4, and 8 $e^-$ ADU$^{-1}$. However, only two settings are fully supported for each camera: gain 1 and 2 for WFC, and 2 and 4 for HRC. On-orbit calibration is not available for unsupported gain settings, and therefore they will not be covered in this paper (see AIHv5 for more information on all available gain settings). The default gain values of $\sim$1 $e^-$ ADU$^{-1}$ for WFC and $\sim$2 $e^-$ ADU$^{-1}$ for HRC have been used to establish the adjustment to the quantum efficiency curves.

The absolute gain values for the WFC and HRC were derived during the ground calibration campaign at GSFC in the spring and summer 2001. Details on the procedure and analysis are available in Martel et al. (2001a) and (2001b) for the WFC and HRC, respectively. The measured gain had a typical accuracy of 0.6%. Bohlin et al. (2002) improved the determination of the relative gain between the pair of amplifiers on the same CCD chip and the gain ratio between the two WFC chips. The authors used preflight flat fields and maintained the same mean value over all amplifiers at a given gain setting by imposing a continuity constraint across quadrant boundaries on each chip and at the adjacent edges of the gap between the two

[16] The BPGS Stellar Atlas can be accessed at http://www.stsci.edu/HST/observatory/cdbs/astronomical_catalogs.html.

TABLE 7
HRC Effective Wavelength Aperture Correction Relation

| Effective Wavelength[a] (Å) | Aperture Radius | | | | | | | | | | | | |
|---|---|---|---|---|---|---|---|---|---|---|---|---|---|
| | 0.″075 | 0.″10 | 0.″15 | 0.″20 | 0.″25 | 0.″30 | 0.″40 | 0.″50 | 0.″60 | 0.″80 | 1.″00 | 1.″50 | 2.″00 |
| 2000 ..... | 0.544 | 0.438 | 0.359 | 0.289 | 0.261 | 0.231 | 0.193 | 0.161 | 0.134 | 0.081 | 0.052 | 0.031 | 0.021 |
| 2250 ..... | 0.514 | 0.409 | 0.337 | 0.266 | 0.240 | 0.214 | 0.179 | 0.151 | 0.127 | 0.081 | 0.053 | 0.027 | 0.019 |
| 2500 ..... | 0.489 | 0.384 | 0.317 | 0.244 | 0.221 | 0.198 | 0.165 | 0.141 | 0.120 | 0.082 | 0.055 | 0.026 | 0.016 |
| 2750 ..... | 0.473 | 0.370 | 0.304 | 0.226 | 0.205 | 0.187 | 0.155 | 0.135 | 0.117 | 0.085 | 0.059 | 0.027 | 0.018 |
| 3000 ..... | 0.457 | 0.358 | 0.294 | 0.212 | 0.192 | 0.176 | 0.146 | 0.128 | 0.113 | 0.086 | 0.063 | 0.029 | 0.019 |
| 3250 ..... | 0.451 | 0.348 | 0.288 | 0.198 | 0.179 | 0.165 | 0.139 | 0.120 | 0.108 | 0.085 | 0.064 | 0.030 | 0.018 |
| 3500 ..... | 0.442 | 0.333 | 0.279 | 0.187 | 0.167 | 0.155 | 0.131 | 0.113 | 0.102 | 0.081 | 0.064 | 0.030 | 0.016 |
| 3750 ..... | 0.439 | 0.323 | 0.273 | 0.179 | 0.159 | 0.145 | 0.125 | 0.107 | 0.096 | 0.078 | 0.061 | 0.030 | 0.016 |
| 4000 ..... | 0.425 | 0.311 | 0.265 | 0.173 | 0.152 | 0.139 | 0.119 | 0.102 | 0.091 | 0.075 | 0.060 | 0.031 | 0.016 |
| 4250 ..... | 0.426 | 0.305 | 0.260 | 0.171 | 0.147 | 0.134 | 0.116 | 0.099 | 0.087 | 0.073 | 0.060 | 0.033 | 0.018 |
| 4500 ..... | 0.425 | 0.299 | 0.255 | 0.170 | 0.144 | 0.130 | 0.112 | 0.098 | 0.085 | 0.071 | 0.059 | 0.034 | 0.019 |
| 4750 ..... | 0.434 | 0.298 | 0.252 | 0.174 | 0.141 | 0.128 | 0.110 | 0.095 | 0.083 | 0.069 | 0.059 | 0.036 | 0.020 |
| 5000 ..... | 0.439 | 0.295 | 0.246 | 0.175 | 0.138 | 0.125 | 0.106 | 0.093 | 0.081 | 0.066 | 0.057 | 0.035 | 0.020 |
| 5250 ..... | 0.454 | 0.299 | 0.242 | 0.178 | 0.137 | 0.122 | 0.104 | 0.092 | 0.080 | 0.064 | 0.056 | 0.035 | 0.020 |
| 5500 ..... | 0.468 | 0.308 | 0.240 | 0.178 | 0.139 | 0.120 | 0.102 | 0.091 | 0.080 | 0.063 | 0.055 | 0.035 | 0.021 |
| 5750 ..... | 0.477 | 0.315 | 0.238 | 0.178 | 0.141 | 0.120 | 0.102 | 0.089 | 0.079 | 0.061 | 0.053 | 0.035 | 0.021 |
| 6000 ..... | 0.493 | 0.330 | 0.242 | 0.180 | 0.145 | 0.122 | 0.104 | 0.089 | 0.079 | 0.063 | 0.053 | 0.035 | 0.022 |
| 6250 ..... | 0.515 | 0.352 | 0.251 | 0.187 | 0.155 | 0.128 | 0.110 | 0.094 | 0.085 | 0.067 | 0.058 | 0.041 | 0.027 |
| 6500 ..... | 0.535 | 0.373 | 0.262 | 0.194 | 0.164 | 0.135 | 0.116 | 0.100 | 0.089 | 0.072 | 0.061 | 0.045 | 0.032 |
| 6750 ..... | 0.551 | 0.397 | 0.276 | 0.202 | 0.174 | 0.144 | 0.122 | 0.106 | 0.095 | 0.078 | 0.066 | 0.049 | 0.034 |
| 7000 ..... | 0.565 | 0.417 | 0.291 | 0.208 | 0.181 | 0.152 | 0.127 | 0.111 | 0.100 | 0.081 | 0.068 | 0.049 | 0.034 |
| 7250 ..... | 0.590 | 0.449 | 0.315 | 0.218 | 0.192 | 0.165 | 0.135 | 0.119 | 0.107 | 0.087 | 0.073 | 0.051 | 0.035 |
| 7500 ..... | 0.609 | 0.478 | 0.336 | 0.229 | 0.204 | 0.178 | 0.144 | 0.128 | 0.114 | 0.094 | 0.079 | 0.055 | 0.038 |
| 7750 ..... | 0.627 | 0.502 | 0.356 | 0.238 | 0.215 | 0.191 | 0.155 | 0.140 | 0.125 | 0.102 | 0.086 | 0.060 | 0.042 |
| 8000 ..... | 0.665 | 0.542 | 0.397 | 0.263 | 0.240 | 0.217 | 0.178 | 0.161 | 0.145 | 0.120 | 0.101 | 0.071 | 0.050 |
| 8250 ..... | 0.715 | 0.591 | 0.452 | 0.298 | 0.275 | 0.252 | 0.210 | 0.192 | 0.174 | 0.146 | 0.124 | 0.087 | 0.061 |
| 8500 ..... | 0.769 | 0.645 | 0.510 | 0.339 | 0.315 | 0.291 | 0.245 | 0.226 | 0.206 | 0.175 | 0.150 | 0.105 | 0.072 |
| 8750 ..... | 0.825 | 0.712 | 0.578 | 0.384 | 0.361 | 0.336 | 0.288 | 0.266 | 0.244 | 0.209 | 0.179 | 0.125 | 0.087 |
| 9000 ..... | 0.902 | 0.786 | 0.653 | 0.433 | 0.407 | 0.380 | 0.327 | 0.301 | 0.277 | 0.237 | 0.204 | 0.140 | 0.096 |
| 9250 ..... | 1.001 | 0.874 | 0.746 | 0.509 | 0.477 | 0.446 | 0.389 | 0.355 | 0.328 | 0.282 | 0.242 | 0.168 | 0.117 |
| 9500 ..... | 1.141 | 1.011 | 0.885 | 0.637 | 0.600 | 0.566 | 0.502 | 0.463 | 0.430 | 0.372 | 0.323 | 0.231 | 0.164 |
| 9750 ..... | 1.343 | 1.207 | 1.084 | 0.820 | 0.777 | 0.737 | 0.663 | 0.616 | 0.578 | 0.503 | 0.441 | 0.323 | 0.231 |
| 10000 ..... | 1.554 | 1.414 | 1.291 | 1.014 | 0.963 | 0.916 | 0.834 | 0.779 | 0.735 | 0.643 | 0.567 | 0.420 | 0.304 |
| 10250 ..... | 1.768 | 1.624 | 1.499 | 1.204 | 1.147 | 1.094 | 1.003 | 0.939 | 0.889 | 0.781 | 0.691 | 0.517 | 0.373 |
| 10500 ..... | 1.992 | 1.838 | 1.711 | 1.390 | 1.325 | 1.265 | 1.165 | 1.094 | 1.036 | 0.911 | 0.811 | 0.607 | 0.440 |
| 10750 ..... | 2.233 | 2.060 | 1.929 | 1.568 | 1.493 | 1.426 | 1.318 | 1.234 | 1.175 | 1.034 | 0.919 | 0.685 | 0.498 |
| 11000 ..... | 2.498 | 2.284 | 2.156 | 1.737 | 1.647 | 1.572 | 1.454 | 1.359 | 1.296 | 1.140 | 1.011 | 0.746 | 0.544 |

[a] Values for $\lambda > 9500$ Å are extrapolated.

chips. This provided an improvement in amplifier-to-amplifier gains to better than 0.1%.

Since all the photometric calibration data are taken with the default gains, it is important to accurately know the ratio between different gain settings in order to transform the current calibration to nondefault gain observations. Gilliland (2004) performed an accurate adjustment of the major gain values relative to the default gain levels through analysis of repeated observations in the same filter of the same stellar field, at different gain settings. Gilliland's findings improved the relative calibration of gains to better than 0.1%, removing errors that average about 1% for both HRC and WFC. The corrections to the gain value for WFC gain 2 and 4 and HRC gain 1 and 4 were implemented in CALACS on 2004 January 6. The new values (see Table 9) are being used for the calibration of any data retrieved from the *HST* archive after that date. Table 9 shows the corrective coefficient to add to the zero points for data processed before 2004 January 6.

Absolute errors of ~0.6% are still possible in the default gain values. However, these absolute errors have no impact in the photometric calibration of ACS because the adjustments to the detector quantum efficiency, and therefore the zero points, were based on data acquired with the default gain settings. The use of the appropriate relative gain ratios between quadrants and between the default and the supported settings will ensure that the photometric calibration accuracy is maintained in all modes. Since the output of CALACS is an image already converted to electrons (FLT files) or $e^{-1}$ $s^{-1}$ (DRZ files), there is no need to differentiate the photometric calibration for different gains. For the current paper we assume that the image has

TABLE 8
EFFECTIVE WAVELENGTH (Å) FOR STARS OF DIFFERENT SPECTRAL TYPES IN THE NEAR-IR

| | WFC | | | HRC | | |
|---|---|---|---|---|---|---|
| STAR TYPE | F775W | F814W | F850LP | F775W | F814W | F850LP |
| O5 V ..... | 7659.4 | 7986.0 | 9012.0 | 7631.7 | 8030.7 | 9103.2 |
| B0 V ..... | 7663.0 | 7995.1 | 9017.6 | 7635.3 | 8041.7 | 9108.5 |
| B5 V ..... | 7672.4 | 8015.4 | 9028.7 | 7644.6 | 8064.7 | 9119.3 |
| A0 V ..... | 7678.4 | 8044.3 | 9056.2 | 7650.5 | 8099.1 | 9146.2 |
| A5 V ..... | 7688.1 | 8061.4 | 9062.7 | 7660.2 | 8118.2 | 9152.2 |
| F2 V ..... | 7703.7 | 8085.1 | 9064.7 | 7675.8 | 8144.3 | 9154.3 |
| F6 V ..... | 7707.8 | 8088.0 | 9069.8 | 7679.8 | 8147.5 | 9159.7 |
| G0 V ..... | 7713.6 | 8097.7 | 9074.9 | 7685.7 | 8158.3 | 9164.9 |
| G5 V ..... | 7714.9 | 8105.0 | 9082.6 | 7687.0 | 8167.2 | 9172.4 |
| K0 V ..... | 7717.3 | 8106.5 | 9077.1 | 7689.4 | 8168.4 | 9166.6 |
| K5 V ..... | 7743.9 | 8156.3 | 9093.1 | 7716.3 | 8223.8 | 9181.8 |
| M0 V ..... | 7767.2 | 8205.4 | 9120.2 | 7740.0 | 8279.7 | 9207.8 |
| M6 V ..... | 7837.3 | 8326.2 | 9166.2 | 7812.4 | 8412.7 | 9249.6 |
| L3.5 ..... | 8003.7 | 8669.6 | 9383.5 | 7980.4 | 8779.7 | 9445.2 |
| T6.6 ..... | 8133.6 | 8974.3 | 9772.9 | 8118.1 | 9045.6 | 9788.0 |

already been converted to electrons and therefore 1 ADU ≡ 1 $e^-$.

The default gain settings for WFC and HRC do not sample the full well depth of the CCDs. Both WFC and HRC employ 16 bit analog-to-digit converters (ADCs), which can produce a maximum of $2^{16}$–1 = 65,535 ADU. The largest number of electrons representable by these ADCs is therefore given by gain × $2^{16}$–1. Any charge packet containing more electrons than gain × $2^{16}$–1 will therefore reach digital saturation. At the default gain setting the digital saturation occurs for charge packets of ~65,535 $e^-$ and ~131,072 $e^-$ for the WFC and HRC, respectively.

The physical full well of the CCDs has been measured on the ground with flat-field illumination (Sirianni & Clampin 1999a, 1999b) and on-orbit with observations of star fields (Gilliland 2004). The measured full well is ~84,000 $e^-$ for the WFC and ~165,000 $e^-$ for the HRC, with variations of the order of 10% and 18% in the FOV for the WFC and HRC, respectively (Gilliland 2004). Once the physical saturation is reached, pixels lose their ability to collect additional charges. The additional charge will then spread into adjacent pixels along the same column (blooming). Since in both cameras digital saturation is reached before physical saturation, the use of higher gain settings can be beneficial for very bright objects.

Gilliland (2004) also analyzed the linearity of the response beyond the physical saturation level for both ACS CCDs. They found that with the use of a gain setting that samples the full-well depth, the response of the CCD remains linear well beyond saturation. It is therefore possible to perform <1% accuracy *aperture* photometry of isolated saturated stars by selecting an aperture big enough to contain all pixels that received charge from the saturated pixels. On the other hand, if gain = 1 is set, any information on the charge content of pixels that reached digital saturation is lost. In some cases, however, is still possible

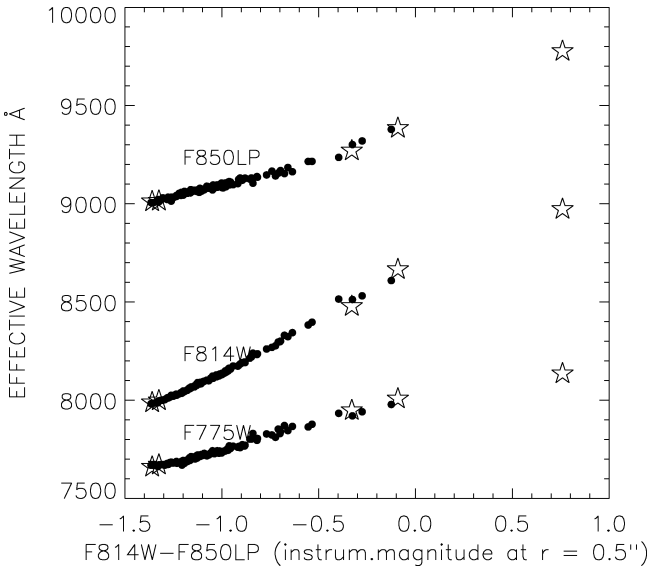


FIG. 11.—Effective wavelength vs. color relation for three near-IR filters of the WFC. The color F814W–F850LP is defined as −2.5 log ([counts $s^{-1}]_{F814W,\ 0''.5}$/[counts $s^{-1}]_{F850LP,\ 0''.5}$), where [counts $s^{-1}]_{filter,\ 0''.5}$ is the count rate within an aperture radius of 0″.5. The filled circles represent the BPGS stellar atlas. The stars represent the five stars used for the EE study.

obtain an estimate (with an accuracy of 2%–10%) of the magnitude of the object (Maíz-Apellániz 2002).

## 6. THE ABSOLUTE FLUX SCALE OF ACS

Considerable effort has been devoted to the determination of accurate response functions for the photometric passbands of ACS. These curves are the product of the characteristic functions of all the individual components in the optical path of the combination of telescope and scientific instrument. In particular, in the case of the ACS, this includes the reflection efficiency of the optical telescope assembly (OTA) and the internal ACS mirrors, the transmission efficiency of the filters, the transmittance of the Dewar window(s), and the quantum efficiency of the detectors. This means that although the HRC and WFC channels share the same filters, the different optimization of the optics and detectors (see § 1) can yield quite different response functions for the same photometric passband. These curves are implemented in SYNPHOT, which is used by the ACS pipeline to populate the image header, to estimate exposure times for ACS observations, and to provide synthetic photometry calibration. The sensitivity curves are also used to translate physical quantities from stellar models, such as isochrones, into the observational plane. The ACS system response curves represent the basis of the ACS synthetic photometric system.

Estimates of the transmission, reflectance, and response of all components of ACS were made on the ground (see Ford et al. 1998). Modifications to the prelaunch response curve, made

by comparison with the observed count rates of spectrophotometric standard stars, are often needed to improve the accuracy of the predicted sensitivity curves.

The first check of the on-orbit sensitivity of the ACS was made during SMOV (Sirianni et al. 2002b). The throughput of the WFC was found to be higher than expected from ground measurements: from a few percent in the red up to ~20% in the blue. Similarly, the HRC sensitivity was higher than predicted in the visual and in the red, but it also showed an unexpected dip in the UV at ~3200 Å. These first observations were used to derive rough corrections to the preflight sensitivity curves for a preliminary SYNPHOT update in 2002 August.

Additional observations have permitted a fine-tuning of these corrections, with an average improvement of ~2% in the uncertainty. The data consist of an extended set of observations of the spectrophotometric standard stars GRW +70 5824 and GD 71, both DA dwarfs, taken between 2002 May and 2003 January. Of these, only GD 71 is a primary *HST* spectrophotometric standard. Its data were collected in 2002 May during the SMOV program, in all filters with both the WFC and HRC cameras. GRW +70 5824 was observed in 2002 July, August, and September through most of the filters with both channels. Additional observations were collected in the course of the *HST* cycle 11: GRW +70 5824 was observed though all WFC filters in 2003 January and all HRC filters in 2003 February. Finally, observations of GRW +70 5824 in the three bluest HRC filters were gathered in 2002 December and 2003 January. In all cases, WFC images were collected by reading out a 512 × 512 subarray around the target, whereas for the HRC the default was a full-frame configuration. In order to remove cosmic-ray hits, at each epoch a pair of images was obtained for each combination of camera and filter. The default gain settings were used for WFC and HRC, namely, 1 and 2. A synopsis of the observations used, with the measured count rates, and a more detailed explanation of the data reduction are given in De Marchi et al. (2004).

All the data have been processed with the standard CALACS pipeline. The analysis was carried out on the geometrically corrected files. Aperture photometry has been performed on the reduced data set as described in § 4.2. In order to calculate precisely the total flux of the standard stars and simultaneously check the stability of the photometric performance of the camera, we chose to perform aperture photometry in all frames from all epochs in a radius smaller than the "infinite" aperture (5.″5). We selected an aperture of 1″ radius (20 pixels for WFC, 40 for HRC). This aperture is large enough to be fairly independent of changes in the PSF core with focus and position on the chip, and to include most of the flux, yet not so large that errors are dominated by the background. The observed count rates in the 1″ radius aperture were converted to an "infinite" aperture by applying the aperture correction calculated from the mean EE profiles.

This analysis has also permitted a first check on the stability of the photometry with time. Since launch, the ACS has proved to be an extremely stable and repeatable instrument. In the selected aperture radius the stability is better than 0.4% for the WFC and better than 0.5% for the HRC. The larger scatter in the HRC is limited in the UV, where the image quality is very sensitive to focus changes, especially in the PSF core. No significant throughput variations are observed in the UV (Boffi et al. 2004).

The observed count rates were compared with the predicted ones using the currently available sensitivity curves of the *HST* ACS system, so that the latter could be updated. Given the photometric stability of the instrument, and in order to reduce the statistical uncertainties associated with the measurement process, all the data for the same combination of detector and filter were averaged together. We also averaged the results of WFC-1 and WFC-2, because the variations between the two are consistent with the temporal variation of the count rate in each chip. We therefore use the standard deviation of the various epochs/chips as a measure of the observational uncertainty.

Although it is not possible to independently measure corrections for any of the sensitivity curves, we decided to hold fixed the mirror reflectivity and window transmission curves, and apply any correction to the detector responsivity quantum efficiency (RQE) or filter throughput. We assumed the wavelength dependence of each filter's throughput curves to be as measured on the ground, and allowed for an overall scaling factor for each filter. Since the same wavelength range is often covered by more than one filter, it was necessary to simultaneously compare observed and predicted count rates over the whole wavelength domain and derive incremental sensitivity updates to be applied simultaneously to all modes. However, since the filters are shared between the two cameras, these scaling factors have been taken as the average of the two corrections (see De Marchi et al. 2004). Finally, although we

TABLE 9
GAIN CORRECTION

| NOMINAL GAIN | AMPLIFIER | GAIN ($e^-$ ADU$^{-1}$) Old | GAIN ($e^-$ ADU$^{-1}$) New | CORRECTION[a] $-2.5 \log (G_{new}/G_{old})$ |
|---|---|---|---|---|
| | | WFC | | |
| 2 ..... | A | 2.018 | 2.002 | 0.0086 |
| | B | 1.960 | 1.945 | 0.0083 |
| | C | 2.044 | 2.028 | 0.0085 |
| | D | 2.010 | 1.994 | 0.0087 |
| 4 ..... | A | 4.005 | 4.011 | −0.0016 |
| | B | 3.897 | 3.902 | −0.0014 |
| | C | 4.068 | 4.074 | −0.0016 |
| | D | 3.990 | 3.996 | −0.0016 |
| | | HRC | | |
| 1 ..... | C | 1.185 | 1.163 | 0.0203 |
| 4 ..... | C | 4.289 | 4.235 | 0.0138 |

[a] Correction to apply to zero points *only* for data retrieved from the *HST* archive before 2004 January 6.

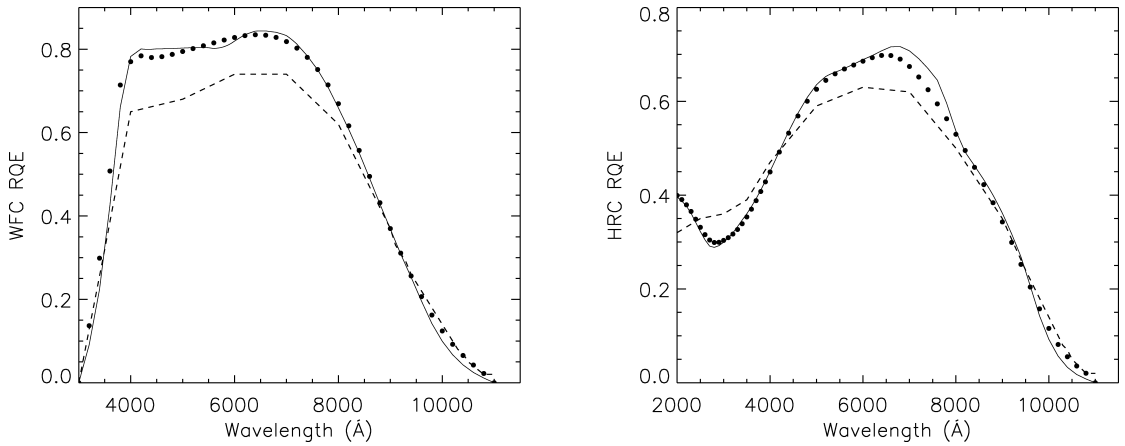


FIG. 12.—Responsive quantum efficiency curves for the WFC (*left*) and HRC (*right*) CCDs. The dashed lines show the preflight measurements, while the dotted lines show the first on-orbit correction (Sirianni et al. 2002a). The final RQE curves resulting from the iterative process are shown as a solid line (De Marchi et al. 2004).

decided to apply all the large-scale corrections to the RQE curves, even if not just detector related, we required the solution to be smooth, without bumps and wiggles. This procedure has been repeated iteratively until convergence. The derived RQE curves (Fig. 12) can now reproduce the count rates in broad-band filters with an accuracy better than 0.5%. The new RQE curves and the corrected filter curves were implemented in the ACS pipeline on 2003 December 10. The new files can be downloaded at the STScI/ACS reference files Web page[17] and were included in the last release of STSDAS.

## 7. ZERO POINTS

The photometric system based on the ACS filters is, by definition, the natural photometric system of ACS. Knowledge of the response of the instrument allows us to define a synthetic system. Synthetic photometry refers to magnitudes and fluxes computed from a spectral energy flux distribution and the response function of a photometric system. The approach taken here deals with the determination of the absolute flux scale of the ACS, as opposed to a conversion from ACS to standard filters. The transformation between ACS and other photometric systems is discussed in § 8.

If $P(\lambda)$ is the dimensionless passband transmission curve in the interval $[\lambda_1, \lambda_2]$, the apparent magnitude of an object with energy flux distribution $f_\lambda(\lambda)$ is

$$m_P = -2.5 \log \frac{\int_{\lambda_1}^{\lambda_2} \lambda f_\lambda P(\lambda)\, d\lambda}{\int_{\lambda_1}^{\lambda_2} \lambda f_\lambda^* P(\lambda)\, d\lambda} + m_P^*, \qquad (3)$$

where $m_P^*$ is a known apparent magnitude from a reference spectrum $f_\lambda^*$. Thus, $f_\lambda^*$ and $m_P^*$ completely define the zero point of a synthetic photometric system.[18]

Several different photometric systems can be defined for the same instrument. For example, the photometric systems based on the WFPC2 filters are the WFPC2 flight system and the synthetic system. The WFPC2 flight system (Holtzman et al. 1995a) is defined such that stars of zero color in the Landolt *UBVRI* system have zero color between any pair of WFPC2 filters, and have the same magnitude in *V* and WFPC2 F555W. In the synthetic photometric system, the zero points were determined so that the magnitude of Vega, when observed through the appropriate WFCP2 filters, would be identical in the closest equivalent filters in the Johnson-Cousins system. This system was later implemented in the STSDAS SYNPHOT package as the VEGAMAG system, in which the zero points are defined by the magnitude of Vega being exactly zero in all filters. The VEGAMAG system, although also related to the absolute flux scale, is designed to resemble closely the standard Johnson-Cousins system.

For the ACS, we present three different versions of a synthetic photometric system. The first is the VEGAMAG system, the analog of the WFPC2 synthetic system implemented in SYNPHOT and the standard-based system. The other two, STMAG and ABMAG, are flux-based systems. Their zero points are defined in terms of a reference flux in physical units rather than the flux of Vega. These two flux-based systems define an *equivalent flux density* for a source, corresponding to the flux density of a source of predefined spectral shape that would produce the observed count rate. The equivalent flux is

[17] Available at: http://www.stsci.edu/hst/acs/analysis/reference_files.

[18] The energy flux distribution $f_\lambda$ in eq. (3) is multiplied by $\lambda/hc$ in order to convert it into photon flux distribution as appropriate for a photon-counting detector.

TABLE 10
SYNTHETIC ZERO POINTS FOR WFC

| Filter | VEGAMAG | ABMAG | STMAG |
|---|---|---|---|
| F435W ..... | 25.779 | 25.673 | 25.157 |
| F475W ..... | 26.168 | 26.068 | 25.757 |
| F502N ..... | 22.352 | 22.271 | 22.084 |
| F550M ..... | 24.867 | 24.892 | 24.934 |
| F555W ..... | 25.724 | 25.718 | 25.672 |
| F606W ..... | 26.398 | 26.486 | 26.655 |
| F625W ..... | 25.731 | 25.898 | 26.206 |
| F658N ..... | 22.365 | 22.747 | 23.148 |
| F660N ..... | 21.389 | 21.676 | 22.081 |
| F775W ..... | 25.256 | 25.654 | 26.393 |
| F814W ..... | 25.501 | 25.937 | 26.776 |
| F850LP ..... | 24.326 | 24.862 | 25.954 |
| F892N ..... | 21.865 | 22.371 | 23.429 |

TABLE 11
SYNTHETIC ZERO POINTS FOR HRC

| Filter | VEGAMAG | ABMAG | STMAG |
|---|---|---|---|
| F220W ..... | 21.871 | 23.553 | 21.627 |
| F250W ..... | 22.288 | 23.724 | 22.201 |
| F330W ..... | 22.904 | 24.085 | 23.026 |
| F344N ..... | 20.439 | 21.588 | 20.574 |
| F435W ..... | 25.185 | 25.095 | 24.575 |
| F475W ..... | 25.623 | 25.527 | 25.230 |
| F502N ..... | 21.906 | 21.826 | 21.638 |
| F550M ..... | 24.392 | 24.416 | 24.457 |
| F555W ..... | 25.255 | 25.248 | 25.200 |
| F606W ..... | 25.893 | 25.976 | 26.134 |
| F625W ..... | 25.195 | 25.359 | 25.662 |
| F658N ..... | 21.803 | 22.185 | 22.585 |
| F660N ..... | 20.827 | 21.116 | 21.516 |
| F775W ..... | 24.551 | 24.945 | 25.675 |
| F814W ..... | 24.849 | 25.287 | 26.141 |
| F850LP ..... | 23.850 | 24.388 | 25.502 |
| F892N ..... | 21.366 | 21.870 | 22.928 |

then converted into a magnitude by using a constant chosen such that the magnitude in the $V$ band corresponds roughly to that in the Johnson system. The advantage of the ABMAG and STMAG magnitude systems is that the magnitude is directly related to physical units, and they are therefore much simpler and cleaner. The basic equation in their definition is the *mean flux density* per unit wavelength, $f_\lambda$ (STMAG), or per unit frequency, $f_\nu$ (ABMAG). The choice between flux-based and standard-based system is mostly a matter of personal preference.

The zero point of an instrument, by definition, is the magnitude of an object that produces 1 count per second. We use this definition and SYNPHOT to calculate the zero points in this paper. Any zero point must refer to a count rate measured in a specific way. In this paper they refer to a nominal "infinite" aperture of 5.″5 radius. Independently of the different definitions, the magnitude in the bandpass $P$ in any of the ACS systems is given by

$$\begin{aligned}\mathrm{ACSMAG}(P) &= -2.5 \log (\text{total count rate } [e^- \text{ s}^{-1}]) + \mathrm{Zpt}(P) \\ &= \mathrm{OBMAG}(P) + \mathrm{Zpt}(p), \end{aligned} \quad (4)$$

and the choice of the zero point Zpt($P$) determines the photometric system of ACSMAG.

### 7.1. VEGAMAG Magnitude System

The VEGAMAG system makes use of Vega ($\alpha$ Lyr) as the standard star. Calibrated empirical spectra are available covering the wavelength range from 3300 Å to 1.05 $\mu$m (Hayes 1985). Bohlin et al. (1990) have extended this spectral coverage down to 1150 Å using *International Ultraviolet Explorer* (*IUE*) spectra. Since its initial release, SYNPHOT adopted as reference the synthetic spectrum of Vega computed by Kurucz (1993) models with a normalization at $V = +0.034$ mag, assuming 3670 Jy for $V = 0$. Composite spectra of Vega have been constructed by assembling empirical and synthetic spectra (e.g., Colina et al. 1996). The most recent absolute calibration of Vega from the far-UV to the IR is a composite spectrum with *IUE* data from 1140 to 1700 Å and *HST* STIS from 1700 to 4200 Å (Bohlin & Gilliland 2004). Longward of 4200 Å, the Kurucz[19] model of Vega is used. The normalization has been done to the observed flux level of $3.46 \times 10^{-9}$ ergs cm$^{-2}$ s$^{-1}$ Å$^{-1}$ at 5556 Å, corresponding to $V = 0.026$. Since this new spectrum has been adopted as the Vega reference spectrum in SYNPHOT, we decided to use it to calculate the zero points for the ACS VEGAMAG system.

In the VEGAMAG system, by definition, Vega has magnitude 0 in all filters. Since the zero points in all VEGAMAG systems are tied to the observed Vega fluxes, their synthetic absolute magnitude may have systematic errors (probably up to 2%). Smaller errors, however, are expected in the colors. The values of the VEGAMAG Zpt($P$) are listed in Tables 10 and 11 for both the WFC and HRC filters.

### 7.2. STMAG Magnitude System

The STMAG magnitude system (Koorneef et al. 1986) is based on the definition of mean flux density per unit wavelength as

$$f_\lambda(P) \equiv \frac{\int f_\lambda P(\lambda) \lambda \, d\lambda}{\int P(\lambda) \lambda \, d\lambda}, \quad (5)$$

and the selection of a flat reference spectrum in $f_\lambda$, where $f_\lambda$ is expressed in ergs s$^{-1}$ cm$^{-2}$ Å$^{-1}$. The magnitudes in the STMAG system are given by

$$\mathrm{STMAG}(P) = -2.5 \log [f_\lambda(P)] + K. \quad (6)$$

[19] See the Kurucz Web page: http://kurucz.harvard.edu.

The zero point $K$ is defined by setting the magnitude of a source that has a flux density of 1 erg s$^{-1}$ cm$^{-2}$ Å$^{-1}$ to $-21.10$. Another way to express this zero point is to say that an object with a flux density of $3.631 \times 10^{-9}$ ergs cm$^{-2}$ s$^{-1}$ Å$^{-1}$ will have magnitude STMAG $= 0$ in every filter.

Historically, the spectral flux density per unit wavelength that would generate 1 count s$^{-1}$ (within the nominal infinite aperture defined above) is stored in *HST* image headers as the keyword entry PHOTFLAM. Calling PHOTFLAM($P$) the value of PHOTFLAM for the passband $P$, to directly convert count rates to average flux density

$$f_\lambda(P) = \text{PHOTFLAM}(P) \times (\text{count rate}),$$

where the count rate is in $e^-$ s$^{-1}$. The value of PHOTFLAM($P$) can be derived directly by the passband function $P(\lambda)$,

$$\text{PHOTFLAM}(P) = \frac{hc/A}{\int P(\lambda)\lambda\, d\lambda},$$

where $A$ is the telescope collecting area in square centimeters. We list the value of PHOTFLAM($P$) for all ACS filters in Tables 1 and 2. These values are also reported in the photometry keyword section in the header of the SCI extension of the calibrated ACS FITS file.

Thus, following the standard definition of any zero point, the STMAG zero point is

$$\text{STMAGZpt}(P) = -2.5 \log [\text{PHOTFLAM}(P)] - 21.10,$$

and the STMAG is therefore defined as

$$\begin{aligned}\text{STMAG}(P) &= -2.5 \log [f_\lambda(P)] - 21.10 \\ &= -2.5 \log (\text{total counts} \times \text{s}^{-1}) \\ &\quad + \text{STMAGZpt}(P). \end{aligned} \tag{7}$$

The STMAGZpt($P$) are listed in Tables 10 and 11 for both WFC and HRC filters.

### 7.3. ABMAG Magnitude System

The ABMAG magnitude system is the analog of STMAG for a constant flux density per unit frequency $f_\nu$ (Oke 1964). The reference spectrum is flat in $f_\nu$ expressed in ergs s$^{-1}$ cm$^{-2}$ Hz$^{-1}$. The magnitudes in the ABMAG system are given by

$$\text{ABMAG}(P) = -2.5 \log [f_\nu(P)] - 48.60. \tag{8}$$

The constant is chosen so that ABMAG matches the Johnson $V$ magnitude for an object with a flat spectrum. Another way to express this zero point is to say that an object with a flux density of $3.631 \times 10^{-20}$ ergs cm$^{-2}$ s$^{-1}$ Hz$^{-1}$ will have magnitude ABMAG $= 0$ in every filter. There is a simple relation between the STMAG and the ABMAG due to their own definition ($f_\lambda = f_\nu c/\lambda^2$) and the pivot wavelength definition,

$$\lambda_p(P) \equiv \sqrt{\frac{cf_\nu(P)}{f_\lambda(P)}} = \sqrt{\frac{\int P(\lambda)\lambda\, d\lambda}{\int P(\lambda) d\lambda/\lambda}}.$$

Thus, STMAG can be converted into ABMAG as

$$\text{ABMAG}(P) = \text{STMAG}(P) - 5 \log \lambda_p(P) + 18.6921, \tag{9}$$

where $\lambda_p$ is in Å. This can also be rewritten as

$$\text{ABMAG}(P) = \text{STMAG}(P) - 5 \log [\lambda_p(P)/5475.4]; \tag{10}$$

therefore, the two flux-based systems will give the same magnitude at $\lambda = 5475.4$ Å. This transformation provides an easy way to calculate the zero points in the ABMAG system starting from PHOTFLAM($P$):

$$\begin{aligned}\text{ABMAGZpt}(P) = &-2.5 \log [\text{PHOTFLAM}(P)] \\ &-21.10 - 5 \log \lambda_p(P) + 18.6921.\end{aligned}$$

Equation (9) can therefore be rewritten as

$$\begin{aligned}\text{ABMAG}(P) &= -2.5 \log (\text{total counts} \times \text{s}^{-1}) \\ &\quad + \text{ABMAGZpt}(P). \end{aligned} \tag{11}$$

ACS ABMAGZpt($P$) are listed in Tables 10 and 11 for both WFC and HRC filters.

## 8. PHOTOMETRIC TRANSFORMATIONS

Since the ACS filters do not have exact counterparts in any other "standard" filter set, we strongly recommend that ACS photometric results be referred to a system based on its own filters. Sensitivity curves can be used to translate physical quantities from stellar models, such as surface luminosity and effective temperature $T_{\rm eff}$, into the ACS observational plane. This conversion is done by means of a bolometric correction and $T_{\rm eff}$-color relations. For example, Girardi et al. (2002) have published theoretical bolometric corrections and color transformations for any broadband photometric system and have converted several sets of Padova isochrones into the ACS photometric system (L. Girardi 2003, private communication). Bedin et al. (2004) transformed the entire set of evolutionary models by Pietrinferni et al. (2004) into the WFC observational photometric system. The total throughput curves of the ACS cameras[20] can be implemented in the isochrone synthesis code

[20] ACS performance data available at http://acs.pha.jhu.edu/instrument/photometry.

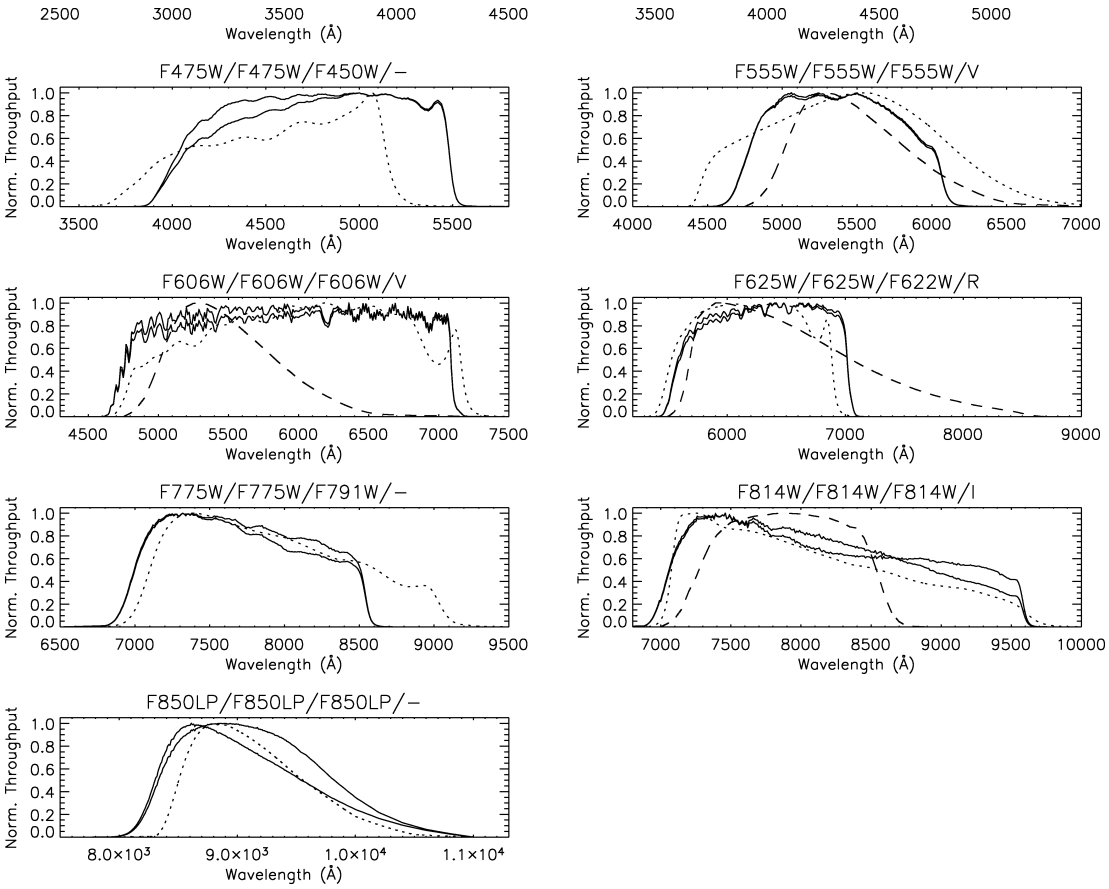


FIG. 13.—Comparison between the total response curve for several filters of the WFC (*solid thick line*), HRC (*solid thin line*), WFPC2 (*dotted line*), and the LANDOLT filters (*dashed line*). All curves have been normalized to their peak value. The title of each panel shows the name of the filter (WFC, HRC, WFPC2, and LANDOLT).

of Bruzual & Charlot (2003) to compute the spectral evolution of stellar populations directly in the ACS observational plane.

Transformation between even nominally similar photometric systems presents difficult and poorly understood problems (Young 1993). Manfroid & Sterken (1992) identify two kinds of error associated with the transformations: *Conformity errors* that arise from the fact that passbands in two systems are different, and there is no rigorous way to evaluate the corrections needed to properly transform data from one system to another; and *reduction errors*, caused by incorrect values in the estimated transformation coefficients due to inevitable measurement errors.

In the traditional empirical approach, the difference between a magnitude in the natural system and the "standard" system is plotted against a convenient color index, and the fit is performed using a straight line or a low-order polynomial. This approach has numerous problems. It requires many accurate observations of standard stars, which might not be feasible (for example in the case of *HST*). Moreover, the validity of the obtained transformations will always be limited to a homogeneous group of stars. Different fitting functions are required for reddened stars, for metal-poor (or metal-rich) stars, and for such effects as age, rotation, magnetic field, etc. Furthermore, in order to increase the throughput at the central wavelength and make the entire system more efficient, modern filter transmission curves are steep-sided and ripple-topped (see, for example, the comparison between ACS and *UBVRI* filters or even between ACS and WFPC2 in Fig. 13). This adds enormously to the complexity of the color-transformation problems (Sterken & Manfroid 1992), because the transformations become even more sensitive to spectral features.

A photometric transformation theory has been developed in the last 30 years that tries to find a mathematical relation between integrals involving various functions, such as the spectral response of the instrument, and the spectral distribution of stellar flux (Young 1992a, 1992b, 1994; Sterken & Manfroid 1992). Although these methods have been very useful in identifying several causes of conformity errors, they have shown that an exact solution is not possible for existing photometric systems. It is, however, important to note some of their con-

clusions. Although high-order terms are usually absent from low-order empirical transformations, they are responsible for significant systematic errors (Young 1992a). These high-order terms are not linear functions of a color index, but involve both higher power and cross products of color, curvature, and derivative-like indices. Those terms are different for objects with different spectra. To accurately estimate the high-order terms, a better sampling of the wavelength space is required, with overlapping bands. Two ideal systems are exactly transformable if the passbands of one are linear combinations of the passbands of the other; i.e., bandpasses need to overlap with each filter peak close to the steepest slope of the neighbors (Young 1992a). All existing photometric systems, including the ACS, are undersampled and consequently nontransformable.

Finally, Manfroid et al. (1992) have also discussed the errors that arise from the use of any color transformation for stars having color indices that fall outside the range of stars used to derive the transformations. These authors show the inherent difficulty of this approach for peculiar objects such as Wolf-Rayet stars, luminous blue variables, cataclysmic variables, supernovae, and quasars.

Although some of the passbands of ACS will eventually establish a standard in their own right, the scientific community, at least initially, will sometimes require a comparison of observations obtained through ACS passbands with those obtained in other systems. In the following pages we provide the coefficients to translate ACS photometry to other well-known photometric systems. They should be used with extreme caution. Internal consistency between the WFC and HRC photometry is achieved by the provided transformation between the two systems. We also provide conversion from ACS to WFPC2 and from ACS to the Landolt *UBVRI* photometric system. ACS also has a subset of the SDSS filters; the conversion to this system will be presented in a separate paper.

In general, transformations between two different photometric systems rely on the spectral energy distribution of the targeted objects as well as the absolute response function of the instruments. There are two routes to establishing the transformations. One approach is to make direct use of observations of the same object (typically stars in well-studied globular clusters) in the two systems. In principle, this straightforward determination is believed to provide an unbiased approximation to the real shape of the transformation curve (for the selected stars) and can be directly used without any knowledge of the instrumental throughputs. However, because of the limited *HST* time that can be allocated to calibration programs, the current database of ACS observations is still insufficient to produce transformations that are valid over a large color range. In the future, this deficiency will be remedied as more and more ACS data become public.

The other method is to deduce transformation curves based on synthetic photometry. This method takes advantage of the well-established response curves of the ACS and the BPGS catalog of stellar spectra. The transformations obtained in this way can span much wider color ranges, but their accuracy is, of course, limited by the fidelity of the ACS throughput curves and the quality of the spectra in the atlas. Here we present the results from both approaches and show that in most cases the transformations using these two approaches are consistent with each other. Therefore, synthetic transformations based on larger color range can be safely employed and should be considered the norm, unless otherwise indicated.

Although the current WFC and HRC throughput curves can predict the observed count rates of the spectrophotometric standard stars with an accuracy of ~1%, strictly speaking they are valid for the specific stellar properties of the standard star used. When the transformation coefficients presented in this paper are employed, the different spectral shapes (e.g., due to surface gravity, metallicity, extinction, redshift, etc.) of the targets under investigation must be taken into account. Passband differences may not be evident from the photometry of the object used to derive the transformations. If these transformations are used for bluer or redder objects, for objects with different gravities, or for any object not well represented by the targets used to derive the transformations, then systematic magnitude differences are possible (see also Bessel 1990; Holtzman et al. 1995a).

### 8.1. General Notes

In the following sections we define SOURCE (S) as the photometric system of the observed data that we want to transform, and TARGET (T) as the photometric system after the transformation. Following this definition, SMAG is the magnitude in the SOURCE system, and TMAG and TCOL are the magnitude and color in the TARGET system. Since several photometric systems can be defined for each instrument, we need to clarify the default magnitude system used in the following transformations. In order to minimize the possible confusion and reduce the redundancy among different zero points, we only provide OBMAG-to-OBMAG (see eq. [1]) transformations, except for the transformation to the Landolt photometric system. The OBMAG-to-OBMAG transformations can be used to convert magnitudes to any photometric system by simply subtracting (adding) the corresponding zero points before (after) the transformation. We present an example in Appendix D.1.

The transformations have the following format:

$$\mathrm{TMAG} = \mathrm{SMAG} + c0 + c1 \times \mathrm{TCOL} + c2 \times \mathrm{TCOL}^2, \tag{12}$$

where SMAG is the OBMAG in the source system, and TMAG and TCOL are the OBMAG magnitude and color (as difference of two OBMAGs) in the target system, and $c0$, $c1$, and $c2$ are the coefficients for the transformation. Please note that in the transformation equation the color term is in the TARGET system and not in the SOURCE system. The same approach was

used by Holtzman et al. (1995a) for the transformations from WFCP2 to *UBVRI*, since this formalism carries several advantages, as discussed by Stetson (1992). Consequently, TCOL must be derived iteratively using ACS observations in two colors unless the target color is known.

The number of objects used for the observational transformations varies greatly depending on the area of the FOV, the photometric quality of the data, and the brightness of the stars. Photometric errors have been used as initial criteria to select stars for the transformations. Depending on the numbers of stars available, the error threshold was set between 0.02 and 0.06 mag. We divided the color range in equally sized bins and calculated the median and standard deviation for each bin. Outliers have been rejected based on the local median and standard deviation, using a $\sigma$-clipping criterion. In transformation plots where observed stars are used, we show only representative points that are just local medians in any given color bin.

To estimate the uncertainties of the transformation parameters, we followed the approach employed by Holtzman et al. (1995a). For transformations derived from the observational data, we weighted stars equally and iterated the $\chi^2$ minimization by adjusting the magnitude errors until $\chi^2$ reached unity. In order to avoid overestimation of the uncertainty of synthetic stars, we measured the scatter from the fit and used this as a weight for the $\chi^2$ minimization. This procedure not only prevents the fit from being partially weighted by a few bright stars, but also provides realistic errors that are not modeled by synthetic photometry.

In deriving the transformation between two photometric systems, the functional form of the transformation should be addressed. Although in principle a quadratic least-squares fit is preferable, we found that for observational transformations, given the limited color range and limited statistics, a linear fit was more appropriate. In the case of observational transformations between the CCD cameras of the ACS that use the same filters, we also decided to perform a linear least-squares fitting with iterative rejection. For all synthetic transformations we performed a quadratic least-squares fitting.

A single set of coefficients does not always fit the data over the large color range of the stellar atlas. Sudden differences in the response curves can produce discontinuities in the color term dependencies and force us to limit the color range for which a set of coefficients can be used. When this happens, we divide the color range into two regions and provide separate coefficients for each segment.

Finally, the precision of the synthetic transformations depends on the accuracy of the total response function of the photometric passbands of ACS. As we discussed in § 6, a fairly significant revision of the prelaunch RQE has been necessary in order to reproduce the observed on-orbit sensitivity. Although the derived RQE curves can now reproduce the count rates in all broadband filters with an accuracy better than 0.5%, it is possible that the shape of the total response of the bluest and reddest passbands is not a perfect representation of the real response curve. This could introduce systematic errors in the color transformations. In these cases (F435W and F850LP for the WFC, and F220W and F850LP for the HRC), we suggest using the observed transformations, if available.

### 8.2. ACS Internal Transformations

The WFC and the HRC share all the visual and near-IR filters of the ACS. The transformation between the two systems is therefore expected to be quite simple. However, the different optimization of the cameras (mirrors and CCDs) produces different total throughput curves, in particular in the blue and near-IR (Fig. 13). Therefore, the transformation between filters in these wavelength regions could have a significant dependence on the color term.

For these "internal" transformations between the two CCD cameras, we used observations of two globular clusters, NGC 104 (programs 9018, 9656, and 9666) and NGC 2419 (program 9666). These globular clusters have very different metallicities ([Fe/H] $\sim -0.7$ for NGC 104 and [Fe/H] $\sim -2.2$ for NGC 2419), essentially spanning the whole metallicity distribution of the Galactic globular cluster system.

The raw data have been processed through the CALACS pipeline at the STScI. For moderately crowded fields ($\sim 6'$ west of the core) of NGC 104, we simply performed 5 pixel radius aperture photometry using the IRAF APPHOT package. Because the NGC 104 data were originally acquired for the assessment of the geometric distortion and low-frequency residuals in the flat field, each filter observation consists of multiple pointings offsets by large dithers. We decided to select only stars present in at least three pointings and to use the $\sigma$-clipped averages of the magnitude in the multiple observations as an estimate of the brightness of the star.

The photometry of NGC 2419 required more complicated field-dependent handling. Due to the larger distance of the cluster, a single pointing of WFC covers both the compact core and the moderately crowded outer regions. In the external regions of NGC 2419 we can safely perform 5 pixel radius aperture photometry. However, PSF-fitting photometry is required for the crowded region of NGC 2419 common to the HRC and WFC. While the PSF of the HRC can be assumed to be nearly constant across the field, the PSF varies significantly across the WFC FOV (see § 4.2), thus preventing us from applying in the crowded area the PSF extracted from isolated stars in the external regions. We confirmed this fact by performing our initial PSF photometry assuming a spatially constant PSF; the result showed systematic errors up to $\sim$4%. Although in principle a PSF can be iteratively constructed even for an extremely crowded field, the task of achieving calibration-quality photometry becomes prohibitively impractical if not impossible. An alternative is to use Tiny Tim (see footnote 14) to model the PSF on the crowded area. However, it is difficult to determine the time-varying behavior of the PSF,

mainly due to focus offset changes. Besides, most PSF photometry packages cannot readily make use of PSF images from Tiny Tim. We therefore decided to create position-dependent PSF templates using the sparser observations of NGC 104. The PSFs were easily sampled from isolated stars over the entire field of view and then applied to the NGC 2419 field. In order to avoid effects due to PSF time variations, when possible we used the NGC 104 images that were closest to the date of the NGC 2419 observations. After checking the residuals in PSF-subtracted images as well as various goodness-of-fit criteria, such as $\chi^2$, best matching PSF templates were determined for each filter. This technique allowed us to remove any systematic effect on the photometry of the crowded regions.

Examining the NGC 104 and NGC 2419 data separately, one does not see strong evidence for a metallicity dependence in the transformation relations. Due to the different metallicities and distance moduli of the two clusters [$(m - M) = 13.27$ for NGC 104 (Zoccali et al. 2001) and $(m - M) = 19.88$ for NGC 2419 (Harris et al. 1997)] the range of colors that our selection criteria allow are not the same in both clusters. In particular, for NGC 2419 we used stars on the horizontal branch, the asymptotic giant branch, and on the red and subgiant branches. The NGC 104 data allow an extension to the red, since we can use main-sequence stars at least 4 mag fainter than the turnoff point.

Figure 14 shows the observed color-magnitude diagrams (CMDs) for the two clusters for the WFC and HRC. In order to look for metallicity effects, we must compare stars of similar colors in the two clusters. In most transformations, the data of the two clusters overlap only in a quite narrow color range spanning $\leq$0.6 mag. We therefore used the model atmospheres of Kurucz (1993) to investigate the metallicity dependency. We compared synthetic transformations using three different metallicities, [Fe/H] = 0, $-0.5$, and $-2.0$, and find that in the color range covered by the observational data, the systematic differences between the three metallicities are at most 0.3%. We therefore decided to combine the data for both clusters and also include the observations of the two spectrophotometric standards to determine the final transformations.

Even when combining all the observational data, the color range covered by all the stars (WDs+NGC 2419+NGC 104) were generally limited to $0.0 < \mathrm{F435W} - \mathrm{F555W} < 1.2$ or $-0.4 < \mathrm{F555W} - \mathrm{F814W} < 1.2$ in the HRC VEGAMAG system; the transformation from observed stars cannot be assumed to be corrected for stars outside this color range. Synthetic transformations cover a larger color range and should be used instead.

We list the transformation coefficients to use in equation (12) for different combinations of most of the full-sized filters in Tables 12 and 13 for the transformations from WFC to HRC and from HRC to WFC, respectively. The transformations between the primary filters from WFC to HRC are shown in Figure 15.

These figures show that the synthetic system matches the observations fairly well, usually within 1% for all stars within the range of colors in which our observations were made. There are, however, a few cases, F435W and F625W for example, where the discrepancy can rise up to a couple of percent for the reddest stars. In principle, one could argue that since the long-wavelength light scattering is more severe in the HRC than in the WFC, an incorrect aperture correction could be the reason for this discrepancy. However, this is not the case, because these filters are not affected by this problem, which starts at $\lambda > 7000$ Å. Also, the near-IR filters, which suffer from extended PSF wings, and therefore could be more affected by aperture correction errors, do not show any systematic differences.

Although the BPGS atlas does not include stars with high surface gravities, but only main-sequence stars and giants, the agreement with the two spectrophotometric white dwarfs does not show any systematics. This analysis suggests that we have a good understanding of the ACS synthetic system and that the derived transformations are accurate to 1%–2% or better in all filters. The synthetic curves can thus be used in place of the observational ones to produce transformations for objects with spectra different from the observed stars.

### 8.3. Transformations from ACS to *UBVRI*

ACS filters differ significantly from the *UBVRI* bandpasses. The ACS filters are usually narrower, start at shorter wavelengths, and, apart from F814W, extend less to the red (see Fig. 13). As a consequence, the transformations between the two systems may be very sensitive to details in the underlying stellar spectrum and show strong dependencies on metallicity and surface gravity.

We compared ACS observations with ground-based photometry of NGC 2419. In particular, we retrieved *BVRI* data from the Stetson Web page,[21] and an independent *BVRI* data set was provided by Saha et al. (2005). The two NGC 2419 photometric control data sets are the same as recently used to examine the accuracy of the WFPC2 zero points (Heyer et al. 2002, 2004). The two observational CMDs from the two different sources are shown in Appendix D.2, Figure 20. In order to have a large number of common stars in the HRC and WFC FOV, ACS observations were centered in a region fairly close to the center of NGC 2419. As a consequence, the match with ground observations—centered in a more sparse region—resulted in only 30–60 stars, depending on the filter and camera.

We compare the two NGC 2419 control data sets and find a significant color term between them: red stars tend to be brighter in Stetson's (see footnote 19) than in Saha et al. (2005), with differences up to 3%–4% for stars with $V - I > 1.0$ in the *I* band. Such differences, also discussed in Saha et al. (2005), could be due to different filter throughput curves, red-leak control, and systematic effects in the transformation from the in-

[21] See http://cadcwww.hia.nrc.ca/cadcbin/wdb/astrocat/stetson/query.

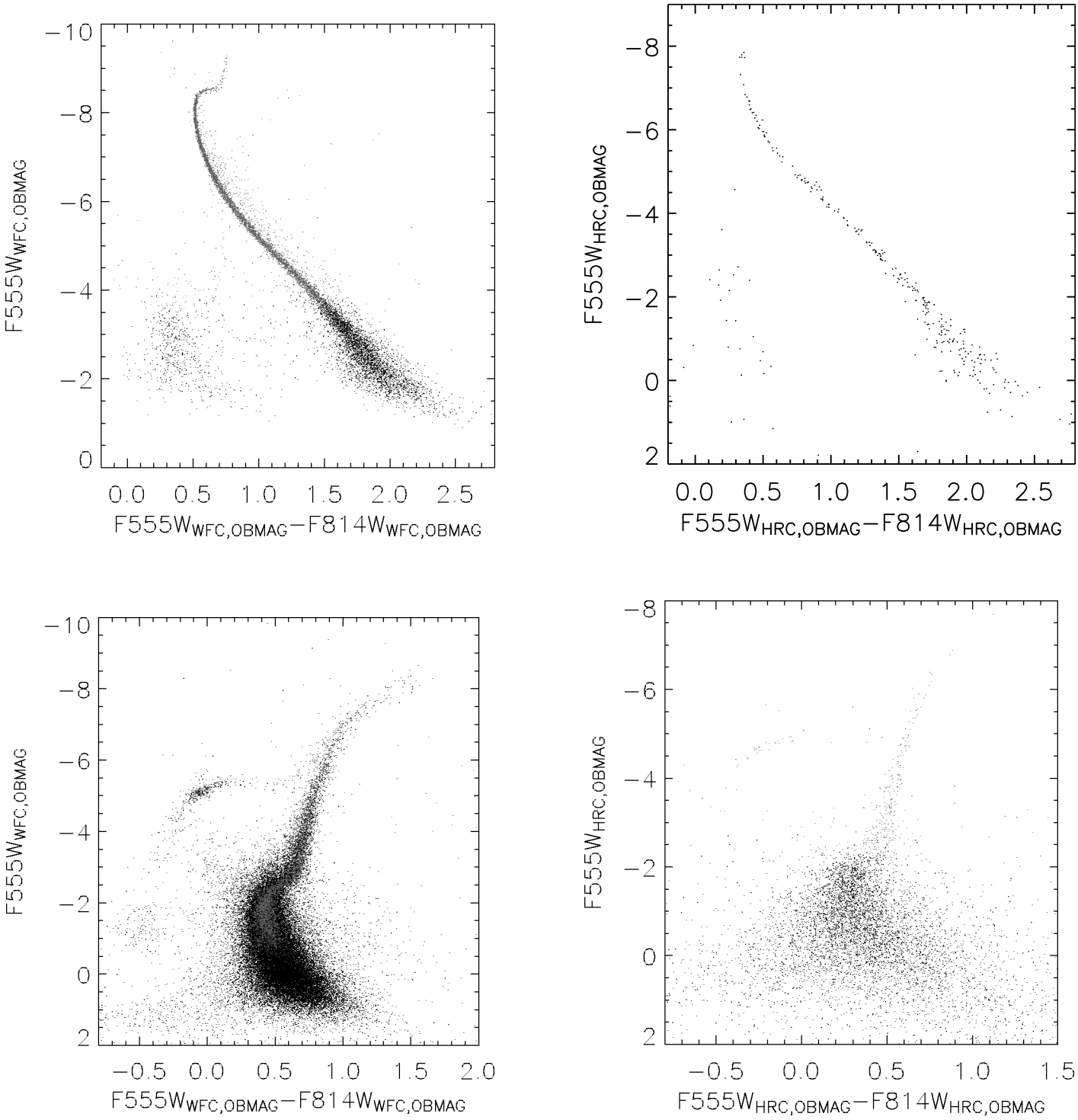


FIG. 14.—Observed CMDs for NGC 104 (*top*) and NGC 2419 (*bottom*) with WFC (*left*) and HRC (*right*). [*See the electronic edition of the PASP for a color version of this figure*.]

TABLE 12
COEFFICIENTS FOR THE TRANSFORMATION FROM WFC TO HRC

| SOURCE | TARGET | | OBSERVED | | | SYNTHETIC | | | |
|---|---|---|---|---|---|---|---|---|---|
| SMAG | TMAG | TCOL | c0 | c1 | c2 | c0 | c1 | c2 | TCOL Range[a] |
| F435W ..... | F435W | F435W−F475W | 0.580 ± 0.061 | 0.018 ± 0.088 | 0.000 ± 0.000 | 0.525 ± 0.042 | 0.273 ± 0.227 | −0.266 ± 0.299 | <0.5 |
| | | | | | | 0.592 ± 0.008 | 0.007 ± 0.016 | −0.014 ± 0.008 | >0.5 |
| | F435W | F435W−F550M | | | | 0.584 ± 0.073 | −0.046 ± 0.154 | −0.043 ± 0.080 | <−0.7 |
| | | | | | | 0.589 ± 0.001 | −0.007 ± 0.002 | −0.002 ± 0.002 | >−0.7 |
| | F435W | F435W−F555W | 0.591 ± 0.031 | 0.009 ± 0.044 | 0.000 ± 0.000 | 0.592 ± 0.002 | 0.047 ± 0.035 | −0.011 ± 0.159 | <0.1 |
| | | | | | | 0.593 ± 0.003 | −0.001 ± 0.005 | −0.005 ± 0.002 | >0.1 |
| | F435W | F435W−F606W | 0.586 ± 0.059 | 0.006 ± 0.040 | 0.000 ± 0.000 | 0.565 ± 0.028 | 0.044 ± 0.115 | −0.003 ± 0.112 | <0.7 |
| | | | | | | 0.596 ± 0.005 | −0.002 ± 0.005 | −0.001 ± 0.001 | >0.7 |
| | F435W | F435W−F625W | 0.592 ± 0.032 | 0.005 ± 0.031 | 0.000 ± 0.000 | 0.593 ± 0.003 | 0.023 ± 0.025 | −0.019 ± 0.060 | <0.1 |
| | | | | | | 0.594 ± 0.003 | −0.003 ± 0.003 | −0.001 ± 0.001 | >0.1 |
| | F435W | F435W−F775W | 0.591 ± 0.020 | 0.004 ± 0.020 | 0.000 ± 0.000 | 0.602 ± 0.027 | 0.008 ± 0.063 | −0.008 ± 0.034 | <−0.5 |
| | | | | | | 0.593 ± 0.002 | −0.007 ± 0.002 | 0.001 ± 0.000 | >−0.5 |
| | F435W | F435W−F814W | 0.591 ± 0.031 | 0.007 ± 0.025 | 0.000 ± 0.000 | 0.599 ± 0.011 | 0.013 ± 0.038 | −0.006 ± 0.030 | <−0.2 |
| | | | | | | 0.595 ± 0.002 | −0.007 ± 0.002 | 0.001 ± 0.000 | >−0.2 |
| | F435W | F435W−F850LP | 0.596 ± 0.010 | 0.004 ± 0.011 | 0.000 ± 0.000 | 0.618 ± 0.067 | 0.018 ± 0.080 | −0.000 ± 0.023 | <−1.2 |
| | | | | | | 0.590 ± 0.001 | −0.005 ± 0.001 | 0.001 ± 0.000 | >−1.2 |
| F475W ..... | F475W | F435W−F475W | 0.564 ± 0.029 | −0.054 ± 0.042 | 0.000 ± 0.000 | 0.578 ± 0.004 | −0.087 ± 0.009 | 0.017 ± 0.005 | … |
| | F475W | F475W−F550M | | | | 0.489 ± 0.002 | −0.041 ± 0.006 | 0.003 ± 0.004 | … |
| | F475W | F475W−F555W | 0.519 ± 0.017 | −0.025 ± 0.078 | 0.000 ± 0.000 | 0.521 ± 0.001 | −0.063 ± 0.003 | 0.005 ± 0.008 | … |
| | F475W | F475W−F606W | 0.543 ± 0.036 | −0.026 ± 0.044 | 0.000 ± 0.000 | 0.560 ± 0.002 | −0.057 ± 0.004 | 0.012 ± 0.002 | … |
| | F475W | F475W−F625W | 0.522 ± 0.013 | −0.015 ± 0.026 | 0.000 ± 0.000 | 0.532 ± 0.001 | −0.030 ± 0.002 | 0.002 ± 0.001 | … |
| | F475W | F475W−F775W | 0.519 ± 0.010 | −0.010 ± 0.014 | 0.000 ± 0.000 | 0.526 ± 0.004 | −0.019 ± 0.012 | −0.000 ± 0.007 | <−0.1 |
| | | | | | | 0.523 ± 0.002 | −0.023 ± 0.002 | 0.005 ± 0.001 | >−0.1 |
| | F475W | F475W−F814W | 0.523 ± 0.010 | −0.009 ± 0.012 | 0.000 ± 0.000 | 0.532 ± 0.007 | −0.019 ± 0.021 | −0.001 ± 0.014 | <−0.2 |
| | | | | | | 0.531 ± 0.002 | −0.024 ± 0.002 | 0.004 ± 0.000 | >−0.2 |
| | F475W | F475W−F850LP | 0.518 ± 0.014 | −0.012 ± 0.013 | 0.000 ± 0.000 | 0.510 ± 0.072 | −0.026 ± 0.075 | −0.003 ± 0.019 | <−1.4 |
| | | | | | | 0.514 ± 0.001 | −0.015 ± 0.001 | 0.003 ± 0.000 | >−1.4 |
| F555W ..... | F555W | F435W−F555W | 0.479 ± 0.025 | −0.010 ± 0.034 | 0.000 ± 0.000 | 0.470 ± 0.001 | 0.003 ± 0.002 | −0.000 ± 0.001 | … |
| | F555W | F475W−F555W | 0.465 ± 0.012 | −0.025 ± 0.046 | 0.000 ± 0.000 | 0.472 ± 0.001 | 0.006 ± 0.002 | 0.001 ± 0.005 | … |
| | F555M | F550M−F555W | | | | 0.482 ± 0.020 | −0.011 ± 0.057 | −0.004 ± 0.040 | … |
| | F555W | F555W−F606W | 0.487 ± 0.066 | −0.023 ± 0.077 | 0.000 ± 0.000 | 0.459 ± 0.006 | 0.020 ± 0.011 | −0.006 ± 0.004 | … |
| | F555W | F555W−F625W | 0.473 ± 0.019 | −0.011 ± 0.047 | 0.000 ± 0.000 | 0.470 ± 0.001 | 0.006 ± 0.004 | −0.002 ± 0.002 | … |
| | F555W | F555W−F775W | 0.466 ± 0.014 | −0.006 ± 0.025 | 0.000 ± 0.000 | 0.472 ± 0.001 | 0.003 ± 0.001 | −0.001 ± 0.000 | … |
| | F555W | F555W−F814W | 0.472 ± 0.015 | −0.007 ± 0.021 | 0.000 ± 0.000 | 0.471 ± 0.001 | 0.003 ± 0.001 | −0.000 ± 0.000 | … |
| | F555W | F555W−F850LP | 0.468 ± 0.015 | −0.005 ± 0.017 | 0.000 ± 0.000 | 0.472 ± 0.001 | 0.001 ± 0.001 | 0.000 ± 0.000 | … |
| F606W ..... | F606W | F435W−F606W | 0.487 ± 0.039 | 0.026 ± 0.026 | 0.000 ± 0.000 | 0.498 ± 0.002 | 0.011 ± 0.002 | 0.001 ± 0.000 | … |
| | F606W | F475W−F606W | 0.496 ± 0.028 | 0.036 ± 0.033 | 0.000 ± 0.000 | 0.500 ± 0.002 | 0.021 ± 0.004 | −0.000 ± 0.002 | … |
| | F606W | F555W−F606W | 0.445 ± 0.057 | 0.095 ± 0.066 | 0.000 ± 0.000 | 0.465 ± 0.007 | 0.070 ± 0.013 | −0.010 ± 0.006 | … |
| | F606W | F606W−F625W | 0.589 ± 0.074 | 0.129 ± 0.135 | 0.000 ± 0.000 | 0.569 ± 0.010 | 0.131 ± 0.038 | 0.056 ± 0.036 | … |
| | F606W | F606W−F775W | 0.548 ± 0.033 | 0.034 ± 0.037 | 0.000 ± 0.000 | 0.533 ± 0.001 | 0.017 ± 0.001 | −0.002 ± 0.001 | … |
| | F606W | F606W−F814W | 0.535 ± 0.021 | 0.033 ± 0.031 | 0.000 ± 0.000 | 0.525 ± 0.001 | 0.016 ± 0.001 | −0.002 ± 0.001 | … |
| | F606W | F606W−F850LP | 0.553 ± 0.030 | 0.021 ± 0.021 | 0.000 ± 0.000 | 0.534 ± 0.001 | 0.011 ± 0.001 | −0.001 ± 0.000 | … |
| F625W ..... | F625W | F435W−F625W | 0.537 ± 0.015 | 0.012 ± 0.013 | 0.000 ± 0.000 | 0.536 ± 0.001 | 0.005 ± 0.001 | −0.000 ± 0.000 | … |
| | F625W | F475W−F625W | 0.546 ± 0.011 | 0.013 ± 0.020 | 0.000 ± 0.000 | 0.539 ± 0.001 | 0.006 ± 0.002 | 0.002 ± 0.001 | … |
| | F625W | F555W−F625W | 0.546 ± 0.018 | 0.016 ± 0.042 | 0.000 ± 0.000 | 0.537 ± 0.001 | 0.010 ± 0.004 | 0.004 ± 0.002 | … |
| | F625W | F606W−F625W | 0.588 ± 0.050 | 0.063 ± 0.084 | 0.000 ± 0.000 | 0.562 ± 0.009 | 0.052 ± 0.036 | 0.021 ± 0.034 | … |
| | F625W | F625W−F775W | 0.553 ± 0.012 | 0.026 ± 0.030 | 0.000 ± 0.000 | 0.545 ± 0.001 | 0.012 ± 0.002 | −0.001 ± 0.001 | … |
| | F625W | F625W−F814W | 0.546 ± 0.010 | 0.024 ± 0.025 | 0.000 ± 0.000 | 0.540 ± 0.001 | 0.011 ± 0.002 | −0.001 ± 0.001 | … |
| | F625W | F625W−F850LP | 0.559 ± 0.017 | 0.014 ± 0.019 | 0.000 ± 0.000 | 0.547 ± 0.001 | 0.007 ± 0.001 | −0.000 ± 0.000 | … |
| F775W ..... | F775W | F435W−F775W | 0.706 ± 0.015 | 0.005 ± 0.014 | 0.000 ± 0.000 | 0.707 ± 0.001 | 0.003 ± 0.001 | 0.001 ± 0.000 | … |
| | F775W | F475W−F775W | 0.710 ± 0.007 | 0.007 ± 0.010 | 0.000 ± 0.000 | 0.711 ± 0.001 | 0.006 ± 0.001 | 0.001 ± 0.000 | … |
| | F775W | F555W−F775W | 0.711 ± 0.012 | 0.007 ± 0.020 | 0.000 ± 0.000 | 0.711 ± 0.001 | 0.008 ± 0.001 | 0.001 ± 0.001 | … |
| | F775W | F606W−F775W | 0.718 ± 0.028 | 0.011 ± 0.031 | 0.000 ± 0.000 | 0.722 ± 0.001 | 0.015 ± 0.001 | 0.002 ± 0.001 | … |
| | F775W | F625W−F775W | 0.713 ± 0.010 | 0.007 ± 0.024 | 0.000 ± 0.000 | 0.716 ± 0.001 | 0.016 ± 0.002 | 0.000 ± 0.001 | … |
| | F775W | F775W−F814W | 0.665 ± 0.061 | 0.115 ± 0.164 | 0.000 ± 0.000 | 0.677 ± 0.007 | 0.106 ± 0.026 | −0.029 ± 0.022 | … |
| | F775W | F775W−F850LP | 0.716 ± 0.031 | 0.017 ± 0.063 | 0.000 ± 0.000 | 0.726 ± 0.001 | 0.029 ± 0.002 | 0.001 ± 0.004 | … |
| F814W ..... | F814W | F435W−F814W | 0.653 ± 0.025 | −0.001 ± 0.018 | 0.000 ± 0.000 | 0.653 ± 0.002 | −0.003 ± 0.001 | −0.001 ± 0.000 | … |
| | F814W | F475W−F814W | 0.652 ± 0.014 | −0.003 ± 0.015 | 0.000 ± 0.000 | 0.651 ± 0.001 | −0.005 ± 0.002 | −0.001 ± 0.001 | … |
| | F814W | F555W−F814W | 0.654 ± 0.014 | −0.008 ± 0.017 | 0.000 ± 0.000 | 0.651 ± 0.001 | −0.007 ± 0.002 | −0.002 ± 0.001 | … |
| | F814W | F606W−F814W | 0.646 ± 0.023 | −0.010 ± 0.032 | 0.000 ± 0.000 | 0.643 ± 0.002 | −0.013 ± 0.002 | −0.002 ± 0.002 | … |
| | F814W | F625W−F814W | 0.649 ± 0.012 | −0.010 ± 0.025 | 0.000 ± 0.000 | 0.649 ± 0.001 | −0.014 ± 0.004 | −0.002 ± 0.002 | … |
| | F814W | F775W−F814W | 0.699 ± 0.044 | −0.132 ± 0.112 | 0.000 ± 0.000 | 0.674 ± 0.017 | −0.054 ± 0.078 | −0.047 ± 0.085 | … |
| | F814W | F814W−F850LP | 0.633 ± 0.057 | −0.026 ± 0.070 | 0.000 ± 0.000 | 0.578 ± 0.016 | −0.119 ± 0.042 | −0.044 ± 0.027 | … |

TABLE 12 (*Continued*)

| Source | Target | | Observed | | | Synthetic | | | |
|---|---|---|---|---|---|---|---|---|---|
| SMAG | TMAG | TCOL | c0 | c1 | c2 | c0 | c1 | c2 | TCOL Range[a] |
| F850LP ..... | F850LP | F435W−F850LP | 0.472 ± 0.010 | −0.009 ± 0.010 | 0.000 ± 0.000 | 0.469 ± 0.045 | −0.005 ± 0.060 | 0.003 ± 0.019 | <−0.9 |
| | | | | | | 0.474 ± 0.002 | −0.003 ± 0.002 | −0.001 ± 0.000 | >−0.9 |
| | F850LP | F475W−F850LP | 0.465 ± 0.011 | −0.011 ± 0.010 | 0.000 ± 0.000 | 0.378 ± 0.251 | −0.084 ± 0.245 | −0.015 ± 0.059 | <−1.7 |
| | | | | | | 0.470 ± 0.002 | −0.007 ± 0.001 | −0.002 ± 0.001 | >−1.7 |
| | F850LP | F555W−F850LP | 0.465 ± 0.011 | −0.014 ± 0.012 | 0.000 ± 0.000 | 0.459 ± 0.187 | −0.010 ± 0.238 | 0.004 ± 0.075 | <−1.2 |
| | | | | | | 0.469 ± 0.002 | −0.009 ± 0.002 | −0.002 ± 0.001 | >−1.2 |
| | F850LP | F606W−F850LP | 0.446 ± 0.029 | −0.020 ± 0.021 | 0.000 ± 0.000 | 0.448 ± 0.307 | −0.007 ± 0.287 | 0.004 ± 0.066 | <−1.8 |
| | | | | | | 0.456 ± 0.002 | −0.014 ± 0.002 | −0.002 ± 0.002 | >−1.8 |
| | F850LP | F625W−F850LP | 0.455 ± 0.015 | −0.023 ± 0.017 | 0.000 ± 0.000 | 0.433 ± 0.271 | −0.037 ± 0.374 | −0.001 ± 0.128 | <−1.2 |
| | | | | | | 0.461 ± 0.002 | −0.014 ± 0.002 | −0.001 ± 0.002 | >−1.2 |
| | F850LP | F775W−F850LP | 0.442 ± 0.030 | −0.060 ± 0.060 | 0.000 ± 0.000 | 0.333 ± 0.295 | −0.332 ± 0.778 | −0.172 ± 0.508 | <−0.6 |
| | | | | | | 0.451 ± 0.003 | −0.049 ± 0.009 | −0.015 ± 0.018 | >−0.6 |
| | F850LP | F814W−F850LP | 0.400 ± 0.072 | −0.088 ± 0.086 | 0.000 ± 0.000 | 0.531 ± 2.168 | 0.149 ± 4.034 | 0.102 ± 1.874 | <−1.0 |
| | | | | | | 0.390 ± 0.020 | −0.141 ± 0.058 | −0.052 ± 0.041 | >−1.0 |

[a] TCOL range applies only to synthetic transformations.

strumental system to the standard system for the low surface gravity stars in NGC 2419.

For the synthetic *UBVRI* photometry, we first used the Landolt *UBVRI* filter set (i.e., Johnson *UBV*+Cousins *RI*) defined in SYNPHOT. In particular, the throughput data for the Johnson *UBV* bands are the U3, B2, and *V* synthetic bandpass data of Buser & Kurucz (1978), while the Cousins *R* and *I* throughputs are taken from Bessel (1983). However, we got poor agreement with the observed transformation using the B2 filter. We then tried using other *B* synthetic bandpasses and found a much better agreement when applying the *B* filter from the Harris set in use at KPNO and WIYN.[22]

For both ACS cameras, we compared the observed transformations using the two NGC 2419 control data sets with the corresponding synthetic transformations. We obtained poor agreement with the *I* bands of Stetson's data set, with systematic offsets of the order of a few percent between the two curves. The observed *R*-band transformation also shows some departures for the reddest stars. Finally, the *V* band shows a good match between observed and synthetic transformations. Using Saha's data set, we have significantly better results in *V*, *R*, and *I* available bands. The *B* band shows a similar agreement using either Stetson's or Saha's data set. The observed and synthetic transformation provide similar results for stars with $B - V > 0.5$, whereas for bluer stars the discrepancy between the two transformations can be as high as 5%. Given the possible uncertainties in the shape of the blue side of the total response curve with the F435W filter, our bluest filter with WFC, we suggest using the observed transformations when this filter is involved.

We decided to use only the Saha photometric data set of NGC 2419 to calculate the coefficients for the observational transformations. However, in determining the new zero points for WFPC2, Heyer et al. (2002) find that Stetson's photometry produces values slightly closer to the historical zero points of WFPC2 than Saha's photometry. Unfortunately, no color term was taken into account.

We list the observational and synthetic transformation coefficients to use in equation (12) for different combinations of most filters in Appendix D.2, Tables 22 and 23, for WFC-to-*BVRI* and HRC-to-*UBVRI*, respectively. The transformations between primary filters are shown in Appendix D.2, Figures 21 and 22. An example of how to calculate the transformation is provided in Appendix D.1.

As expected, Figures 21 and 22 show large scatter in the synthetic transformation. The BPGS atlas includes stars with a wide range of surface gravity and possibly metallicity. We used the synthetic system to investigate dependencies of the main transformations on gravity and metallicity. For the gravity, we use the Bruzual Spectrum Synthesis Atlas (BZ77)[23] implemented in SYNPHOT. It provides solar-metallicity spectra for main-sequence stars (from spectral class O5 to M6), giant stars (from O8 to M6), and supergiants (from O9 to M1). For the metallicity dependence, we use the model atmosphere of Kurucz (1993). We selected models to cover the main sequence from O3 to M2 for the solar metallicity, and for [Fe/H] = +0.5, −1.0, and −2.0. The results are shown in Appendix D.2, Figures 23 and 24, for the WFC and HRC, respectively. In both figures the column on the left shows the dependence on the surface gravity; filled circles represent data for a synthetic main sequence. The sequences of giant and supergiant stars are represented by gray stars and squares, respectively. The column on the right shows the dependence on the metallicity for main-sequence stars: black dots show the solar metallicity, filled triangles are [Fe/H] = 0.5, gray filled stars are [Fe/H] = −1, and squares are [Fe/H] = −2.

[22] The curves used for the synthetic *UBVRI* are available at http://acs.pha.jhu.edu/instrument/photometry.

[23] The Bruzual Spectrum Synthesis Atlas is available at http://www.stsci.edu/HST/observatory/cdbs/astronomical_catalogs.html.

TABLE 13
COEFFICIENTS FOR THE TRANSFORMATION FROM HRC TO WFC

| SOURCE | TARGET | | OBSERVED | | | SYNTHETIC | | | |
|---|---|---|---|---|---|---|---|---|---|
| SMAG | TMAG | TCOL | c0 | c1 | c2 | c0 | c1 | c2 | TCOL Range[a] |
| F435W ..... | F435W | F435W−F475W | −0.573 ± 0.073 | −0.045 ± 0.111 | 0.000 ± 0.000 | −0.513 ± 0.031 | −0.378 ± 0.178 | 0.439 ± 0.244 | <0.5 |
| | | | | | | −0.592 ± 0.008 | −0.006 ± 0.017 | 0.015 ± 0.008 | >0.5 |
| | F435W | F435W−F550M | | | | −0.550 ± 0.369 | 0.100 ± 0.629 | 0.060 ± 0.267 | <−1.0 |
| | | | | | | −0.588 ± 0.001 | 0.008 ± 0.001 | 0.002 ± 0.002 | >−1.0 |
| | F435W | F435W−F555W | −0.592 ± 0.022 | −0.016 ± 0.036 | 0.000 ± 0.000 | −0.594 ± 0.002 | −0.010 ± 0.009 | 0.089 ± 0.040 | <0.3 |
| | | | | | | −0.590 ± 0.004 | −0.002 ± 0.007 | 0.006 ± 0.003 | >0.3 |
| | F435W | F435W−F606W | −0.580 ± 0.041 | −0.014 ± 0.028 | 0.000 ± 0.000 | −0.563 ± 0.008 | −0.076 ± 0.024 | 0.047 ± 0.017 | <1.2 |
| | | | | | | −0.586 ± 0.009 | −0.007 ± 0.008 | 0.004 ± 0.002 | >1.2 |
| | F435W | F435W−F625W | −0.591 ± 0.025 | −0.009 ± 0.023 | 0.000 ± 0.000 | −0.594 ± 0.002 | −0.010 ± 0.007 | 0.040 ± 0.021 | <0.4 |
| | | | | | | −0.591 ± 0.004 | −0.000 ± 0.004 | 0.002 ± 0.001 | >0.4 |
| | F435W | F435W−F775W | −0.586 ± 0.023 | −0.011 ± 0.021 | 0.000 ± 0.000 | −0.593 ± 0.002 | 0.009 ± 0.009 | 0.019 ± 0.008 | <0.3 |
| | | | | | | −0.596 ± 0.003 | 0.009 ± 0.002 | −0.002 ± 0.000 | >0.3 |
| | F435W | F435W−F814W | −0.592 ± 0.023 | −0.006 ± 0.018 | 0.000 ± 0.000 | −0.594 ± 0.002 | 0.000 ± 0.007 | 0.019 ± 0.009 | <0.4 |
| | | | | | | −0.597 ± 0.003 | 0.008 ± 0.002 | −0.001 ± 0.000 | >0.4 |
| | F435W | F435W−F850LP | −0.599 ± 0.009 | −0.004 ± 0.010 | 0.000 ± 0.000 | −0.579 ± 0.011 | 0.028 ± 0.017 | 0.013 ± 0.006 | <−0.5 |
| | | | | | | −0.590 ± 0.001 | 0.006 ± 0.001 | −0.001 ± 0.000 | >−0.5 |
| F475W ..... | F475W | F435W−F475W | −0.520 ± 0.050 | −0.005 ± 0.074 | 0.000 ± 0.000 | −0.577 ± 0.004 | 0.093 ± 0.009 | −0.020 ± 0.006 | … |
| | F475W | F475W−F550M | | | | −0.488 ± 0.002 | 0.040 ± 0.006 | −0.003 ± 0.004 | … |
| | F475W | F475W−F555W | −0.517 ± 0.012 | 0.033 ± 0.045 | 0.000 ± 0.000 | −0.518 ± 0.001 | 0.059 ± 0.003 | −0.004 ± 0.007 | … |
| | F475W | F475W−F606W | −0.539 ± 0.023 | 0.021 ± 0.028 | 0.000 ± 0.000 | −0.557 ± 0.002 | 0.052 ± 0.003 | −0.011 ± 0.002 | … |
| | F475W | F475W−F625W | −0.526 ± 0.012 | 0.020 ± 0.023 | 0.000 ± 0.000 | −0.532 ± 0.001 | 0.029 ± 0.002 | −0.002 ± 0.001 | … |
| | F475W | F475W−F775W | −0.525 ± 0.010 | 0.011 ± 0.013 | 0.000 ± 0.000 | −0.529 ± 0.006 | 0.019 ± 0.016 | 0.001 ± 0.010 | <−0.1 |
| | | | | | | −0.528 ± 0.002 | 0.025 ± 0.002 | −0.005 ± 0.001 | >−0.1 |
| | F475W | F475W−F814W | −0.528 ± 0.012 | 0.012 ± 0.014 | 0.000 ± 0.000 | −0.533 ± 0.010 | 0.020 ± 0.029 | 0.002 ± 0.019 | <−0.2 |
| | | | | | | −0.534 ± 0.002 | 0.025 ± 0.002 | −0.004 ± 0.000 | >−0.2 |
| | F475W | F475W−F850LP | −0.515 ± 0.010 | 0.011 ± 0.009 | 0.000 ± 0.000 | −0.513 ± 0.065 | 0.021 ± 0.066 | 0.002 ± 0.017 | <−1.4 |
| | | | | | | −0.514 ± 0.001 | 0.015 ± 0.001 | −0.003 ± 0.000 | >−1.4 |
| F555W ..... | F55W | F435W−F555W | −0.478 ± 0.021 | 0.006 ± 0.034 | 0.000 ± 0.000 | −0.470 ± 0.001 | −0.003 ± 0.002 | 0.000 ± 0.001 | … |
| | F555W | F475W−F555W | −0.469 ± 0.014 | 0.010 ± 0.054 | 0.000 ± 0.000 | −0.472 ± 0.001 | −0.006 ± 0.002 | −0.002 ± 0.004 | … |
| | F555M | F550M−F555W | | | | −0.483 ± 0.021 | 0.013 ± 0.059 | 0.002 ± 0.041 | … |
| | F555W | F555W−F606W | −0.506 ± 0.045 | 0.038 ± 0.049 | 0.000 ± 0.000 | −0.459 ± 0.006 | −0.019 ± 0.010 | 0.006 ± 0.004 | … |
| | F555W | F555W−F625W | −0.478 ± 0.019 | 0.015 ± 0.041 | 0.000 ± 0.000 | −0.470 ± 0.001 | −0.006 ± 0.004 | 0.002 ± 0.002 | … |
| | F555W | F555W−F775W | −0.473 ± 0.014 | 0.008 ± 0.023 | 0.000 ± 0.000 | −0.471 ± 0.001 | −0.003 ± 0.001 | 0.001 ± 0.000 | … |
| | F555W | F555W−F814W | −0.479 ± 0.017 | 0.012 ± 0.021 | 0.000 ± 0.000 | −0.470 ± 0.001 | −0.003 ± 0.001 | 0.000 ± 0.000 | … |
| | F555W | F555W−F850LP | −0.469 ± 0.014 | 0.008 ± 0.015 | 0.000 ± 0.000 | −0.473 ± 0.001 | −0.002 ± 0.001 | 0.000 ± 0.000 | … |
| F606W ..... | F606W | F435W−F606W | −0.482 ± 0.035 | −0.031 ± 0.024 | 0.000 ± 0.000 | −0.499 ± 0.002 | −0.011 ± 0.002 | −0.001 ± 0.000 | … |
| | F606W | F475W−F606W | −0.493 ± 0.033 | −0.040 ± 0.039 | 0.000 ± 0.000 | −0.502 ± 0.002 | −0.018 ± 0.003 | −0.001 ± 0.001 | … |
| | F606W | F555W−F606W | −0.447 ± 0.062 | −0.084 ± 0.069 | 0.000 ± 0.000 | −0.465 ± 0.007 | −0.067 ± 0.013 | 0.010 ± 0.006 | … |
| | F606W | F606W−F625W | −0.554 ± 0.071 | −0.062 ± 0.136 | 0.000 ± 0.000 | −0.570 ± 0.010 | −0.139 ± 0.040 | −0.064 ± 0.040 | … |
| | F606W | F606W−F775W | −0.543 ± 0.027 | −0.032 ± 0.036 | 0.000 ± 0.000 | −0.530 ± 0.001 | −0.018 ± 0.001 | 0.003 ± 0.001 | … |
| | F606W | F606W−F814W | −0.532 ± 0.016 | −0.026 ± 0.027 | 0.000 ± 0.000 | −0.523 ± 0.001 | −0.018 ± 0.001 | 0.002 ± 0.001 | … |
| | F606W | F606W−F850LP | −0.552 ± 0.031 | −0.021 ± 0.021 | 0.000 ± 0.000 | −0.535 ± 0.001 | −0.012 ± 0.001 | 0.001 ± 0.000 | … |
| F625W ..... | F625W | F435W−F625W | −0.543 ± 0.016 | −0.013 ± 0.015 | 0.000 ± 0.000 | −0.537 ± 0.001 | −0.005 ± 0.001 | 0.000 ± 0.000 | … |
| | F625W | F475W−F625W | −0.549 ± 0.012 | −0.011 ± 0.023 | 0.000 ± 0.000 | −0.539 ± 0.001 | −0.006 ± 0.002 | 0.000 ± 0.001 | … |
| | F625W | F555W−F625W | −0.544 ± 0.020 | −0.020 ± 0.041 | 0.000 ± 0.000 | −0.536 ± 0.001 | −0.010 ± 0.004 | −0.004 ± 0.002 | … |
| | F625W | F606W−F625W | −0.607 ± 0.043 | −0.113 ± 0.083 | 0.000 ± 0.000 | −0.563 ± 0.009 | −0.056 ± 0.038 | −0.024 ± 0.038 | … |
| | F625W | F625W−F775W | −0.549 ± 0.010 | −0.017 ± 0.030 | 0.000 ± 0.000 | −0.543 ± 0.001 | −0.013 ± 0.002 | 0.001 ± 0.001 | … |
| | F625W | F625W−F814W | −0.547 ± 0.012 | −0.018 ± 0.027 | 0.000 ± 0.000 | −0.539 ± 0.001 | −0.011 ± 0.002 | 0.001 ± 0.001 | … |
| | F625W | F625W−F850LP | −0.567 ± 0.018 | −0.017 ± 0.019 | 0.000 ± 0.000 | −0.548 ± 0.001 | −0.008 ± 0.001 | 0.000 ± 0.000 | … |
| F775W ..... | F775W | F435W−F775W | −0.708 ± 0.011 | −0.005 ± 0.010 | 0.000 ± 0.000 | −0.707 ± 0.001 | −0.003 ± 0.001 | −0.001 ± 0.000 | … |
| | F775W | F475W−F775W | −0.710 ± 0.010 | −0.005 ± 0.013 | 0.000 ± 0.000 | −0.710 ± 0.001 | −0.005 ± 0.001 | −0.001 ± 0.000 | … |
| | F775W | F555W−F775W | −0.709 ± 0.010 | −0.008 ± 0.014 | 0.000 ± 0.000 | −0.709 ± 0.001 | −0.008 ± 0.001 | −0.001 ± 0.001 | … |
| | F775W | F606W−F775W | −0.715 ± 0.017 | −0.012 ± 0.024 | 0.000 ± 0.000 | −0.719 ± 0.001 | −0.014 ± 0.001 | −0.002 ± 0.001 | … |
| | F775W | F625W−F775W | −0.710 ± 0.014 | −0.016 ± 0.040 | 0.000 ± 0.000 | −0.713 ± 0.001 | −0.016 ± 0.002 | −0.000 ± 0.001 | … |
| | F775W | F775W−F814W | −0.732 ± 0.053 | 0.066 ± 0.162 | 0.000 ± 0.000 | −0.677 ± 0.007 | −0.128 ± 0.032 | 0.041 ± 0.033 | … |
| | F775W | F775W−F850LP | −0.726 ± 0.035 | −0.019 ± 0.048 | 0.000 ± 0.000 | −0.734 ± 0.002 | −0.032 ± 0.004 | −0.002 ± 0.004 | … |
| F814W ..... | F814W | F435W−F814W | −0.650 ± 0.026 | 0.002 ± 0.020 | 0.000 ± 0.000 | −0.650 ± 0.005 | 0.007 ± 0.024 | −0.002 ± 0.025 | <0.1 |
| | | | | | | −0.650 ± 0.004 | −0.001 ± 0.003 | 0.002 ± 0.000 | >0.1 |
| | F814W | F475W−F814W | −0.653 ± 0.015 | 0.005 ± 0.017 | 0.000 ± 0.000 | −0.638 ± 0.079 | 0.025 ± 0.179 | 0.006 ± 0.098 | <−0.6 |
| | | | | | | −0.650 ± 0.002 | 0.002 ± 0.003 | 0.002 ± 0.001 | >−0.6 |
| | F814W | F555W−F814W | −0.649 ± 0.020 | 0.002 ± 0.024 | 0.000 ± 0.000 | −0.655 ± 0.059 | −0.012 ± 0.290 | −0.031 ± 0.338 | <−0.2 |
| | | | | | | −0.651 ± 0.002 | 0.003 ± 0.004 | 0.003 ± 0.001 | >−0.2 |
| | F814W | F606W−F814W | −0.646 ± 0.016 | 0.004 ± 0.027 | 0.000 ± 0.000 | −0.655 ± 0.191 | −0.020 ± 0.389 | −0.020 ± 0.195 | <−0.8 |
| | | | | | | −0.645 ± 0.002 | 0.012 ± 0.003 | 0.004 ± 0.003 | >−0.8 |

TABLE 13 (*Continued*)

| Source | Target | | Observed | | | Synthetic | | | |
|---|---|---|---|---|---|---|---|---|---|
| SMAG | TMAG | TCOL | c0 | c1 | c2 | c0 | c1 | c2 | TCOL Range[a] |
| | F814W | F625W−F814W | −0.653 ± 0.017 | 0.010 ± 0.037 | 0.000 ± 0.000 | −0.647 ± 0.018 | 0.020 ± 0.144 | −0.014 ± 0.255 | <−0.1 |
| | | | | | | −0.650 ± 0.002 | 0.014 ± 0.008 | 0.002 ± 0.004 | >−0.1 |
| | F814W | F775W−F814W | | | | −0.702 ± 0.377 | 0.248 ± 3.172 | −0.212 ± 6.634 | <0.2 |
| | | | | | | −0.666 ± 0.032 | 0.023 ± 0.164 | 0.121 ± 0.200 | >0.2 |
| | F814W | F814W−F850LP | −0.614 ± 0.062 | 0.035 ± 0.060 | 0.000 ± 0.000 | −0.897 ± 3.138 | −0.425 ± 5.047 | −0.186 ± 2.028 | <−1.1 |
| | | | | | | −0.539 ± 0.032 | 0.175 ± 0.073 | 0.067 ± 0.041 | >−1.1 |
| F850LP ..... | F850LP | F435W−F850LP | −0.471 ± 0.012 | 0.008 ± 0.012 | 0.000 ± 0.000 | −0.465 ± 0.083 | 0.007 ± 0.097 | −0.002 ± 0.028 | <−1.2 |
| | | | | | | −0.474 ± 0.002 | 0.003 ± 0.002 | 0.001 ± 0.000 | >−1.2 |
| | F850LP | F475W−F850LP | −0.464 ± 0.017 | 0.010 ± 0.016 | 0.000 ± 0.000 | −0.450 ± 0.097 | 0.015 ± 0.100 | −0.001 ± 0.025 | <−1.4 |
| | | | | | | −0.470 ± 0.002 | 0.007 ± 0.002 | 0.002 ± 0.001 | >−1.4 |
| | F850LP | F555W−F850LP | −0.463 ± 0.015 | 0.012 ± 0.016 | 0.000 ± 0.000 | −0.375 ± 0.258 | 0.112 ± 0.325 | 0.026 ± 0.101 | <−1.3 |
| | | | | | | −0.469 ± 0.002 | 0.009 ± 0.002 | 0.001 ± 0.001 | >−1.3 |
| | F850LP | F606W−F850LP | −0.447 ± 0.028 | 0.015 ± 0.019 | 0.000 ± 0.000 | −0.425 ± 0.475 | 0.026 ± 0.431 | −0.001 ± 0.097 | <−1.9 |
| | | | | | | −0.455 ± 0.002 | 0.015 ± 0.002 | 0.002 ± 0.002 | >−1.9 |
| | F850LP | F625W−F850LP | −0.448 ± 0.019 | 0.021 ± 0.019 | 0.000 ± 0.000 | −0.388 ± 0.371 | 0.091 ± 0.490 | 0.018 ± 0.161 | <−1.3 |
| | | | | | | −0.460 ± 0.002 | 0.015 ± 0.002 | 0.001 ± 0.002 | >−1.3 |
| | F850LP | F775W−F850LP | −0.451 ± 0.058 | 0.027 ± 0.079 | 0.000 ± 0.000 | −0.229 ± 0.752 | 0.449 ± 1.511 | 0.190 ± 0.757 | <−0.9 |
| | | | | | | −0.435 ± 0.005 | 0.064 ± 0.019 | 0.018 ± 0.020 | >−0.9 |
| | F850LP | F814W−F850LP | −0.407 ± 0.117 | 0.062 ± 0.115 | 0.000 ± 0.000 | −0.605 ± 3.138 | −0.259 ± 5.047 | −0.132 ± 2.028 | <−1.1 |
| | | | | | | −0.362 ± 0.032 | 0.161 ± 0.073 | 0.053 ± 0.041 | >−1.1 |

[a] TCOL range applies only to synthetic transformations.

These figures show that the dependency of the transformations on these quantities can be quite large. Gravity provides a large spread in short and long-wavelength filters for stars around zero color and for low-temperature stars. Metallicity causes more spread for redder stars. Significant departures from the relation derived from stellar spectra are expected for the transformation of nonstellar objects, especially for galaxies at high redshift.

The derived transformations from the ACS systems to *UBVRI* can be applied to main-sequence and giant stars without introducing errors of more than a few percent. However, it should not be expected that the 1%–2% accuracy of ACS photometry will be preserved in the transformed data. Transformation to *U*, *B*, and *I* filters are highly dependent on the object spectral details, and Tables 22 and 23 should be used with extreme caution for objects different from those used to derive the relations. Therefore, whenever possible, we strongly recommend working with the ACS system.

### 8.4. Transformations from ACS to WFPC2

Most ACS broadband filters have, at least nominally, a close match in the vast WFPC2 filter complement. However, the different response of the two instruments and specific filter designs create significant differences between the ACS and WFPC2, as shown in Figure 13.

Since the installation of WFPC2 on *HST* a decade ago, a large amount of WFPC2 data has become publicly available through the *HST* archives for calibration purposes. Now many characteristics of the instrument are well understood, although refinements are still in progress (Baggett et al. 2001; Casertano & Wiggs 2001; Whitmore & Heyer 2002; Dolphin 2000a).

In order to derive transformations between ACS and WFPC2, we retrieved WFPC2 observations of NGC 104 (programs 7465, 6114, 6660, and 6114) and NGC 2419 (programs 7268, 7630, and 9601) from the STScI archive. Accurate stellar photometry on WFPC2 images requires a careful treatment of the undersampling effect, of position-dependent pixel size variations, and of the charge transfer efficiency (CTE) degradation. We found that HSTPHOT,[24] an automatic stellar photometry software specifically designed for WFPC2 data (Dolphin 2000b), accounts for all these issues with acceptable accuracy. The dependability of the package was tested by first performing PSF-fitting photometry with IRAF DAOPHOT on a subsample of the data, applying aperture corrections measured from isolated stars in the same images, and CTE correction from Dolphin (2000a), and comparing the results with HSTPHOT results. Since the results from these two methods did not show any systematic difference, we decided to use HSTPHOT to automatically process all the WFPC2 observations.

We used the `multiphot` photometry feature of HSTPHOT instead of performing photometry on combined images. This method, although reducing the detectability of faint stars, increased the photometric accuracy for the bright stars that we used to estimate the transformation coefficients. Finally, the HSTPHOT output flight system magnitudes were converted into OBMAGs by subtracting flight-system zero points (Dolphin 2000b). Figure 25 in Appendix D.3 shows the observed CMD for the two clusters.

There is a subtlety involved in the determination of OBMAG in the WFPC2 photometric system, because WFPC2 zero points are slightly different depending on the chip. We choose the

[24] A detailed description and usage of HSTPHOT can be found at http://www.noao.edu/staff/dolphin/HSTphot.

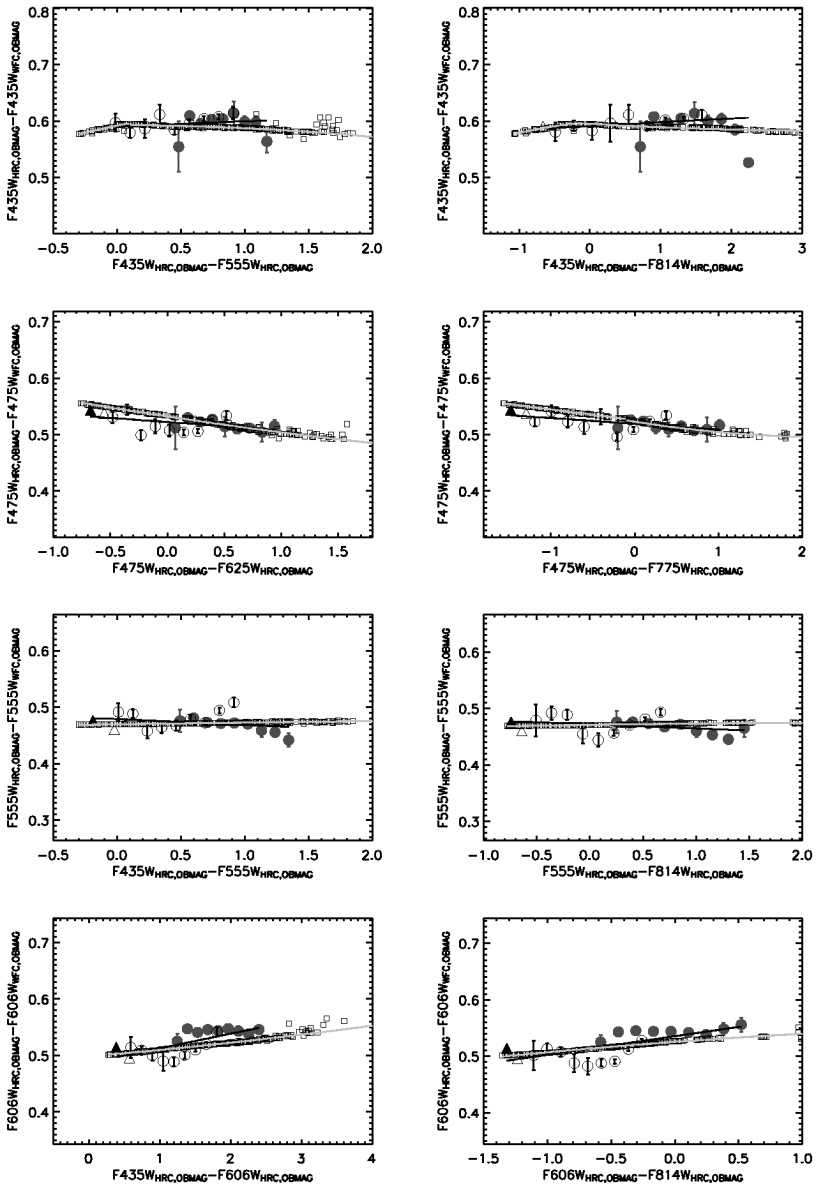


FIG. 15.—Observed and synthetic WFC-to-HRC transformations for primary photometric filters. Squares show the synthetic measurements for the BPGS atlas. The circles represent observational data (filled for NGC 104, open for NGC 2419). The two standard stars are shown with triangles. The black line shows the linear fit to the observational points; the light gray curve shows the synthetic transformations. [*See the electronic edition of the PASP for a color version of this figure*.]

WF3 chip as a basis for our OBMAG definition. For the synthetic transformation, we used the sensitivity curves for all WFPC2/WF3 components currently available in SYNPHOT (Bagget et al. 1997).

We list the observational and synthetic transformation coefficients to use in equation (12) for different combinations of most filters in Appendix D.2, Tables 24 and 25 for WFC-to-WFPC2 and HRC-to-WFPC2 conversions, respectively. The appropriate WFPC2/WF3 zero points for *gain* = 15 must be added when transforming the WFPC2 OBMAG into any WFPC2 photometric system. The transformations between primary filters are shown in Appendix D.3, Figures 26 and 27.

## 9. The HRC UV RED LEAK

We investigated the red leak of the UV filters of the HRC. When designing a UV filter, the high suppression of the red off-band transmission goes at the expense of the in-band

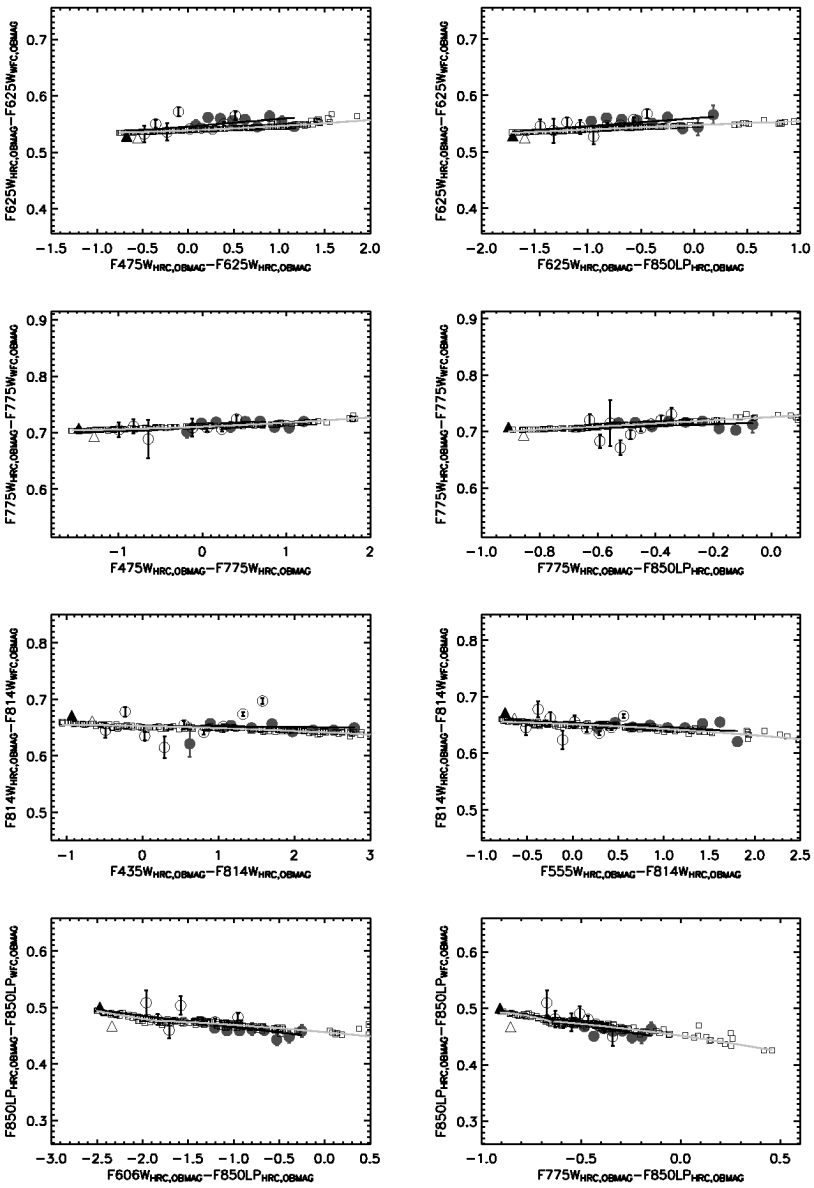


FIG. 15.—*Continued*

throughput. The elevated quantum efficiency of the HRC makes it possible to design UV filters with limited red leak. We defined all contributions from $\lambda > 4000$ Å as red leak. In order to quantify the red-leak contribution as a function of the stellar color, we used the BPGS library of stellar spectra and the HRC throughput curves. Figure 16 shows the amount of light contributed by red leak as a function of color for the three filters. Clearly, there is no red leak in F330W, but it becomes important in F250W and particularly in F220W. Accurate UV photometry in the F250W and F220W filters will require red-leak corrections for objects with a spectrum as red as that of an F5 V star or colder, and will be essentially impossible for objects with a spectrum later than M. In addition to the majority of the flux being off-band, the red photons will contribute to create an extended halo (see § 4.3) that will be superimposed on the sharper UV PSF.

## 10. REDDENING IN THE ACS SYSTEM

The ACS filters can differ significantly from the Johnson-Cousins *UBVRI* bandpasses (see § 8.3), and these differences need to be taken into account when calculating reddening corrections. ACS magnitudes should be corrected with extinction coefficients calculated in the native photometric system. For

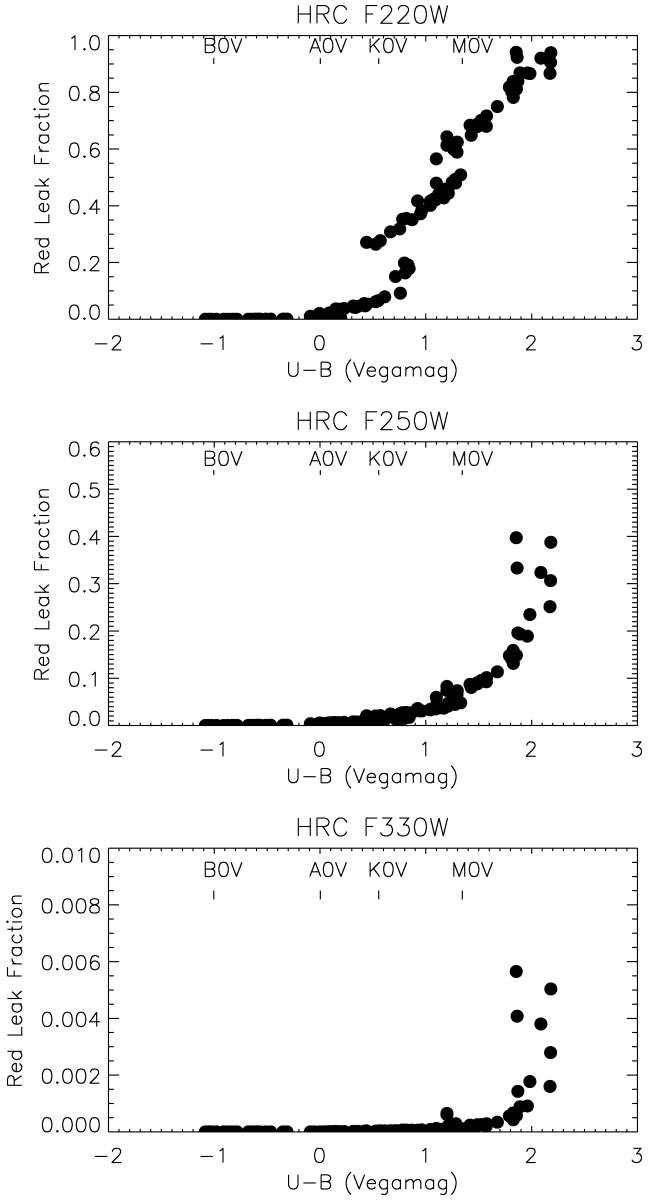


FIG. 16.—Amount of light contributed by red leak (λ > 4000 Å) as a function of color.

the same reason, any reddening correction should be applied before transforming to any other photometric system. We calculated a grid of extinction coefficients for all ACS filters as a function of $E(B-V)$ up to $E(B-V) = 5.5$. The extinction was computed using the synthetic throughput curves in SYNPHOT and adopting the Galactic extinction law presented by Cardelli et al. (1989). For medium- and broadband filters, the extinction depends on the object's color. We therefore selected three template stars (O5 V, G2 V, and M0 V) from the BPGS atlas and three galaxy templates (E, Sc, and Im) from Benítez et al. (2004), and computed the extinction coefficient for the

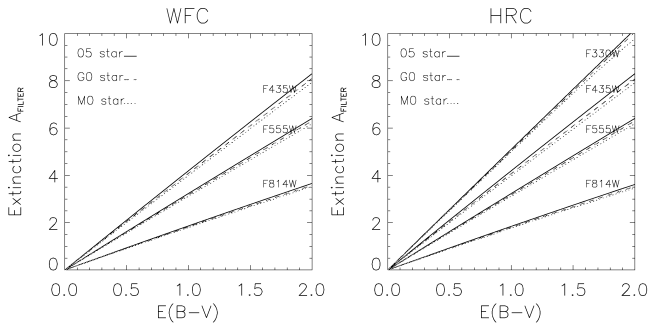


FIG. 17.—Extinction in ACS WFC and HRC filters as a function of $E(B-V)$ for three stars of different spectral type. We used the interstellar extinction curve from Cardelli et al. (1989), with $R_v = 3.1$.

grid of $E(B-V)$ values. Figure 17 shows the extinction in a few primary ACS filters as a function of $E(B-V)$ computed for three stars of different types. Tables 14 and 15 list the extinction $A(P)$ normalized to the photometric measurement of $E(B-V) = A(V)/3.1$ for all ACS filters using the interstellar extinction of Cardelli et al. (1989). Due to the difference in the filter transmission curves between the ground-based system and the ACS systems, there could be systematic differences in the extinction coefficients for the two systems. Figure 18 shows that the extinction in F330W, F435W, and F555W is systematically higher than in $U$, $B$, and $V$ because the effective wavelength in these ACS band is shorter than in the corresponding Johnson filters. On the other hand, the extinction in F814W is systematically lower than in the $I$ band, because the effective wavelength in the F814W is longer than in $I$.

## 11. CONCLUSIONS

We have presented the current status and the photometric calibration of the two CCD channels of ACS. The overall performance is as expected from prelaunch testing of the instrument. A positive surprise was the discovery that the ground throughput prediction underestimated the overall sensitivity of the camera by a few percent in the red, up to ~20% in the blue for WFC and in the visual and the near-IR for HRC. HRC also showed an unpredicted dip in the UV response at ~3200 Å.

Initial signs of degradation due to the *HST* radiative environment are already visible in terms of dark rate increase, charge transfer efficiency degradation, and growth of the permanent hot pixel population. The detailed effect of CTE losses as a function of brightness and background level is being determined with a continuous effort at STScI. The correction formula to be applied to photometric measurements is constantly kept up to date on the ACS Web server at STScI.

The long-wavelength light scattering in ACS CCDs has a twofold effect: the width of the PSF increases significantly in the near-IR filters, and the aperture correction in the near-IR

TABLE 14
EXTINCTION RATIOS $A(P)/E(B-V)$ IN WFC FILTERS FOR DIFFERENT SEDS

| SED | F435W | F475W | F502N | F550M | F555W | F606W | F625W | F658N | F660N | F775W | F814W | F850LP | F892N |
|---|---|---|---|---|---|---|---|---|---|---|---|---|---|
| O5 ..... | 4.192 | 3.773 | 3.459 | 3.052 | 3.233 | 2.936 | 2.673 | 2.525 | 2.518 | 2.005 | 1.864 | 1.498 | 1.509 |
| G2 ..... | 4.081 | 3.634 | 3.458 | 3.042 | 3.177 | 2.809 | 2.637 | 2.525 | 2.517 | 1.982 | 1.825 | 1.485 | 1.508 |
| M0 ..... | 3.994 | 3.555 | 3.458 | 3.030 | 3.115 | 2.716 | 2.616 | 2.525 | 2.517 | 1.965 | 1.796 | 1.471 | 1.508 |
| E ..... | 4.044 | 3.591 | 3.458 | 3.040 | 3.158 | 2.764 | 2.623 | 2.525 | 2.517 | 1.973 | 1.803 | 1.472 | 1.508 |
| Sc ..... | 4.103 | 3.637 | 3.459 | 3.041 | 3.176 | 2.799 | 2.633 | 2.525 | 2.517 | 1.981 | 1.822 | 1.477 | 1.508 |
| Im ..... | 4.127 | 3.659 | 3.460 | 3.044 | 3.200 | 2.830 | 2.637 | 2.525 | 2.517 | 1.979 | 1.818 | 1.476 | 1.508 |

depends on the SED of the object. Recipes for calculating the aperture correction have been presented.

Photometric calibration data of spectrophotometric standard stars have been obtained for all ACS filters to provide transformation to physical fluxes. The HRC and the WFC synthetic photometric systems have been constructed and reproduce count rates of spectrophotometric standards to within 0.5% in all broadband filters. Zero points are provided in three different magnitude systems.

Transformations between HRC and WFC photometric systems are given. Although ground observation and synthetic photometry have been used for the determination of the transformation to *UBVRI* and WFPC2 photometric systems, we strongly recommend that ACS photometric results be referred to a system based on its own filters. Synthetic photometry can be used to construct isochrones and to safely convert models into the ACS observational plane. In some instances, a direct comparison with previous results in a different photometric system may still be needed. We warn the reader that transformations to *UBVRI* and WFPC2 depend on details of the stellar spectra and should be used with caution. Generally, transformed data will be accurate within a few percent, but differences could be significantly larger for peculiar spectra. We also provide tables for the color transformation for a few galaxy templates as a function of the redshift.

The effective wavelength of the ACS filters can differ significantly from their counterparts in the WFPC2 and *UBVRI* systems. As a consequence, accurate reddening corrections must be made in the ACS system before transforming the magnitude to other photometric systems. Extinction curves for the ACS filters for a standard interstellar reddening law have been presented for a sample of stellar and galaxy templates. Extinction for other reddening laws can be derived using the synthetic ACS system.

The process of understanding and calibrating ACS is ongoing. More calibration programs are currently planned, and more data are being analyzed. ACS users are encouraged to stay posted for future reports from the STScI and to contact the ACS Instrument Scientists with questions (help@stsci.edu).

Many people have contributed to this work. ACS was engineered, built, and tested by a dedicated team at Ball Aerospace, Boulder, CO. We thank the entire ACS Investigation Definition Team and all personnel at GSFC who have supported ground calibration and prelaunch testing. Special thanks to the entire crew of STS-109, who did a superb job during an extraordinarily demanding servicing mission.

Thanks to ACS personnel at STScI, the ACS photometric calibration group, and the ACS science team. They have prepared many of the calibration proposals and were always available to discuss results. Among these people, we specially appreciate the comments and work we received from Ralph Bohlin, Francesca Boffi, Nick Cross, David Golimowski, Inge Heyer, John Krist, Adam Riess, and Roeland van der Marel.

We are indebted to Abhiji Saha for providing unpublished magnitudes and data relating to the *UBVRI* system. We also thank Tom Brown, Stefano Casertano, Leo Girardi, Brad Whitmore, and Manuela Zoccali for their useful suggestions and insightful discussion.

The entire paper has been modelled after equivalent WFPC2

TABLE 15
EXTINCTION RATIOS $A(P)/E(B-V)$ IN HRC FILTERS FOR DIFFERENT SEDS

| SED | F220W | F250W | F330W | F344N | F435W | F475W | F502N | F550M | F555W | F606W | F625W | F658N | F660N | F775W | F814W | F850LP | F892N |
|---|---|---|---|---|---|---|---|---|---|---|---|---|---|---|---|---|---|
| O5 ..... | 8.350 | 6.353 | 5.105 | 4.991 | 4.197 | 3.741 | 3.461 | 3.053 | 3.235 | 2.953 | 2.681 | 2.528 | 2.546 | 2.018 | 1.847 | 1.473 | 1.513 |
| G2 ..... | 5.735 | 5.676 | 5.046 | 4.987 | 4.075 | 3.608 | 3.458 | 3.043 | 3.180 | 2.825 | 2.644 | 2.525 | 2.518 | 1.995 | 1.803 | 1.460 | 1.508 |
| M0 ..... | 2.809 | 4.965 | 5.000 | 4.953 | 3.984 | 3.535 | 3.458 | 3.031 | 3.118 | 2.730 | 2.623 | 2.525 | 2.517 | 1.978 | 1.770 | 1.447 | 1.507 |
| E ..... | 5.479 | 5.654 | 5.043 | 4.980 | 4.036 | 3.569 | 3.458 | 3.041 | 3.160 | 2.780 | 2.630 | 2.525 | 2.518 | 1.985 | 1.779 | 1.447 | 1.508 |
| Sc ..... | 7.773 | 6.133 | 5.066 | 4.987 | 4.100 | 3.611 | 3.459 | 3.042 | 3.179 | 2.816 | 2.640 | 2.525 | 2.518 | 1.994 | 1.800 | 1.452 | 1.508 |
| Im ..... | 7.995 | 6.207 | 5.070 | 4.988 | 4.126 | 3.632 | 3.460 | 3.044 | 3.203 | 2.847 | 2.644 | 2.525 | 2.519 | 1.992 | 1.795 | 1.451 | 1.508 |

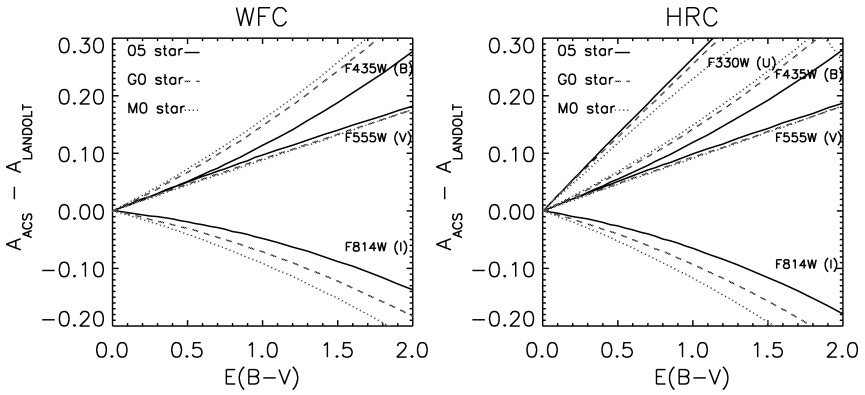


FIG. 18.—Difference in extinction between the ACS system and the ground system as a function of $E(B - V)$.

calibration papers by John Holtzman and collaborators. We are indebted to them for setting a benchmark in comprehensive calibration papers, making our job much easier.

M. S. is particularly grateful to the ACS IDT team and all personnel of the Johns Hopkins University Physics and Astronomy department for 5 years of pleasant and productive work. Finally, we are grateful to K. Anderson, S. Busching, A. Framarini, S. Barkhouser, and T. Allen for their invaluable contributions to the ACS project at JHU.

We have much appreciated the many useful suggestions and constructive criticism of Gordon Walker, the referee of this paper, whose valuable help has considerably improved the presentation of our work.

ACS was developed under NASA contract NAS 532865, and this research has been supported by NASA grant NAG5-7697 and by equipment grant from Sun Microsystems, Inc. The Space Telescope Science Institute is operated by AURA Inc., under NASA contract NAS 526555.

## APPENDIX A

## ACRONYMS

ACS: Advanced Camera for Surveys
ADHv4: ACS Data Handbook version 4.0
ADU: Analog-to-digital unit
AIHv5: ACS Instrument Handbook version 5.0
BPGS: Bruzual, Perrson, Gunn, and Stryker stellar atlas
CALACS: Calibration pipeline for ACS data
CCD: Charge coupled device
CTE: Charge transfer efficiency
EE: Encircled energy
FOV: Field of view
FWHM: Full width at half-maximum
GSFC: Goddard Space Flight Center
HRC: High Resolution Channel
*HST*: *Hubble Space Telescope*
IR: Infrared
MPP: Multipinned phase
OTA: Optical Telescope Assembly
PSF: Point-spread function
RQE: Responsive quantum efficiency
SED: Spectral energy distribution
SMOV: Servicing Mission Orbital Verification
STIS: Space Telescope Imaging Spectrograph
STScI: Space Telescope Science Institute
SBC: Solar blind channel
Tiny Tim: Program that produces simulated *HST* point-spread functions
UV: Ultraviolet
WFC: Wide Field Channel
WFPC2: Wide Field and Planetary Camera 2

## APPENDIX B

## PHOTOMETRIC CALIBRATION COOKBOOK

Here we briefly summarize the steps required to perform photometry on an ACS image. See also ADHB03.

### B1. POINT-SOURCE PHOTOMETRY

1. Retrieve the image(s) from the *HST* archive or proceed with the manual recalibration of the data, following the recipe given in ADHv4. Be sure to use the best reference files, usually available a few weeks after the data acquisition.

2. After running CALACS on the association file, the main output is the flat-field-corrected FLT image and/or the geometric corrected DRZ image.

*i.* If CR-SPLIT observations are available, the FLT images are combined to produce a CRJ frame free of cosmic rays. We draw the reader's attention to the fact that the default settings for the CR rejection routine are quite conservative. If the images in the CR-SPLIT pair do not show any significant offset (<0.05 pixel), the `scalenoise` parameter may be reduced a more efficient CR rejection (see § 3.5). However, in the case of undersampled images, one should verify that the peak of the PSF is not affected (i.e., truncated) by a more "aggressive" CR-removal technique.

*ii*. If instead the observation consisted of dithered images but without CR-SPLIT, the resulting FLT images will still have cosmic rays, which are removed during the combination of the dithered observations. MultiDrizzle performs a better CR-rejection on non–CR-splitted observations than PyDrizzle.[25]

3. Perform photometry of objects in the field using any choice of photometry technique.

*i*. If work is carried out on the FLT image instead of the distortion-corrected DRZ file, it is necessary to multiply each SCI (and ERR) frame of the FLT file by the appropriate pixel area map file (see § 3.6). This operation will ensure that the total integrated flux of the star is conserved. We emphasize here that even after the application of the pixel area map, the PSF of the stars will be distorted, and the amount of distortion is position dependent. The encircled energy (EE) profiles published in this paper were calculated from nondistorted PSFs. As a consequence, the aperture correction that can be derived from the EE profile cannot be directly applied to nondrizzled images, at least for small-radius apertures. The zero points published in this paper refer to an "infinite" aperture and can be used once the aperture correction to a "total" flux has been applied.

*ii*. The units of the FLT and DRZ images are $e^-$ and $e^-$ $s^{-1}$, respectively. Many photometry packages for PSF fitting use an optimal weighting scheme that depends on the readout noise, gain, and the true counts in the pixels. As a consequence, in order to compute the weights correctly, the image should not be divided by the exposure time. Therefore, the DRZ image should be multiplied by the exposure time before running such packages. The total number of electrons, instead of the electron rate, is also needed in order to properly calculate the CTE correction. For the same reasons, the background sky should not be subtracted from the image.

*iii*. When performing aperture or PSF fitting photometry, possible systematic errors due to the spatial variation of the PSF should be addressed. This is particularly important when the photometry is carried out using a small-radius aperture (<5 pixels). For very small aperture ($r < 2$ pixels) the systematic variations in aperture correction can be as high as 10%–15%. An example of the analysis of the optimal aperture is provided in Appendix F.

This step should give you a set of measurements in units of electrons or $e^-$ $s^{-1}$ in your selected aperture for all your objects. The instrumental magnitude can be calculated as $-2.5 \times \log(e \times s^{-1})$.

4. Consider correcting the photometry for CTE degradation. Unless your data were acquired in the first semester of 2002, the effects of CTE degradation are probably present in your data. Check on the STScI ACS Web page for updates on the CTE degradation correction. There are several things to keep in mind when calculating the correction for CTE degradation in your image:

*i*. The flux level and the background level to use in the formula are in electrons and not $e^-$ $s^{-1}$. When working with DRZ images, it is necessary to multiply the measured value by the exposure time.

*ii.* When applying the CTE correction to combined images, each of the combined images must have the same or very similar exposure times. The output of CALACS, when CR-SPLIT or DRZ observations are available, is the sum of the combined images. In this case, if all the combined images have the same exposure time, the measured values in the equation, such as SKY and FLUX, should be divided by the number of images used to create the add-combine image. Determining the CTE correction for a combined image created with unequal exposure times (for example, one long exposure and one short exposure) cannot easily be done.

*iii.* In particular for WFC observations, the FOV is large enough that the background sky might present gradients. In general, the use of a constant sky value for the determination of CTE correction in different regions of the FOV is not recommended. This is particularly true for all filters where the PSF wings are broadened by the long-wavelength halo. Depending on the brightness of the star, the signal in the PSF wings can enhance the "local" sky and reduce the amount of lost signal within the aperture where the flux is measured. In

[25] Since 2004 September, MultiDrizzle has been part of CALACS. See ADHB03 for more information on running MultiDrizzle on ACS images.

such instances a global sky value would overestimate the CTE correction.

5. Apply the aperture correction to all photometric measurements to transform the instrumental magnitudes into OBMAG:

*i*. For filters bluer than F775W, determine the offset between your photometry and aperture photometry with a 0.″5 radius aperture. This is usually done by measuring a few bright isolated objects in the field. Apply this offset to all the photometric measurements. Use Table 5 to get the value of AC05 for each filter. Add AC05 to the instrumental magnitude or insert the count rate at $r = 0.''5$ and the value of AC05 in equation (2) to get OBMAG.

*ii*. For all near-IR filters, if your object is a blue star proceed as in (*i*). For all other objects, you need to estimate the impact of the *red halo*: first estimate the effective wavelength of the observation using the recipe in § 4.5, SYNPHOT, or Table 8. Then calculate the aperture correction from a 0.″5 aperture radius to infinity using the relation in Figures 9 and 10 and Tables 6 and 7 and compare the results with the values in Table 5. If the calculated aperture correction is similar, within a few tenths of a percent, to the corresponding value in Table 5, then the red halo has little or no impact on your observations and you should proceed as in (*i*). If, however, the difference is larger, then you should use the relation in Figures 9 and 10 and Tables 6 and 7 to directly calculate the aperture correction from your aperture radius to infinity.

6. Apply the appropriate zero point from Tables 10 and 11 to transform OBMAG to any choice of magnitude system.

7. If your observations were processed with CALACS before 2004 January 6, and the gain is different from the default setting (1 for WFC, 2 for HRC), use Table 9 to correct the photometry.

8. The magnitude can be corrected for interstellar extinction using Tables 14 and 15. Given $E(B - V)$, the extinction $A(P)$ in the passband $P$ is calculated by multiplying $E(B - V)$ by the value in the table that correspond to the correct passband and spectral type.

9. If you want to transform the data to a different photometric system, use equation (12) with the coefficients in § 8 that are appropriate for the source and target systems. You should apply the correction for interstellar extinction (see § 10) before applying the transformations.

### B2. RESOLVED OBJECT PHOTOMETRY

1. Retrieve the image(s) from the *HST* archive or proceed with the manual recalibration of the data, following the recipe given in ADHv4. Be sure to use the best reference files, usually available a few weeks after the data acquisition.

2. After running CALACS on the association file, the main output is the flat-field–corrected FLT image and/or the geometrically corrected DRZ image (see point 2 in Appendix B.1).

3. Perform photometry of objects in the field using any choice of photometry technique (see point 3 in Appendix B.1). This step should give you a set of measurements in units of electrons or $e^-$ s$^{-1}$ in your selected aperture for all your objects. The instrumental magnitude can be calculated as $-2.5 \times \log(e \times \mathrm{s}^{-1})$.

4. Consider correcting the photometry for CTE degradation. Unless your data were acquired in the first semester of 2002, due to the large number of transfers, the effects of CTE degradation are probably present in your data. Check on the STScI ACS Web page for updates on the CTE degradation correction (see point 4 in Appendix B.1).

5. Apply the aperture corrections to transform the instrumental magnitudes into OBMAG: these will of course in general be different for extended objects and for stars, so the corrections given in the tables should not be applied blindly. However, for barely resolved galaxies, the aperture corrections may be similar to the stellar ones if the apertures are at least several pixels in radius. If high accuracy is required, consider simulating galaxy profiles and convolving them with the PSFs of the appropriate bandpasses to determine the amount of light lost through the adopted aperture. If one is only interested in galaxy colors for a given aperture, and the PSFs of the two bandpasses are nearly identical, this step is unnecessary; however, for colors involving the near-IR filters, particularly F850LP, there will in general be more light lost through the redder filter. In this case, one can determine the size of the differential aperture correction for the two bands by convolving galaxy models with the respective PSFs or else deconvolving the images and measuring the color change for the given aperture.

6. Apply the appropriate zero point from Tables 10 and 11 to transform OBMAG to any choice of magnitude system.

7. If your observations were processed with CALACS before 2004 January 6, and the gain is different from the default setting (1 for WFC, 2 for HRC), use Table 9 to correct the photometry.

8. The magnitude can be corrected for interstellar extinction using Tables 14 and 15. Given $E(B - V)$, the extinction $A(P)$ in the passband $P$ is calculated by multiplying $E(B - V)$ by the value in the table that correspond to the correct passband and spectral type.

9. If you want to transform the data to a different photometric system, see Appendix E. You should apply the correction for interstellar extinction (see § 10) before applying the transformations.

### B3. SURFACE PHOTOMETRY

1. Retrieve the image(s) from the *HST* archive or proceed with the manual recalibration of the data, following the recipe given in ADHv4. Be sure to use the best reference files, usually available a few weeks after the data acquisition.

2. After running CALACS on the association file, the main output is the flat-field–corrected FLT image and/or the geometrically corrected DRZ image (see point 2 in Appendix B.1).

3. Measure the surface brightness in units of $e\ s^{-1}$ pixel$^{-1}$. If one is interested in absolute surface photometry within a single bandpass, we recommend using the distortion-corrected (DRZ) image and converting from flux per pixel to flux per arcsec$^2$ via the output pixel scale used in the drizzling process. The FLT images may also be used, and since the pixel area variation has been divided out by applying the flat field, it is not necessary to apply the pixel area map. However, in this case, the appropriate factor to use in the conversion from pixel area to arcsec$^2$ depends on the mean pixel scale over the detector region used in normalization of the flat fields. Of course, if one is only interested in surface colors, this factor cancels out (since the flat fields for different bandpasses were normalized in the same way), and the colors can be determined simply from the flux per pixel in the two bands.

4. The effect of the PSF red halo should also be considered in doing surface photometry of extended objects in near-IR filters (see discussion in § 4.3).

5. Convert the count rate into OBMAG arcsec$^{-2}$ using the appropriate pixel scale.

6. Apply the appropriate zero point from Tables 10 and 11 to transform OBMAG arcsec$^{-2}$ to a surface brightness in your choice of magnitude system.

7. If your observations were processed with CALACS before 2004 January 6, and the gain was different from the default setting, use Table 9 to correct the photometry.

8. If you want to transform the data to a different photometric system, use equation (12) with the coefficients in § 8 that are appropriate for the source and target systems. For the color conversion of galaxies use the instructions in Appendix E. You should apply the correction for interstellar extinction before applying the transformations.

## APPENDIX C

## APERTURE CORRECTION FOR RED OBJECTS: EXAMPLES

### C1. CASE 1: PHOTOMETRY OF A HIGH-REDSHIFT GALAXY

The red "halo" can affect both the magnitude and the color of a galaxy. The most commonly used software for performing photometry of galaxies is SExtractor (Bertin & Arnouts 1996), which provides several measurements of the magnitude. The most commonly used for faint galaxy photometry is MAG_AUTO, an aperture magnitude measured within an elliptical aperture adapted to the shape of the object and with a width scaled $n$ times the isophotal radius. Other common choices are MAG_ISO, an isophotal magnitude that measures the integrated light above a certain threshold, and MAG_APER, a circular aperture. MAG_AUTO is the best choice for estimating total magnitudes, but even for filters not affected by long-wavelength light scattering it excludes a significant amount of the light (Benítez et al. 2004). In order to accurately measure the color of galaxies, it is quite common to adopt a single aperture defined by a detection image[26] and selecting MAG_ISO or MAG_APER. If all filters have similar PSFs, then the magnitude measurements in all filters will be affected by the same systematic errors that cancel out when subtracting the magnitudes to calculate the colors. If the PSFs are different, then an aperture correction ought to be applied to the magnitudes in each filter.

[26] A detection image is either an image from a chosen band or the weighted sum of images obtained in different bands.

TABLE 16
EFFECTIVE WAVELENGTH AND EE WITH LONG-WAVELENGTH LIGHT SCATTERING AND SYNPHOT

| Instrument Parameter | F775W | F850LP |
|---|---|---|
| WFC: | | |
| $\lambda_{\rm eff}$ (Å) ..... | 8026.2 | 9125.4 |
| EE($r$ = 0.″3) ..... | 0.879 | 0.816 |
| HRC: | | |
| $\lambda_{\rm eff}$ (Å) ..... | 7997.0 | 9210.8 |
| EE($r$ = 0.″3) ..... | 0.809 | 0.674 |

For this simulation we use a model of a SB2 galaxy at redshift $z = 5.8$ normalized to a magnitude ABMAG = 26.0 in the F850LP filter. The color of this galaxy is F775W − F850LP = 1.65 (1.71) in ABMAG WFC (HRC) system. Using the data of the characterization of the long-wavelength light scattering and SYNPHOT, we estimate that the effective wavelength $\lambda_{\rm eff}$ and the fraction of the total light enclosed in a 0.″3 aperture radius at the calculated $\lambda_{\rm eff}$ (see Table 16). If we remove the AB zero points and scale the total counts for the EE for an aperture of 0.″3 radius, we obtain the OBMAG presented in Table 17.

TABLE 17
OBMAG

| Instrument | F775W | F850LP |
|---|---|---|
| WFC ..... | 2.14 | 1.36 |
| HRC ..... | 2.99 | 2.04 |

At this point there are two options: treat the measured counts as total counts, or decide to apply an aperture correction. The aperture correction can be calculated from different sources, from stars in the FOV, from the tabulated EE for the standard stars, using SYNPHOT, or calculating the effective wavelength and Tables 6 and 7. In Table 18 we report the different cases and show the different results.

TABLE 18
APERTURE CORRECTION: CASE 1

| | WFC | | | | HRC | | | |
|---|---|---|---|---|---|---|---|---|
| ASSUMPTION | apt_c F775W | apt_c F850LP | F850LP | F775W−F850LP | apt_c F775W | apt_c F850LP | F850LP | F775W−F850LP |
| Input data | … | … | 26.00 | 1.65 | … | … | 26.00 | 1.71 |
| The counts in 0.″3 are the total counts | … | … | 26.22 | 1.57 | … | … | 26.43 | 1.51 |
| The counts in 0.″3 need to be corrected using the same correction for both filters: | | | | | | | | |
| F775W apt_c from the EE of WDs | 0.14 | 0.14 | 26.08 | 1.57 | 0.18 | 0.18 | 26.25 | 1.51 |
| F850LP apt_c from the EE of WDs | 0.19 | 0.19 | 26.03 | 1.57 | 0.40 | 0.40 | 26.03 | 1.51 |
| The counts in 0.″3 need to be corrected using different corrections in different filters: | | | | | | | | |
| apt_c from the EE of WDs | 0.14 | 0.19 | 26.03 | 1.62 | 0.18 | 0.40 | 26.03 | 1.73 |
| apt_c from Tables 6 and 7 | 0.15 | 0.22 | 26.00 | 1.64 | 0.22 | 0.45 | 26.02 | 1.74 |
| Using SYNPHOT | 0.14 | 0.24 | 25.98 | 1.66 | 0.23 | 0.47 | 25.96 | 1.75 |

## C2. CASE 2: PHOTOMETRY OF AN L-DWARF STAR

For this example we simulate observations of an L3.5 star with magnitude VEGAMAG = 22.00 in the WFC F775W filter. The color of this star is F775W − F850LP = 1.84 (1.99) in VEGAMAG WFC (HRC) system. For this example we perform photometry in a 0.″2 (4 pixels) radius aperture for WFC, and a 0.″1 (4 pixels) radius aperture for HRC. Using the observed spectra of the L3.5 star 2M0036+18 and SYNPHOT, we estimate the effective wavelength $\lambda_{eff}$ of the observations and the fraction of the total light enclosed in the selected aperture radius (Table 19). If we remove the VEGAMAG zero points and scale the total counts for the EE and an aperture of 4 pixels radius, we obtain the instrumental magnitude given in Table 20.

At this point it is important to address the issue of the aperture correction. The aperture correction can be calculated from different sources, from stars in the FOV, from the tabulated EE for the standard stars, using SYNPHOT, or calculating the effective wavelength and using Tables 6 and 7. In Table 21 we report the different cases and show the different results.

TABLE 19
EFFECTIVE WAVELENGTH AND EE WITH 2M 0036+18 AND SYNPHOT

| Instrument Parameter | F775W | F850LP |
|---|---|---|
| WFC: | | |
| $\lambda_{eff}$ (Å) | 8003.7 | 9383.5 |
| EE($r$ = 0.″2) | 0.829 | 0.718 |
| HRC: | | |
| $\lambda_{eff}$ (Å) | 7980.4 | 9445.2 |
| EE($r$ = 0.″1) | 0.629 | 0.414 |

TABLE 20
INSTRUMENTAL MAGNITUDES

| Instrument | F775W | F850LP |
|---|---|---|
| WFC | −3.05 | −3.81 |
| HRC | −2.00 | −2.70 |

TABLE 21
APERTURE CORRECTION: CASE 2

| | WFC | | | | HRC | | | |
|---|---|---|---|---|---|---|---|---|
| ASSUMPTION | apt_c F775W | apt_c F850LP | F775W | F775W−F850LP | apt_c F775W | apt_c F850LP | F775W | F775W−F850LP |
| Input data | … | … | 22.00 | 1.84 | … | … | 22.05 | 1.99 |
| Measured data in aperture | … | … | 22.20 | 1.69 | … | … | 22.55 | 1.54 |
| apt_c from the EE of WDs | 0.19 | 0.27 | 22.01 | 1.77 | 0.50 | 0.83 | 22.06 | 1.88 |
| apt_c from Tables 6 and 7 | 0.20 | 0.37 | 22.00 | 1.86 | 0.54 | 0.98 | 22.02 | 1.98 |
| Using SYNPHOT | 0.20 | 0.39 | 22.00 | 1.87 | 0.55 | 1.00 | 22.01 | 1.99 |

## APPENDIX D

## SUPPORTING MATERIAL FOR COLOR TRANSFORMATIONS

All figures and tables in this appendix are in support of §§ 8.3 and 8.4. Readers should read the appropriate section before using the coefficient listed in these tables in equation (12).

### D1. EXAMPLE

Here we present, as an example, a transformation between the HRC and the WFC photometric systems. Suppose we observed the globular cluster NGC 2419 with ACS/HRC in F555W and F814W and have stored the photometric tables in the ABMAG HRC photometric system. We want to compare this result with previous WFC observations of the same cluster in the VEGAMAG system. This is the procedure that we need to follow, step by step:

1. Transform the HRC ABMAG photometry to OBMAG.

This is simply done by subtracting the ABMAG zero points (Table 11) from our data set:

$$\mathrm{F555W}_{\mathrm{HRC,\,OBMAG}} = \mathrm{F555W}_{\mathrm{HRC,\,ABMAG}} - 25.248,$$

$$\mathrm{F814W}_{\mathrm{HRC,\,OBMAG}} = \mathrm{F814W}_{\mathrm{HRC,\,ABMAG}} - 25.287.$$

2. Compute the first estimate of TCOL. This is the less critical step and can be done by simply assuming

$$\mathrm{F555W}_{\mathrm{WFC,\,OBMAG}} = \mathrm{F555W}_{\mathrm{HRC,\,OBMAG}},$$

$$\mathrm{F814W}_{\mathrm{WFC,\,OBMAG}} = \mathrm{F814W}_{\mathrm{HRC,\,OBMAG}},$$

$$\mathrm{TCOL} \equiv \mathrm{F555W}_{\mathrm{HRC,\,OBMAG}} - \mathrm{F814W}_{\mathrm{HRC,\,OBMAG}}$$

$$\simeq \mathrm{F555W}_{\mathrm{WFC,\,OBMAG}} - \mathrm{F814W}_{\mathrm{WFC,\,OBMAG}}.$$

3. Transform $\mathrm{F555W}_{\mathrm{HRC,\,OBMAG}}$ to $\mathrm{F555W}_{\mathrm{WFC,\,OBMAG}}$. From Table 13, we select the coefficients in the "synthetic" column for SMAG = F555W, TMAG = F555W, and TCOL = F555W − F814W and use them in equation (12):

$$\mathrm{F555W}_{\mathrm{WFC,\,OBMAG}} = \mathrm{F555W}_{\mathrm{HRC,\,OBMAG}} - 0.470 - 0.004\mathrm{TCOL} + 0.000\mathrm{TCOL}^2$$

4. Transform $\mathrm{F814W}_{\mathrm{HRC,\,OBMAG}}$ to $\mathrm{F814W}_{\mathrm{WFC,\,OBMAG}}$. We proceed similarly to step 3 for the F555W but in the "synthetic " column for SMAG = F814W, TMAG = F814W, and TCOL = F555W − F814W there are two sets of coefficients depending on the value of TCOL:

for TCOL $< -0.2$,

$$\mathrm{F814W}_{\mathrm{WFC,\,OBMAG}} = \mathrm{F814W}_{\mathrm{HRC,\,OBMAG}} - 0.655 - 0.012\mathrm{TCOL} - 0.031\mathrm{TCOL}^2,$$

and for TCOL $> -0.2$,

$$\mathrm{F814W}_{\mathrm{WFC,\,OBMAG}} = \mathrm{F814W}_{\mathrm{HRC,\,OBMAG}} - 0.651 + 0.003\mathrm{TCOL} + 0.003\mathrm{TCOL}^2.$$

5. Now we have better estimate of $\mathrm{F555W}_{\mathrm{WFC,\,OBMAG}}$ and $\mathrm{F814W}_{\mathrm{WFC,\,OBMAG}}$ from steps (2) and (3). Obviously, TCOL should be updated:

$$\mathrm{TCOL} = \mathrm{F555WW}_{\mathrm{WFC,\,OBMAG}} - \mathrm{F814W}_{\mathrm{WFC,\,OBMAG}}.$$

6. Repeat steps 3 trough 5 until convergence is reached. Usually not more than 10 iterations are needed.

7. Convert $\mathrm{F555W}_{\mathrm{WFC,\,OBMAG}}$ and $\mathrm{F814W}_{\mathrm{WFC,\,OBMAG}}$ into VEGAMAG by adding the zero points from Table 10:

$$\mathrm{F555W}_{\mathrm{WFC,\,VEGAMAG}} = \mathrm{F555W}_{\mathrm{WFC,\,ABMAG}} + 25.711$$

$$\mathrm{F814W}_{\mathrm{WFC,\,VEGAMAG}} = \mathrm{F814W}_{\mathrm{WFC,\,ABMAG}} + 25.487$$

In Figure 19 we show the comparison between the HRC-to-WFC transformed magnitude and the WFC photometry, overplotting the transformed magnitudes in the observed WFC CMD and plotting the differences in magnitude in the two filters as a function of the color.

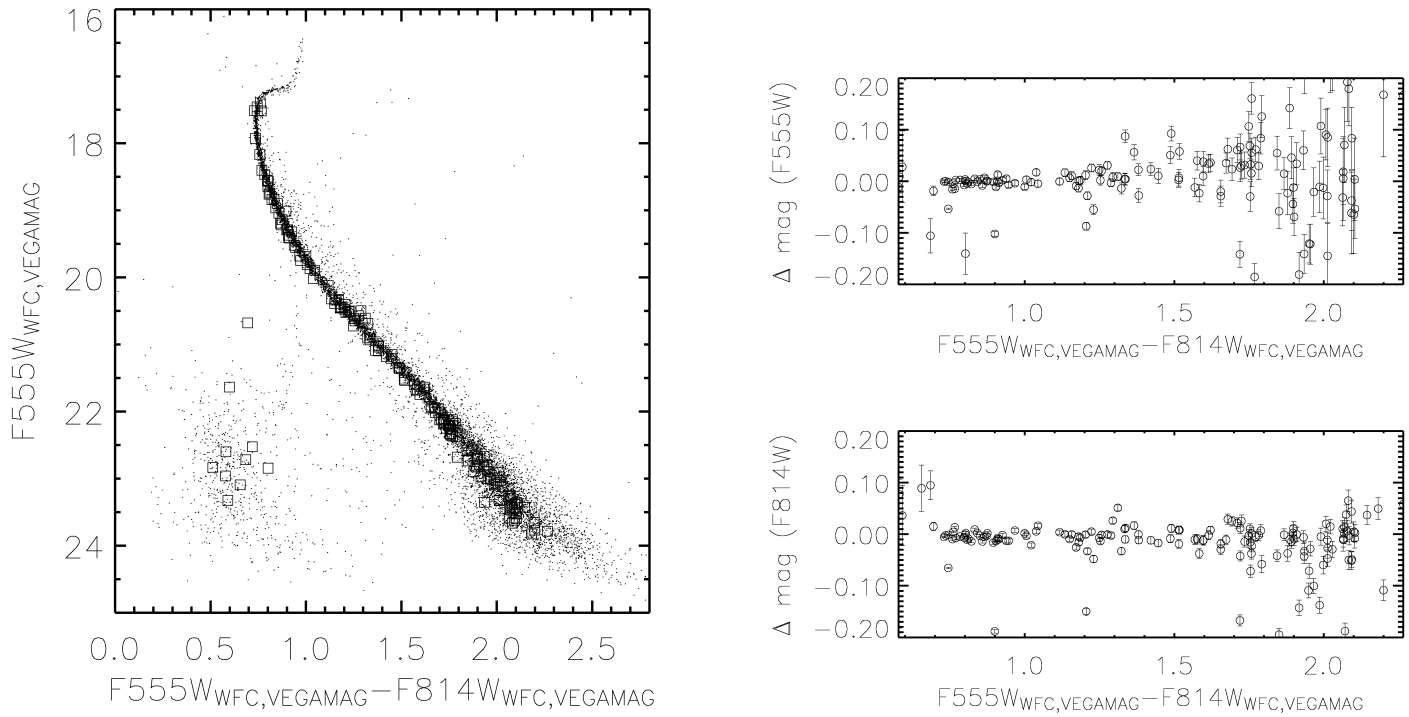


FIG. 19.—*Left*: HRC photometry of NGC 104 *(open square)* transformed into the WFC observational plane of WFC. *Right*: Difference in magnitude (transformed HRC−WFC) in the two filters as a function of color.

## D2. TRANSFORMATION FROM ACS TO *UBVRI*

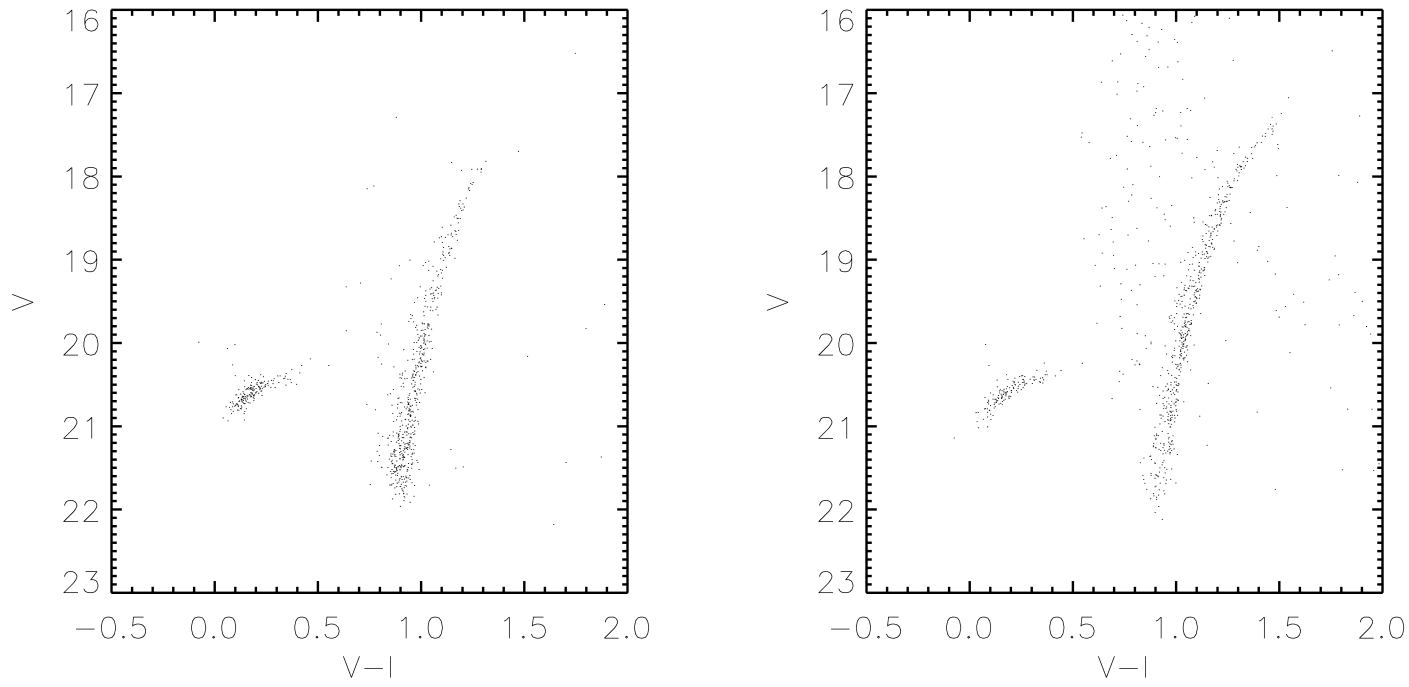


FIG. 20.—Observed CMDs for NGC 2419 from Saha et al. (2005; *left*) and P. Stetson (see footnote 19; *right*).

TABLE 22
COEFFICIENTS FOR THE TRANSFORMATION FROM WFC TO *BVRI*

| SOURCE | TARGET | | OBSERVED | | | SYNTHETIC | | | |
|---|---|---|---|---|---|---|---|---|---|
| SMAG | TMAG | TCOL | c0 | c1 | c2 | c0 | c1 | c2 | TCOL Range[a] |
| F435W ..... | *B* | $B-V$ | 25.842 ± 0.023 | −0.089 ± 0.024 | 0.000 ± 0.000 | 25.769 ± 0.004 | 0.029 ± 0.012 | −0.156 ± 0.055 | <0.4 |
| | | | | | | 25.709 ± 0.007 | 0.108 ± 0.009 | −0.068 ± 0.002 | >0.4 |
| | *B* | $B-R$ | | | | 25.769 ± 0.004 | 0.027 ± 0.008 | −0.073 ± 0.028 | <0.6 |
| | | | | | | 25.743 ± 0.008 | 0.022 ± 0.007 | −0.013 ± 0.001 | >0.6 |
| | *B* | $B-I$ | 25.847 ± 0.021 | −0.045 ± 0.011 | 0.000 ± 0.000 | 25.768 ± 0.004 | 0.022 ± 0.006 | −0.038 ± 0.011 | <1.0 |
| | | | | | | 25.749 ± 0.009 | 0.008 ± 0.006 | −0.005 ± 0.001 | >1.0 |
| F475W ..... | *B* | $B-V$ | | | | 26.146 ± 0.002 | 0.389 ± 0.004 | 0.032 ± 0.001 | ... |
| | *B* | $B-R$ | | | | 26.150 ± 0.004 | 0.291 ± 0.008 | −0.110 ± 0.028 | <0.6 |
| | | | | | | 26.015 ± 0.008 | 0.433 ± 0.007 | −0.046 ± 0.001 | >0.6 |
| | *B* | $B-I$ | | | | 26.145 ± 0.004 | 0.220 ± 0.006 | −0.050 ± 0.011 | <1.0 |
| | | | | | | 25.875 ± 0.009 | 0.456 ± 0.006 | −0.053 ± 0.001 | >1.0 |
| F555W ..... | *V* | $B-V$ | 25.701 ± 0.012 | −0.056 ± 0.013 | 0.000 ± 0.000 | 25.714 ± 0.004 | −0.083 ± 0.032 | 0.020 ± 0.115 | <0.2 |
| | | | | | | 25.720 ± 0.005 | −0.087 ± 0.007 | 0.004 ± 0.002 | >0.2 |
| | *V* | $V-R$ | 25.703 ± 0.009 | −0.100 ± 0.016 | 0.000 ± 0.000 | 25.720 ± 0.005 | −0.197 ± 0.062 | 0.159 ± 0.756 | <0.1 |
| | | | | | | 25.724 ± 0.005 | −0.159 ± 0.010 | 0.018 ± 0.004 | >0.1 |
| | *V* | $V-I$ | 25.704 ± 0.020 | −0.054 ± 0.020 | 0.000 ± 0.000 | 25.719 ± 0.004 | −0.088 ± 0.014 | 0.043 ± 0.068 | <0.4 |
| | | | | | | 25.735 ± 0.006 | −0.106 ± 0.007 | 0.013 ± 0.001 | >0.4 |
| F606W ..... | *V* | $B-V$ | 26.399 ± 0.038 | 0.193 ± 0.045 | 0.000 ± 0.000 | 26.410 ± 0.003 | 0.170 ± 0.005 | 0.061 ± 0.002 | ... |
| | *V* | $V-R$ | 26.341 ± 0.041 | 0.444 ± 0.083 | 0.000 ± 0.000 | 26.392 ± 0.006 | 0.310 ± 0.077 | 0.266 ± 0.945 | <0.1 |
| | | | | | | 26.372 ± 0.006 | 0.477 ± 0.013 | −0.001 ± 0.005 | >0.1 |
| | *V* | $V-I$ | 26.325 ± 0.057 | 0.236 ± 0.058 | 0.000 ± 0.000 | 26.394 ± 0.005 | 0.153 ± 0.018 | 0.096 ± 0.085 | <0.4 |
| | | | | | | 26.331 ± 0.008 | 0.340 ± 0.008 | −0.038 ± 0.002 | >0.4 |
| F625W ..... | *R* | $B-R$ | | | | 25.717 ± 0.003 | −0.041 ± 0.003 | −0.003 ± 0.001 | ... |
| | *R* | $V-R$ | 25.720 ± 0.009 | −0.098 ± 0.021 | 0.000 ± 0.000 | 25.720 ± 0.005 | −0.147 ± 0.041 | 0.043 ± 0.404 | <0.2 |
| | | | | | | 25.684 ± 0.007 | 0.042 ± 0.014 | −0.184 ± 0.005 | >0.2 |
| | *R* | $R-I$ | 25.726 ± 0.017 | −0.110 ± 0.041 | 0.000 ± 0.000 | 25.720 ± 0.003 | −0.107 ± 0.009 | −0.101 ± 0.005 | ... |
| F775W ..... | *I* | $B-I$ | | | | 25.239 ± 0.008 | −0.030 ± 0.012 | −0.002 ± 0.023 | <1.0 |
| | | | | | | 25.216 ± 0.019 | −0.002 ± 0.012 | −0.007 ± 0.002 | >1.0 |
| | *I* | $V-I$ | 25.240 ± 0.013 | −0.054 ± 0.015 | 0.000 ± 0.000 | 25.241 ± 0.005 | −0.061 ± 0.021 | 0.002 ± 0.021 | <1.2 |
| | | | | | | 25.292 ± 0.033 | −0.105 ± 0.026 | 0.007 ± 0.004 | >1.2 |
| | *I* | $R-I$ | 25.242 ± 0.013 | −0.106 ± 0.030 | 0.000 ± 0.000 | 25.240 ± 0.008 | −0.119 ± 0.052 | 0.001 ± 0.499 | <0.2 |
| | | | | | | 25.242 ± 0.012 | −0.133 ± 0.030 | 0.002 ± 0.013 | >0.2 |
| F814W ..... | *I* | $B-I$ | | | | 25.490 ± 0.011 | 0.013 ± 0.060 | −0.028 ± 0.112 | <0.3 |
| | | | | | | 25.495 ± 0.014 | −0.010 ± 0.010 | 0.006 ± 0.002 | >0.3 |
| | *I* | $V-I$ | 25.495 ± 0.015 | −0.002 ± 0.017 | 0.000 ± 0.000 | 25.489 ± 0.013 | 0.041 ± 0.211 | −0.093 ± 0.803 | <0.1 |
| | | | | | | 25.496 ± 0.010 | −0.014 ± 0.013 | 0.015 ± 0.003 | >0.1 |
| | *I* | $R-I$ | 25.492 ± 0.013 | 0.002 ± 0.030 | 0.000 ± 0.000 | 25.489 ± 0.010 | 0.068 ± 0.065 | −0.295 ± 0.624 | <0.2 |
| | | | | | | 25.478 ± 0.016 | 0.042 ± 0.038 | 0.012 ± 0.017 | >0.2 |

[a] TCOL range applies only to synthetic transformations.

TABLE 23
COEFFICIENTS FOR THE TRANSFORMATION FROM HRC TO *UBVRI*

| SOURCE | TARGET | | OBSERVED[a] | | | SYNTHETIC | | | |
|---|---|---|---|---|---|---|---|---|---|
| SMAG | TMAG | TCOL | c0 | c1 | c2 | c0 | c1 | c2 | TCOL Range[b] |
| F330W ..... | *U* | *U* − *B* | | ... | | 23.020 ± 0.008 | −0.406 ± 0.058 | 0.125 ± 0.079 | <0.2 |
| | | | | ... | | 23.064 ± 0.029 | −0.104 ± 0.058 | −0.093 ± 0.026 | >0.2 |
| | *U* | *U* − *V* | | ... | | 22.995 ± 0.012 | −0.328 ± 0.043 | 0.052 ± 0.040 | <0.3 |
| | | | | ... | | 23.001 ± 0.017 | 0.065 ± 0.021 | −0.056 ± 0.006 | >0.3 |
| | *U* | *U* − *R* | | ... | | 23.012 ± 0.012 | −0.222 ± 0.024 | 0.095 ± 0.024 | <0.6 |
| | | | | ... | | 23.050 ± 0.023 | 0.017 ± 0.019 | −0.028 ± 0.004 | >0.6 |
| | *U* | *U* − *I* | | ... | | 23.014 ± 0.012 | −0.216 ± 0.022 | 0.065 ± 0.020 | <0.7 |
| | | | | ... | | 23.040 ± 0.024 | 0.015 ± 0.018 | −0.019 ± 0.003 | >0.7 |
| F435W ..... | *B* | *U* − *B* | | ... | | 25.171 ± 0.005 | 0.005 ± 0.037 | −0.007 ± 0.046 | <0.1 |
| | | | | ... | | 25.166 ± 0.008 | −0.003 ± 0.019 | −0.010 ± 0.010 | >0.1 |
| | *B* | *B* − *V* | | ... | | 25.177 ± 0.008 | 0.048 ± 0.101 | 0.004 ± 0.280 | <0.1 |
| | | | | ... | | 25.171 ± 0.010 | 0.001 ± 0.023 | −0.016 ± 0.012 | >0.1 |
| | *B* | *B* − *R* | | ... | | 25.176 ± 0.006 | 0.014 ± 0.012 | −0.041 ± 0.031 | <0.8 |
| | | | | ... | | 25.135 ± 0.023 | 0.042 ± 0.025 | −0.017 ± 0.006 | >0.8 |
| | *B* | *B* − *I* | | ... | | 25.176 ± 0.006 | 0.011 ± 0.009 | −0.023 ± 0.017 | <1.0 |
| | | | | ... | | 25.165 ± 0.037 | 0.002 ± 0.036 | −0.003 ± 0.008 | >1.0 |
| F475W ..... | *B* | *B* − *V* | | ... | | 25.601 ± 0.004 | 0.444 ± 0.010 | 0.013 ± 0.006 | ... |
| | *B* | *B* − *R* | | ... | | 25.604 ± 0.006 | 0.310 ± 0.012 | −0.108 ± 0.041 | <0.6 |
| | | | | ... | | 25.463 ± 0.019 | 0.464 ± 0.021 | −0.050 ± 0.005 | >0.6 |
| | *B* | *B* − *I* | | ... | | 25.599 ± 0.006 | 0.233 ± 0.009 | −0.049 ± 0.017 | <1.1 |
| | | | | ... | | 25.229 ± 0.046 | 0.611 ± 0.047 | −0.097 ± 0.012 | >1.1 |
| F555W ..... | *V* | *B* − *V* | | ... | | 25.244 ± 0.013 | −0.098 ± 0.157 | −0.014 ± 0.384 | <0.0 |
| | | | | ... | | 25.238 ± 0.008 | −0.050 ± 0.020 | −0.019 ± 0.011 | >0.0 |
| | *V* | *V* − *R* | | ... | | 25.251 ± 0.005 | −0.191 ± 0.049 | 0.184 ± 0.271 | <0.3 |
| | | | | ... | | 25.269 ± 0.019 | −0.205 ± 0.048 | 0.043 ± 0.027 | >0.3 |
| | *V* | *V* − *I* | | ... | | 25.250 ± 0.005 | −0.090 ± 0.021 | 0.034 ± 0.066 | <0.6 |
| | | | | ... | | 25.275 ± 0.041 | −0.124 ± 0.075 | 0.018 ± 0.032 | >0.6 |
| F606W ..... | *V* | *B* − *V* | | ... | | 25.904 ± 0.005 | 0.156 ± 0.014 | 0.059 ± 0.009 | ... |
| | *V* | *V* − *R* | | ... | | 25.887 ± 0.008 | 0.287 ± 0.070 | 0.306 ± 0.389 | <0.3 |
| | | | | ... | | 25.848 ± 0.043 | 0.495 ± 0.132 | −0.028 ± 0.096 | >0.3 |
| | *V* | *V* − *I* | | ... | | 25.888 ± 0.009 | 0.139 ± 0.031 | 0.094 ± 0.145 | <0.4 |
| | | | | ... | | 25.805 ± 0.027 | 0.364 ± 0.044 | −0.054 ± 0.016 | >0.4 |
| F625W ..... | *R* | *B* − *R* | | ... | | 25.180 ± 0.006 | −0.053 ± 0.013 | 0.003 ± 0.008 | <2.0 |
| | | | | ... | | 25.561 ± 2.659 | −0.333 ± 2.408 | 0.047 ± 0.544 | >2.0 |
| | *R* | *V* − *R* | | ... | | 25.184 ± 0.008 | −0.158 ± 0.070 | 0.054 ± 0.389 | <0.3 |
| | | | | ... | | 25.133 ± 0.036 | 0.065 ± 0.107 | −0.201 ± 0.074 | >0.3 |
| | *R* | *R* − *I* | | ... | | 25.183 ± 0.006 | −0.143 ± 0.039 | −0.060 ± 0.079 | <0.7 |
| | | | | ... | | 25.136 ± 0.623 | −0.026 ± 1.399 | −0.136 ± 0.759 | >0.7 |
| F775W ..... | *I* | *B* − *I* | | ... | | 24.534 ± 0.009 | −0.034 ± 0.015 | −0.003 ± 0.028 | <1.0 |
| | | | | ... | | 24.491 ± 0.039 | 0.012 ± 0.032 | −0.011 ± 0.006 | >1.0 |
| | *I* | *V* − *I* | | ... | | 24.535 ± 0.007 | −0.069 ± 0.026 | 0.003 ± 0.026 | <1.2 |
| | | | | ... | | 24.597 ± 0.095 | −0.121 ± 0.095 | 0.008 ± 0.022 | >1.2 |
| | *I* | *R* − *I* | | ... | | 24.535 ± 0.007 | −0.142 ± 0.026 | −0.005 ± 0.023 | ... |
| F814W ..... | *I* | *B* − *I* | | ... | | 24.838 ± 0.012 | 0.023 ± 0.019 | −0.028 ± 0.046 | <0.8 |
| | | | | ... | | 24.824 ± 0.039 | 0.009 ± 0.033 | 0.003 ± 0.006 | >0.8 |
| | *I* | *V* − *I* | | ... | | 24.837 ± 0.016 | 0.060 ± 0.253 | −0.099 ± 0.963 | <0.1 |
| | | | | ... | | 24.838 ± 0.016 | 0.001 ± 0.024 | 0.013 ± 0.007 | >0.1 |
| | *I* | *R* − *I* | | ... | | 24.836 ± 0.036 | 0.110 ± 0.973 | −0.212 ± 5.308 | <0.0 |
| | | | | ... | | 24.834 ± 0.014 | 0.035 ± 0.050 | 0.023 ± 0.038 | >0.0 |

[a] No observed transformations are available.
[b] TCOL range applies only to synthetic transformations.

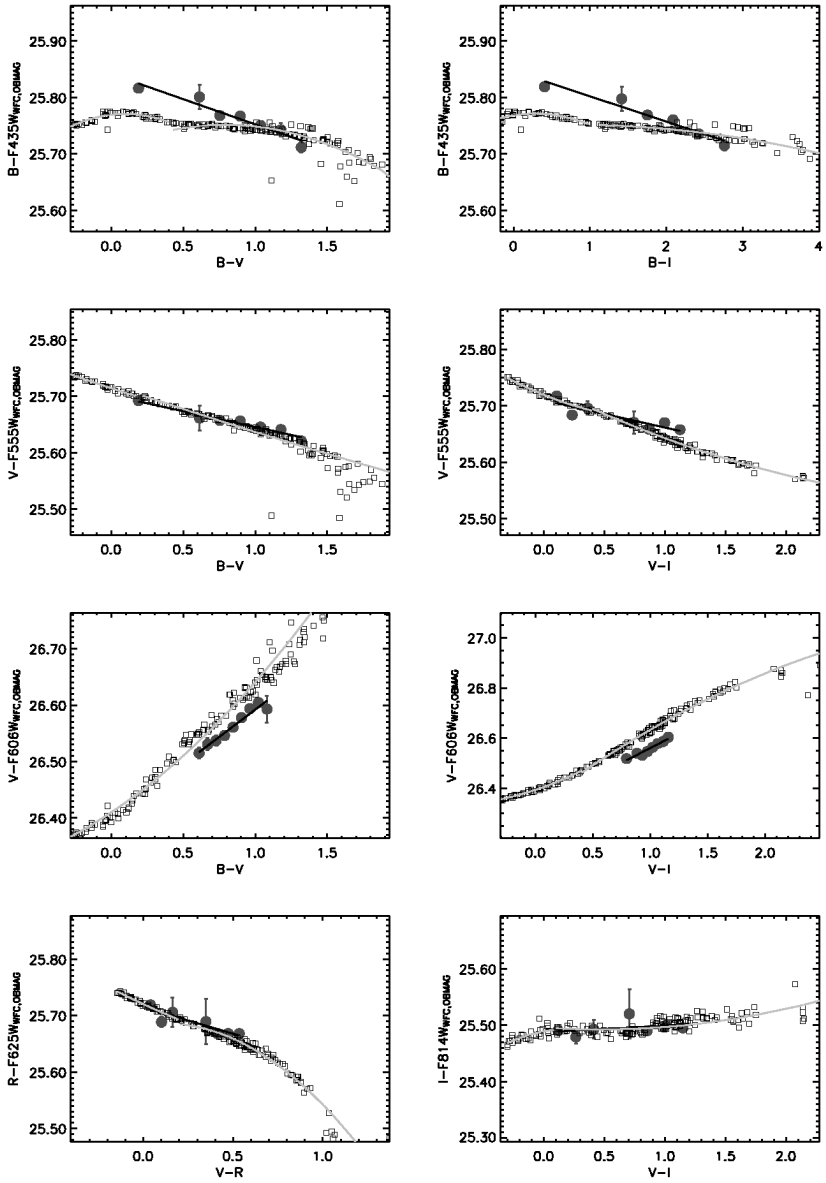


FIG. 21.—Observed and synthetic WFC-to-*BVRI* transformations for primary photometric filters. Squares show the synthetic measurements for the BPGS atlas. The circles are observational data (*filled*, NGC 104; *open*, NGC 2419). The black line shows the linear fit to the observational points; the light curve shows the synthetic transformations. [*See the electronic edition of the PASP for a color version of this figure*.]

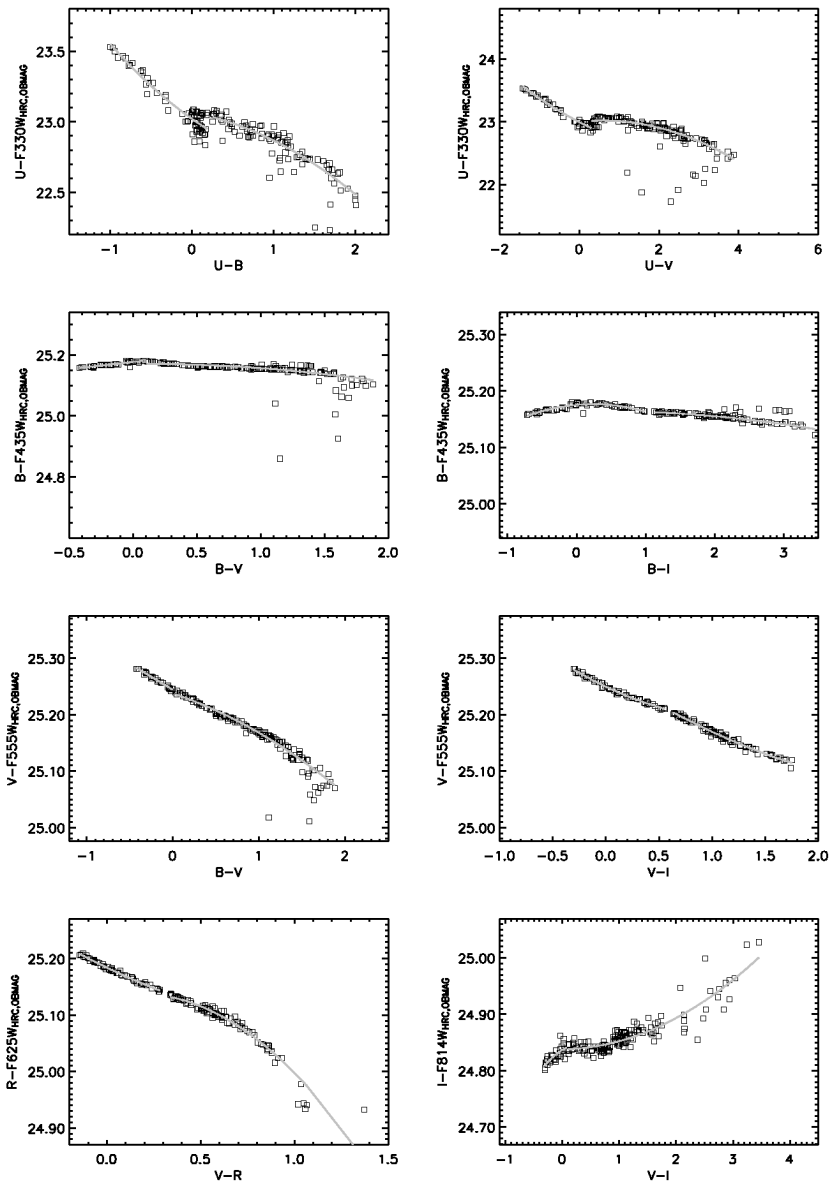


FIG. 22.—Observed and synthetic HRC-to-*UBVRI* transformations for primary photometric filters. Squares show the synthetic measurements for the BPGS atlas. The circles are observational data (*filled*, NGC 104; *open*, NGC 2419). The black line shows the linear fit to the observational points; the light curve shows the synthetic transformations. [*See the electronic edition of the PASP for a color version of this figure*.]

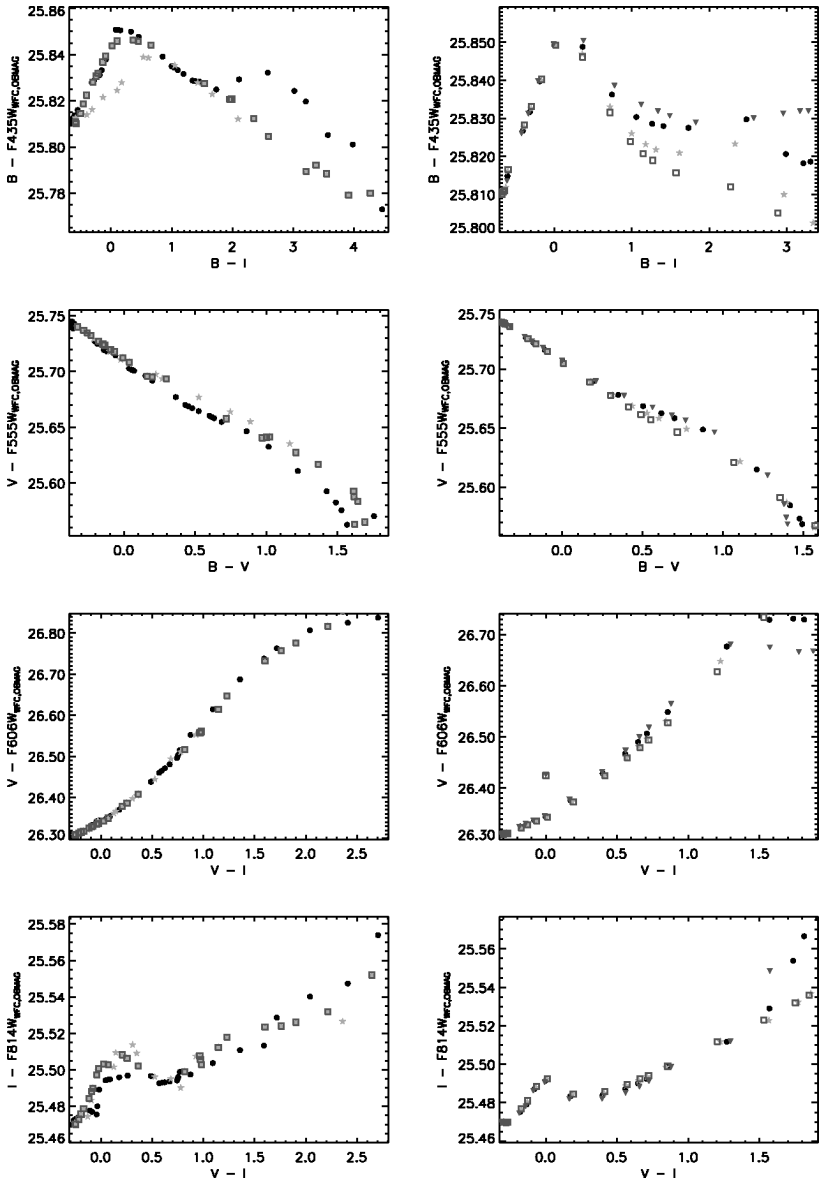


FIG. 23.—Effect of surface gravity (*left*) and metallicity (*right*) on synthetic WFC-to-*BVRI* transformation for a few primary photometric filters. *Left*: Black circles are for main-sequence stars; gray stars and squares are for giants and supergiants, respectively (all from BZ77). *Right*: Black circles are for MS stars with solar metallicity, filled triangles are [Fe/H] = 0.5, gray filled stars are [Fe/H] = −1, and squares are [Fe/H] = −2 (all from Kurucz).

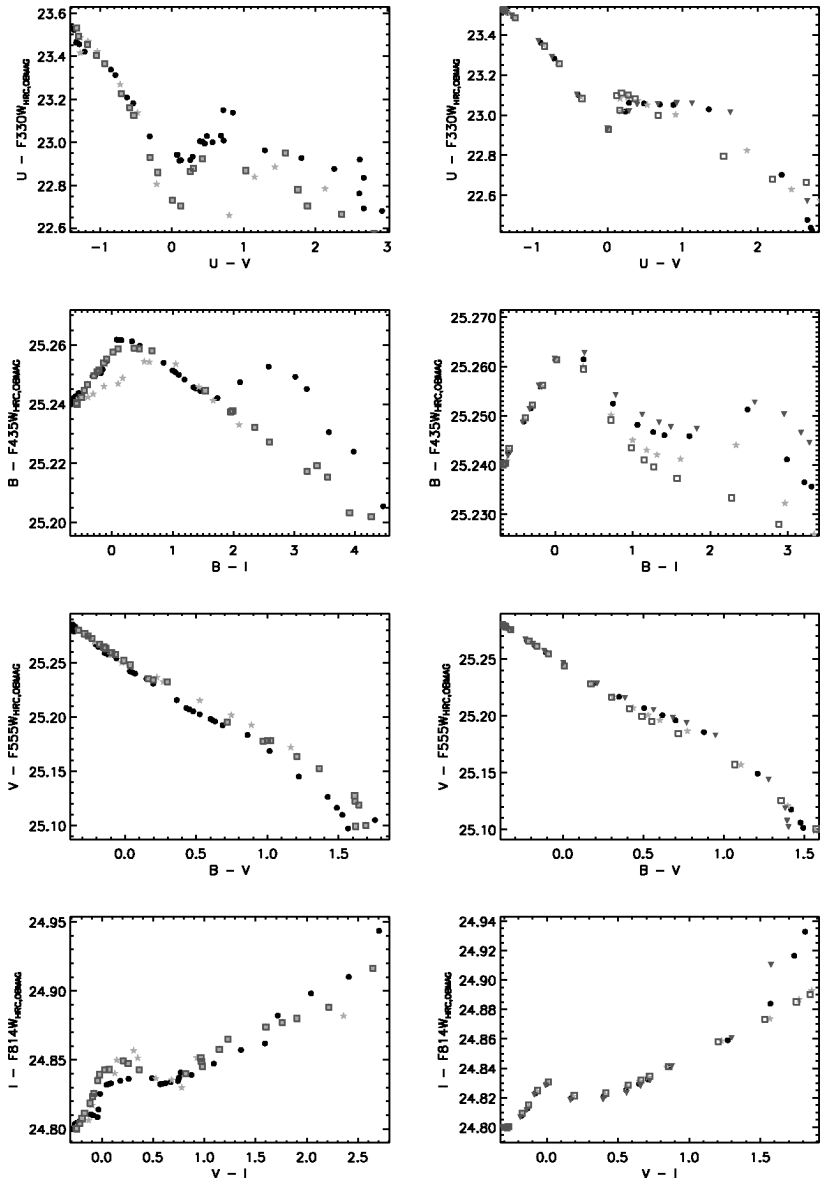


FIG. 24.—Effect of surface gravity (*left*) and metallicity (*right*) on synthetic HRC-to-*UBVRI* transformation for a few primary photometric filters. *Left*: Black circles are for main-sequence stars; gray stars and squares are for giants and supergiants, respectively (all from BZ77). *Right*: Black circles are for MS stars with solar metallicity, filled triangles are [Fe/H] = 0.5, gray-filled stars are [Fe/H] = −1, and squares are [Fe/H] = −2 (all from Kurucz).

## D3. TRANSFORMATION FROM ACS TO WFPC2

TABLE 24
COEFFICIENTS FOR THE TRANSFORMATION FROM WFC TO WFCP2

| SOURCE | TARGET | | OBSERVED | | | SYNTHETIC | | | |
|---|---|---|---|---|---|---|---|---|---|
| SMAG | TMAG | TCOL | c0 | c1 | c2 | c0 | c1 | c2 | TCOL Range[a] |
| F435W ..... | F439W | F439W−F555W | 5.550 ± 0.067 | 0.040 ± 0.029 | 0.000 ± 0.000 | 6.180 ± 1.210 | −0.605 ± 1.589 | 0.158 ± 0.520 | <1.7 |
| | | | | | | 5.655 ± 0.076 | −0.074 ± 0.060 | 0.029 ± 0.011 | >1.7 |
| | F439W | F439W−F606W | 5.783 ± 2.031 | −0.153 ± 1.594 | 0.036 ± 0.304 | 5.772 ± 1.384 | −0.054 ± 1.537 | −0.014 ± 0.425 | <2.0 |
| | | | | | | 5.638 ± 0.061 | −0.046 ± 0.039 | 0.016 ± 0.006 | >2.0 |
| | F439W | F439W−F675W | 5.567 ± 0.176 | 0.030 ± 0.074 | 0.000 ± 0.000 | 5.694 ± 0.195 | −0.066 ± 0.436 | −0.007 ± 0.237 | <1.2 |
| | | | | | | 5.627 ± 0.031 | −0.030 ± 0.025 | 0.015 ± 0.005 | >1.2 |
| | F439W | F439W−F814W | 5.600 ± 0.033 | 0.019 ± 0.015 | 0.000 ± 0.000 | 5.662 ± 0.016 | −0.108 ± 0.053 | 0.057 ± 0.037 | <1.4 |
| | | | | | | 5.614 ± 0.041 | −0.010 ± 0.031 | 0.009 ± 0.006 | >1.4 |
| | F439W | F439W−F850LP | 5.626 ± 0.058 | 0.020 ± 0.062 | 0.000 ± 0.000 | 5.558 ± 0.170 | −0.063 ± 0.265 | −0.007 ± 0.100 | <−0.9 |
| | | | | | | 5.621 ± 0.004 | 0.019 ± 0.006 | 0.008 ± 0.003 | >−0.9 |
| F555W ..... | F555W | F439W−F555W | 3.965 ± 0.090 | −0.041 ± 0.038 | 0.000 ± 0.000 | 3.886 ± 0.038 | 0.037 ± 0.033 | −0.018 ± 0.007 | … |
| | F555W | F555W−F606W | 3.911 ± 0.162 | −0.067 ± 0.292 | 0.000 ± 0.000 | 3.889 ± 0.021 | 0.120 ± 0.078 | −0.250 ± 0.067 | … |
| | F555W | F555W−F675W | 3.875 ± 0.025 | −0.047 ± 0.126 | 0.000 ± 0.000 | 3.875 ± 0.003 | −0.086 ± 0.006 | −0.069 ± 0.012 | … |
| | F555W | F555W−F814W | 3.867 ± 0.016 | −0.032 ± 0.036 | 0.000 ± 0.000 | 3.867 ± 0.003 | −0.061 ± 0.006 | −0.026 ± 0.007 | … |
| | F555W | F555W−F850LP | 3.826 ± 0.159 | −0.028 ± 0.094 | 0.000 ± 0.000 | 3.765 ± 0.010 | −0.089 ± 0.013 | −0.014 ± 0.004 | … |
| F606W ..... | F606W | F439W−F606W | 4.214 ± 0.129 | −0.012 ± 0.051 | 0.000 ± 0.000 | 4.359 ± 0.031 | −0.079 ± 0.021 | 0.008 ± 0.004 | … |
| | F606W | F555W−F606W | | | | 4.291 ± 0.569 | 0.815 ± 1.782 | 0.038 ± 1.389 | … |
| | F606W | F606W−F675W | 4.128 ± 0.046 | −0.093 ± 0.070 | 0.000 ± 0.000 | 4.182 ± 0.005 | 0.077 ± 0.015 | 0.165 ± 0.017 | … |
| | F606W | F606W−F814W | 4.132 ± 0.050 | −0.060 ± 0.053 | 0.000 ± 0.000 | 4.168 ± 0.004 | −0.016 ± 0.005 | 0.030 ± 0.004 | … |
| | F606W | F606W−F850LP | 4.084 ± 0.084 | −0.044 ± 0.034 | 0.000 ± 0.000 | 4.178 ± 0.012 | 0.029 ± 0.013 | 0.016 ± 0.003 | … |
| F625W ..... | F675W | F439W−F675W | | | | 4.553 ± 0.038 | −0.144 ± 0.053 | 0.011 ± 0.016 | <2.6 |
| | | | | | | 3.567 ± 0.268 | 0.499 ± 0.161 | −0.092 ± 0.024 | >2.6 |
| | F675W | F555W−F675W | | | | 4.280 ± 0.008 | −0.243 ± 0.063 | 0.023 ± 0.096 | <0.1 |
| | | | | | | 4.257 ± 0.022 | −0.030 ± 0.130 | −0.365 ± 0.163 | >0.1 |
| | F675W | F606W−F675W | | | | 4.015 ± 0.068 | −0.457 ± 0.211 | 0.011 ± 0.156 | <−0.4 |
| | | | | | | 3.884 ± 0.010 | −0.778 ± 0.029 | 0.093 ± 0.113 | >−0.4 |
| | F675W | F675W−F814W | | | | 4.194 ± 0.025 | −0.664 ± 0.176 | −0.330 ± 0.272 | <−0.1 |
| | | | | | | 4.225 ± 0.005 | −0.327 ± 0.050 | 0.011 ± 0.069 | >−0.1 |
| | F675W | F675W−F850LP | | | | 2.638 ± 0.681 | −1.464 ± 0.665 | −0.294 ± 0.161 | <−1.7 |
| | | | | | | 3.950 ± 0.226 | −0.159 ± 0.321 | 0.022 ± 0.113 | >−1.7 |
| F775W ..... | F814W | F439W−F814W | 4.367 ± 0.047 | −0.030 ± 0.020 | 0.000 ± 0.000 | 4.369 ± 0.019 | −0.075 ± 0.048 | 0.022 ± 0.026 | <1.9 |
| | | | | | | 4.337 ± 0.086 | −0.012 ± 0.058 | −0.004 ± 0.009 | >1.9 |
| | F814W | F555W−F814W | 4.297 ± 0.019 | −0.064 ± 0.038 | 0.000 ± 0.000 | 4.323 ± 0.098 | 0.069 ± 0.232 | 0.080 ± 0.130 | <−0.5 |
| | | | | | | 4.280 ± 0.005 | −0.069 ± 0.018 | −0.006 ± 0.032 | >−0.5 |
| | F814W | F606W−F814W | 4.260 ± 0.110 | −0.093 ± 0.170 | 0.000 ± 0.000 | 4.408 ± 0.313 | 0.233 ± 0.520 | 0.134 ± 0.213 | <−0.9 |
| | | | | | | 4.217 ± 0.007 | −0.104 ± 0.009 | −0.003 ± 0.015 | >−0.9 |
| | F814W | F675W−F814W | 4.309 ± 0.036 | −0.116 ± 0.309 | 0.000 ± 0.000 | 4.311 ± 0.082 | 0.105 ± 0.452 | 0.359 ± 0.591 | <−0.2 |
| | | | | | | 4.265 ± 0.004 | −0.173 ± 0.032 | 0.021 ± 0.038 | >−0.2 |
| | F814W | F814W−F850LP | | | | 3.486 ± 0.162 | −0.761 ± 0.224 | −0.154 ± 0.077 | <−0.2 |
| F814W ..... | F814W | F439W−F814W | 4.602 ± 0.035 | −0.001 ± 0.015 | 0.000 ± 0.000 | 4.569 ± 0.006 | 0.008 ± 0.008 | −0.000 ± 0.002 | <3.5 |
| | | | | | | 4.600 ± 0.133 | −0.013 ± 0.057 | 0.003 ± 0.006 | >3.5 |
| | F814W | F555W−F814W | 4.601 ± 0.016 | −0.001 ± 0.032 | 0.000 ± 0.000 | 4.587 ± 0.002 | 0.015 ± 0.004 | 0.001 ± 0.005 | … |
| | F814W | F606W−F814W | 4.623 ± 0.105 | 0.004 ± 0.160 | 0.000 ± 0.000 | 4.601 ± 0.002 | 0.023 ± 0.004 | 0.002 ± 0.003 | … |
| | F814W | F675W−F814W | 4.622 ± 0.032 | 0.012 ± 0.264 | 0.000 ± 0.000 | 4.590 ± 0.002 | 0.037 ± 0.005 | −0.003 ± 0.009 | … |
| | F814W | F814W−F850LP | | | | 4.765 ± 0.075 | 0.169 ± 0.104 | 0.034 ± 0.036 | <−1.0 |
| | | | | | | 4.663 ± 0.049 | 0.001 ± 0.163 | −0.036 ± 0.123 | >−1.0 |
| F850LP ..... | F850LP | F439W−F850LP | | | | 5.082 ± 0.018 | 0.015 ± 0.047 | 0.014 ± 0.026 | <0.0 |
| | | | | | | 5.082 ± 0.011 | −0.004 ± 0.010 | −0.001 ± 0.002 | >0.0 |
| | F850LP | F555W−F850LP | | | | 5.283 ± 0.451 | 0.174 ± 0.355 | 0.037 ± 0.069 | <−2.0 |
| | | | | | | 5.060 ± 0.007 | −0.011 ± 0.004 | 0.000 ± 0.002 | >−2.0 |
| | F850LP | F606W−F850LP | | | | 5.488 ± 0.931 | 0.299 ± 0.639 | 0.054 ± 0.109 | <−2.5 |
| | | | | | | 5.049 ± 0.011 | −0.012 ± 0.017 | 0.000 ± 0.007 | >−2.5 |
| | F850LP | F675W−F850LP | | | | 5.471 ± 0.908 | 0.402 ± 0.875 | 0.103 ± 0.210 | <−1.8 |
| | | | | | | 5.048 ± 0.010 | −0.019 ± 0.015 | −0.001 ± 0.010 | >−1.8 |
| | F850LP | F814W−F850LP | | | | 5.655 ± 1.632 | 0.738 ± 1.968 | 0.236 ± 0.592 | <−1.5 |
| | | | | | | 5.013 ± 0.055 | −0.019 ± 0.109 | 0.015 ± 0.052 | >−1.5 |

[a] TCOL range applies only to synthetic transformations.

TABLE 25
COEFFICIENTS FOR THE TRANSFORMATION FROM HRC TO WFPC2

| SOURCE | TARGET | | OBSERVED | | | SYNTHETIC | | | |
|---|---|---|---|---|---|---|---|---|---|
| SMAG | TMAG | TCOL | c0 | c1 | c2 | c0 | c1 | c2 | TCOL Range |
| F330W ..... | F336W | F336W−F439W | | | | 4.214 ± 0.018 | 0.004 ± 0.083 | 0.001 ± 0.104 | <1.1 |
| | | | | | | 4.056 ± 0.097 | 0.229 ± 0.100 | −0.077 ± 0.024 | >1.1 |
| | F336W | F336W−F555W | 5.820 ± 6.690 | −0.868 ± 3.329 | 0.118 ± 0.412 | 4.203 ± 0.142 | 0.011 ± 0.139 | −0.002 ± 0.032 | <3.1 |
| | | | | | | 3.745 ± 0.192 | 0.255 ± 0.089 | −0.034 ± 0.010 | >3.1 |
| | F336W | F336W−F606W | | | | 4.206 ± 0.160 | 0.006 ± 0.134 | −0.001 ± 0.026 | <3.6 |
| | | | | | | 3.832 ± 0.345 | 0.186 ± 0.148 | −0.022 ± 0.015 | >3.6 |
| | F336W | F336W−F675W | | | | 4.217 ± 0.148 | −0.002 ± 0.146 | 0.001 ± 0.033 | <3.1 |
| | | | | | | 3.946 ± 0.200 | 0.153 ± 0.093 | −0.021 ± 0.010 | >3.1 |
| | F336W | F336W−F814W | | | | 4.232 ± 0.125 | −0.017 ± 0.115 | 0.005 ± 0.025 | <3.3 |
| | | | | | | 3.940 ± 0.295 | 0.155 ± 0.131 | −0.021 ± 0.014 | >3.3 |
| | F336W | F336W−F850LP | | | | 4.188 ± 0.158 | 0.044 ± 0.185 | −0.012 ± 0.051 | <2.6 |
| | | | | | | 3.962 ± 0.185 | 0.183 ± 0.090 | −0.033 ± 0.011 | >2.6 |
| F435W ..... | F439W | F336W−F439W | | | | 5.718 ± 1.408 | −0.946 ± 1.995 | 0.324 ± 0.704 | <1.6 |
| | | | | | | 4.945 ± 0.200 | 0.052 ± 0.175 | 0.005 ± 0.038 | >1.6 |
| | F439W | F439W−F555W | 4.943 ± 0.100 | 0.039 ± 0.042 | 0.000 ± 0.000 | 5.265 ± 3.528 | −0.099 ± 4.717 | −0.033 ± 1.572 | <1.6 |
| | | | | | | 5.060 ± 0.132 | −0.077 ± 0.106 | 0.031 ± 0.021 | >1.6 |
| | F439W | F439W−F606W | | | | 5.273 ± 2.769 | −0.107 ± 3.074 | −0.011 ± 0.850 | <2.0 |
| | | | | | | 5.042 ± 0.122 | −0.048 ± 0.078 | 0.017 ± 0.012 | >2.0 |
| | F439W | F439W−F675W | | | | 5.140 ± 0.390 | −0.104 ± 0.871 | −0.004 ± 0.474 | <1.2 |
| | | | | | | 5.010 ± 0.050 | −0.010 ± 0.038 | 0.011 ± 0.007 | >1.2 |
| | F439W | F439W−F814W | 5.011 ± 0.103 | 0.018 ± 0.094 | −0.002 ± 0.020 | 5.088 ± 0.038 | −0.140 ± 0.150 | 0.067 ± 0.126 | <1.1 |
| | | | | | | 5.014 ± 0.054 | −0.003 ± 0.042 | 0.009 ± 0.008 | >1.1 |
| | F439W | F439W−F850LP | | | | 4.943 ± 0.341 | −0.088 ± 0.531 | −0.008 ± 0.201 | <−0.9 |
| | | | | | | 5.033 ± 0.007 | 0.030 ± 0.009 | 0.002 ± 0.003 | >−0.9 |
| F555W ..... | F555W | F336W−F555W | | | | 3.430 ± 0.035 | 0.011 ± 0.018 | −0.004 ± 0.002 | ... |
| | F555W | F439W−F555W | 3.565 ± 0.130 | −0.067 ± 0.054 | 0.000 ± 0.000 | 3.410 ± 0.068 | 0.045 ± 0.058 | −0.020 ± 0.012 | ... |
| | F555W | F555W−F606W | | | | 3.421 ± 0.034 | 0.118 ± 0.112 | −0.257 ± 0.087 | ... |
| | F555W | F555W−F675W | | | | 3.404 ± 0.006 | −0.091 ± 0.011 | −0.070 ± 0.019 | ... |
| | F555W | F555W−F814W | 3.406 ± 0.022 | −0.070 ± 0.046 | 0.000 ± 0.000 | 3.395 ± 0.007 | −0.065 ± 0.011 | −0.027 ± 0.015 | ... |
| | F555W | F555W−F850LP | | | | 3.291 ± 0.190 | −0.093 ± 0.170 | −0.015 ± 0.037 | <−1.5 |
| | | | | | | 3.314 ± 0.013 | −0.026 ± 0.013 | 0.021 ± 0.014 | >−1.5 |
| F606W ..... | F606W | F336W−F606W | | | | 3.718 ± 0.081 | 0.033 ± 0.062 | −0.009 ± 0.011 | <4.0 |
| | | | | | | 3.826 ± 0.133 | −0.045 ± 0.047 | 0.003 ± 0.004 | >4.0 |
| | F606W | F439W−F606W | | | | 3.895 ± 0.041 | −0.106 ± 0.028 | 0.011 ± 0.004 | ... |
| | F606W | F555W−F606W | | | | 3.846 ± 0.019 | −0.406 ± 0.058 | 0.196 ± 0.040 | ... |
| | F606W | F606W−F675W | | | | 3.580 ± 0.141 | −0.169 ± 0.399 | 0.011 ± 0.274 | <−0.5 |
| | | | | | | 3.638 ± 0.009 | 0.045 ± 0.023 | 0.184 ± 0.067 | >−0.5 |
| | F606W | F606W−F814W | | | | 3.605 ± 0.215 | −0.115 ± 0.371 | −0.011 ± 0.157 | <−0.8 |
| | | | | | | 3.633 ± 0.007 | −0.032 ± 0.009 | 0.045 ± 0.010 | >−0.8 |
| | F606W | F606W−F850LP | | | | 3.383 ± 0.343 | −0.175 ± 0.253 | −0.019 ± 0.046 | <−2.2 |
| | | | | | | 3.643 ± 0.011 | 0.032 ± 0.020 | 0.021 ± 0.010 | >−2.2 |
| F625W ..... | F675W | F336W−F675W | | | | 3.661 ± 0.132 | 0.227 ± 0.104 | −0.057 ± 0.020 | <3.6 |
| | | | | | | 3.705 ± 0.135 | 0.037 ± 0.052 | −0.008 ± 0.005 | >3.6 |
| | F675W | F439W−F675W | | | | 4.022 ± 0.041 | −0.148 ± 0.057 | 0.011 ± 0.018 | <2.6 |
| | | | | | | 3.394 ± 0.297 | 0.266 ± 0.179 | −0.056 ± 0.027 | >2.6 |
| | F675W | F555W−F675W | | | | 3.741 ± 0.005 | −0.261 ± 0.010 | −0.002 ± 0.025 | ... |
| | F675W | F606W−F675W | | | | 3.417 ± 0.029 | −0.617 ± 0.102 | −0.090 ± 0.083 | ... |
| | F675W | F675W−F814W | | | | 3.645 ± 0.082 | −0.729 ± 0.452 | −0.401 ± 0.591 | <−0.2 |
| | | | | | | 3.682 ± 0.006 | −0.381 ± 0.040 | 0.156 ± 0.248 | >−0.2 |
| | F675W | F675W−F850LP | | | | 2.087 ± 0.557 | −1.470 ± 0.554 | −0.294 ± 0.136 | <−1.7 |
| | | | | | | 3.445 ± 0.055 | −0.083 ± 0.096 | 0.055 ± 0.041 | >−1.7 |
| F775W ..... | F814W | F336W−F814W | | | | 3.655 ± 0.012 | −0.018 ± 0.007 | −0.001 ± 0.001 | ... |
| | F814W | F439W−F814W | | | | 3.665 ± 0.018 | −0.071 ± 0.039 | 0.017 ± 0.018 | <2.0 |
| | | | | | | 3.565 ± 0.046 | 0.032 ± 0.025 | −0.012 ± 0.003 | >2.0 |
| | F814W | F555W−F814W | | | | 3.609 ± 0.098 | 0.057 ± 0.232 | 0.078 ± 0.130 | <−0.5 |
| | | | | | | 3.568 ± 0.005 | −0.076 ± 0.018 | −0.007 ± 0.032 | >−0.5 |

TABLE 25 (*Continued*)

| Source | Target | | Observed | | | Synthetic | | | |
|---|---|---|---|---|---|---|---|---|---|
| SMAG | TMAG | TCOL | c0 | c1 | c2 | c0 | c1 | c2 | TCOL Range |
| | F814W | F606W−F814W | | | | 3.682 ± 0.313 | 0.210 ± 0.520 | 0.130 ± 0.213 | <−0.9 |
| | | | | | | 3.498 ± 0.007 | −0.116 ± 0.009 | −0.005 ± 0.015 | >−0.9 |
| | F814W | F675W−F814W | | | | 3.594 ± 0.082 | 0.064 ± 0.452 | 0.332 ± 0.591 | <−0.2 |
| | | | | | | 3.551 ± 0.004 | −0.192 ± 0.032 | 0.021 ± 0.038 | >−0.2 |
| | F814W | F814W−F850LP | | | | 2.638 ± 0.070 | −0.906 ± 0.106 | −0.191 ± 0.040 | … |
| F814W ..... | F814W | F336W−F814W | | | | 3.911 ± 0.010 | 0.006 ± 0.008 | 0.000 ± 0.002 | <5.0 |
| | | | | | | 4.221 ± 0.135 | −0.100 ± 0.040 | 0.009 ± 0.003 | >5.0 |
| | F814W | F439W−F814W | 3.928 ± 0.054 | 0.003 ± 0.021 | 0.000 ± 0.000 | 3.912 ± 0.009 | 0.012 ± 0.011 | −0.001 ± 0.003 | <3.5 |
| | | | | | | 4.095 ± 0.199 | −0.083 ± 0.086 | 0.012 ± 0.009 | >3.5 |
| | F814W | F555W−F814W | 3.937 ± 0.012 | 0.010 ± 0.031 | 0.000 ± 0.000 | 3.940 ± 0.003 | 0.023 ± 0.006 | 0.002 ± 0.007 | … |
| | F814W | F606W−F814W | | | | 3.962 ± 0.004 | 0.037 ± 0.005 | 0.004 ± 0.005 | … |
| | F814W | F675W−F814W | | | | 3.945 ± 0.003 | 0.060 ± 0.008 | −0.002 ± 0.013 | … |
| | F814W | F814W−F850LP | | | | 4.243 ± 0.113 | 0.295 ± 0.156 | 0.062 ± 0.054 | <−1.0 |
| | | | | | | 4.183 ± 0.074 | 0.177 ± 0.245 | 0.001 ± 0.185 | >−1.0 |
| F850LP ..... | F850LPW | F336W−F850LP | | | | 4.599 ± 0.019 | −0.000 ± 0.043 | 0.001 ± 0.021 | <0.0 |
| | | | | | | 4.603 ± 0.008 | 0.001 ± 0.004 | 0.000 ± 0.001 | >0.0 |
| | F850LP | F439W−F850LP | | | | 4.608 ± 0.013 | 0.016 ± 0.032 | 0.008 ± 0.018 | <0.0 |
| | | | | | | 4.608 ± 0.007 | −0.003 ± 0.007 | 0.001 ± 0.001 | >0.0 |
| | F850LP | F555W−F850LP | | | | 4.763 ± 0.315 | 0.124 ± 0.247 | 0.023 ± 0.048 | <−2.0 |
| | | | | | | 4.606 ± 0.005 | 0.003 ± 0.003 | 0.002 ± 0.001 | >−2.0 |
| | F850LP | F606W−F850LP | | | | 4.931 ± 0.649 | 0.222 ± 0.446 | 0.037 ± 0.076 | <−2.5 |
| | | | | | | 4.609 ± 0.008 | 0.004 ± 0.012 | 0.001 ± 0.005 | >−2.5 |
| | F850LP | F675W−F850LP | | | | 4.945 ± 0.633 | 0.323 ± 0.611 | 0.076 ± 0.146 | <−1.8 |
| | | | | | | 4.609 ± 0.007 | 0.006 ± 0.011 | 0.002 ± 0.007 | >−1.8 |
| | F850LP | F814W−F850LP | | | | 5.034 ± 1.139 | 0.497 ± 1.373 | 0.143 ± 0.413 | <−1.5 |
| | | | | | | 4.683 ± 0.038 | 0.117 ± 0.076 | 0.044 ± 0.036 | >−1.5 |

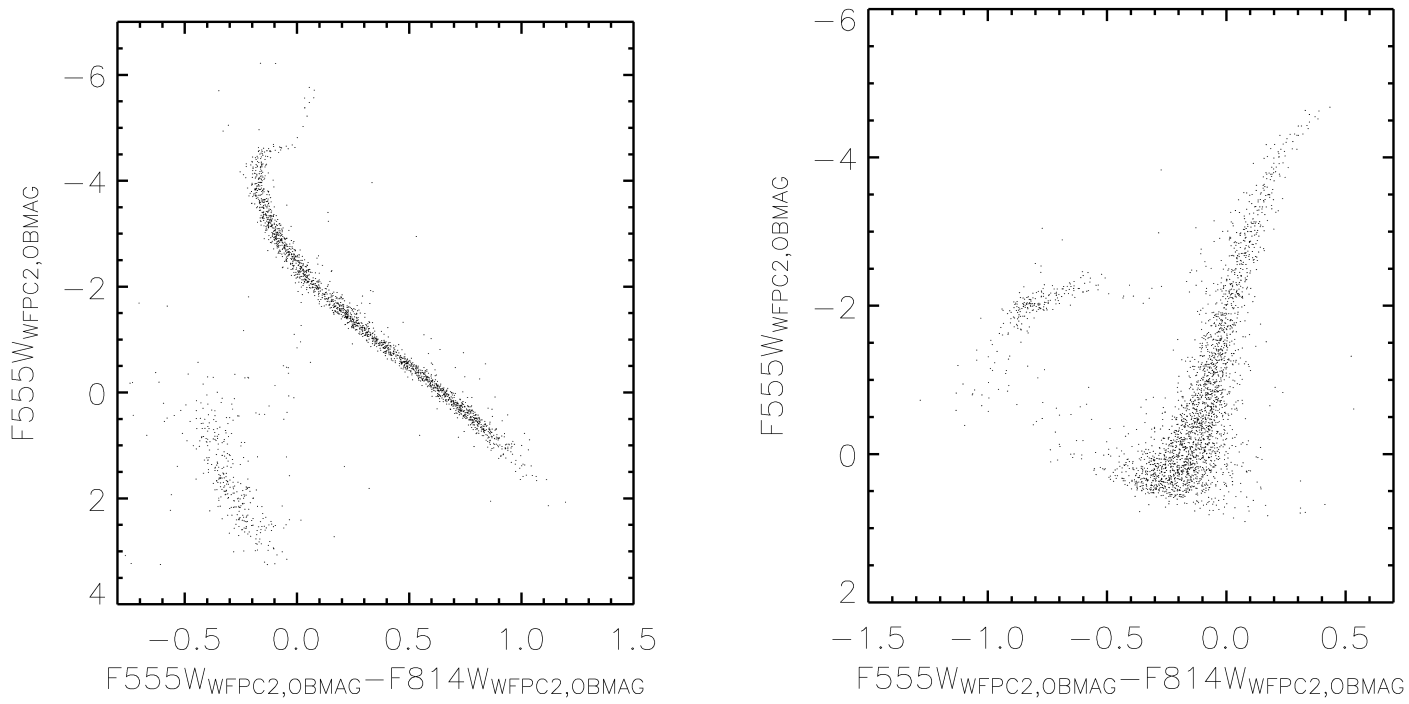


FIG. 25.—Observed WFPC2 CMDs for NGC 104 (*left*) and NGC 2419 (*right*).

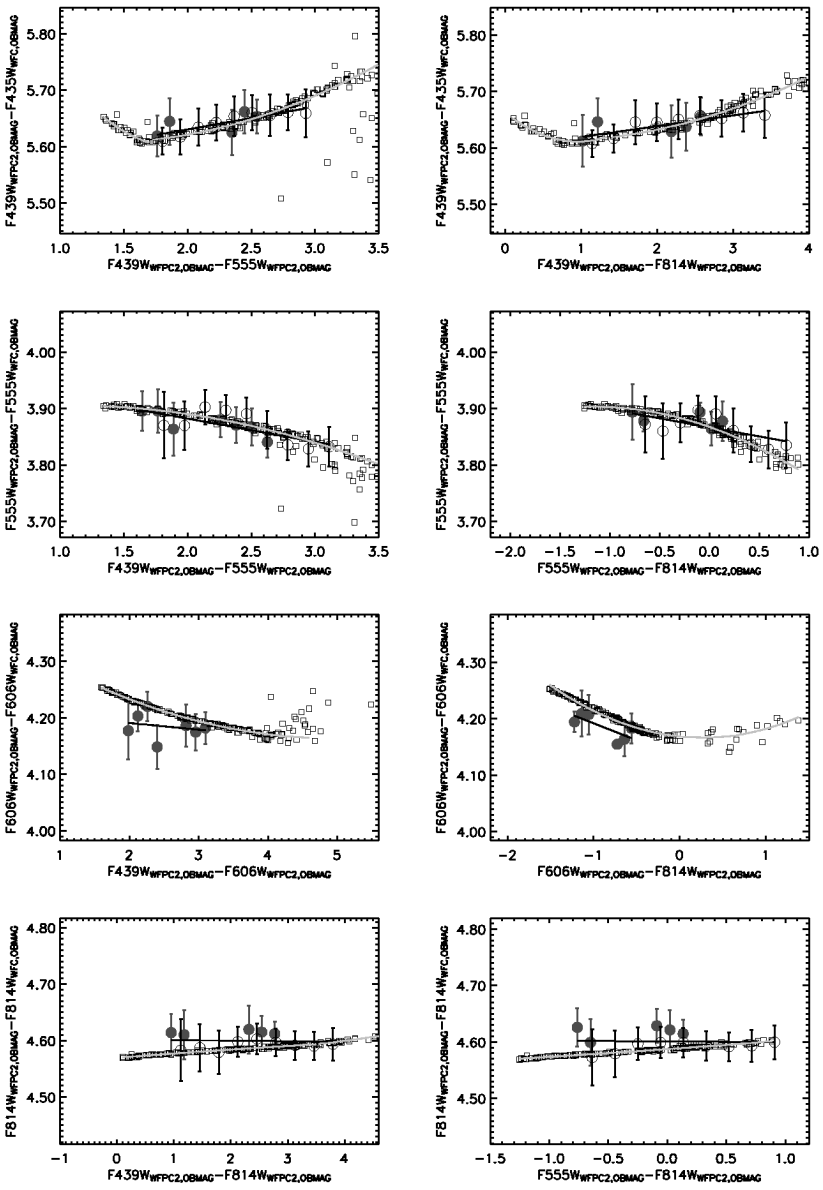


FIG. 26.—Observed and synthetic WFC-to-WFPC2 transformations for primary photometric filters. Squares show the synthetic measurements for the BPGS atlas. The circles are observational data (*filled*, NGC 104; *open*, NGC 2419). The black line shows the linear fit to the observational points; the light curve shows the synthetic transformations. [*See the electronic edition of the PASP for a color version of this figure*.]

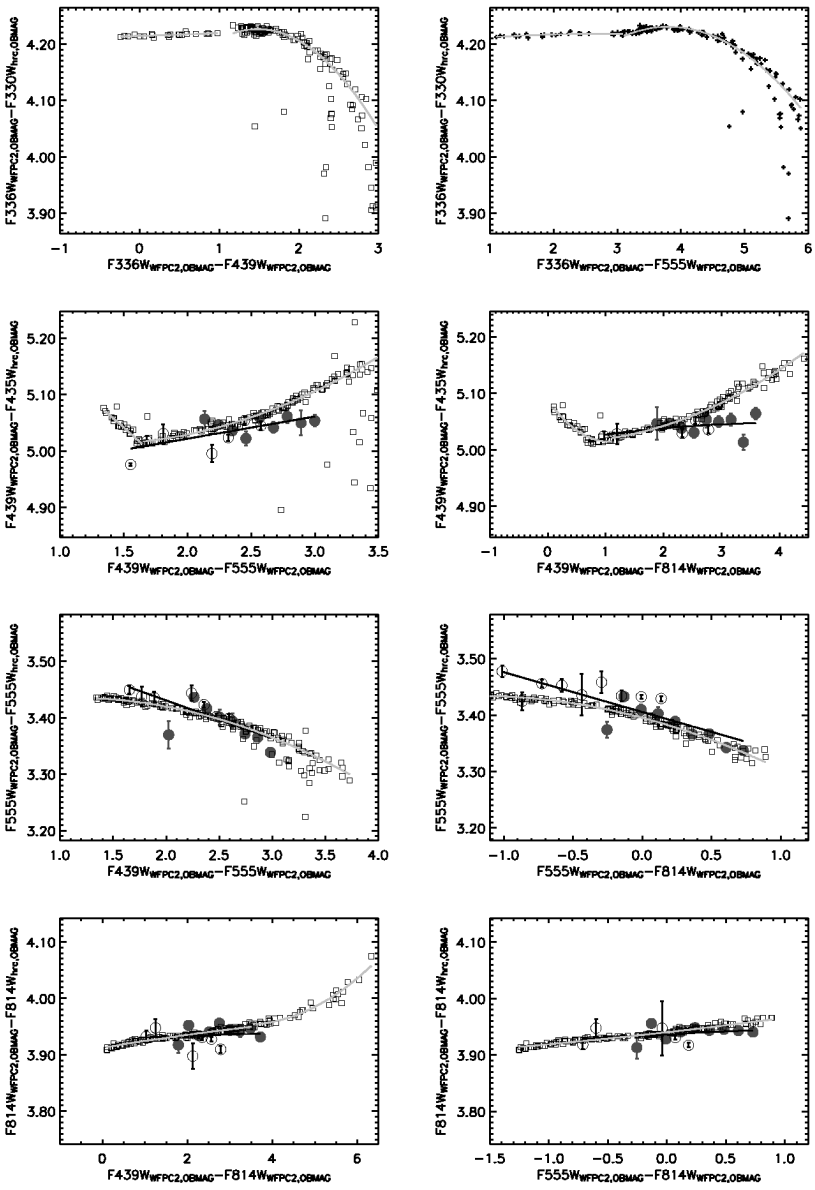


FIG. 27.—Observed and synthetic HRC-to-WFPC2 transformations for primary photometric filters. Squares show the synthetic measurements for the BPGS atlas. The circles are observational data (*filled*, NGC 104; *open*, NGC 2419). The black line shows the linear fit to the observational points; the light curve shows the synthetic transformations. [*See the electronic edition of PASP for a color version of this figure.*]

## APPENDIX E

## TRANSFORMATION OF GALAXY TEMPLATES

The color transformations described in the previous sections cannot offer accurate results for all spectral shapes, especially when the effects of redshift and intergalactic absorption are taken into account. Therefore, it is desirable to describe the colors of observed galaxies at different redshifts in the different systems as accurately as possible. To do so, we use a variation of the CWWSB template library, introduced in Benítez (2000) and formed by the main types (E/SO, Sbc, Scd, and Im) from Coleman et al. (1980) and two starbursts (SB2 and SB3) of Kinney et al. (1996). Benítez et al. (2004, hereafter B2004)

presented a variant of this library, which has been calibrated using spectroscopic redshift catalogs with good quality photometry. By definition, the new templates agree much better with the observed colors of real galaxies, and for instance reduce the photometric redshift scatter by a factor of 25% in the HDF-N, although they have not been optimized for that goal.

We generate estimated colors for the B2004 library in intervals of 0.05 in redshift, using the ACS WFC F606W filter as reference, for the WFC, HRC, WFPC2, and Johnson-Cousins systems. We apply corrections for intergalactic hydrogen extinction using the prescriptions of Madau (1995). All colors, except the Johnson-Cousins ones, correspond to the AB system. The colors were calculated using the functions included in the module `bpz_tools` from the BPZ package (Benítez 2000),[27] which offers accuracy similar to that of SYNPHOT. The Vega reference spectrum is that of Bohlin & Gilliland (2004).

We present here only the tables for the E/S0, Sbc, and Im templates for the WFC and Johnsons-Cousins system. Tables for other templates are available online.[28]

Tables 26–34 must be used with caution, however, because obviously these six "atomic" spectral templates cannot represent all the possible variations of real galaxy spectra except for some limited populations. Moreover, the colors at given redshifts obtained here are evaluated without the consideration of the spectral evolution, which omission may introduce significant systematics, particularly at high redshifts. Nevertheless, despite all these limitations, one can still use these tables as a guide to transform galaxy colors between different photometric systems for a given spectral type and redshift. To this end, we need to find the closest possible match in redshift and spectral type in the electronic tables, using as many colors as possible. Then we look up the corresponding color in the table corresponding to the spectral type and filter of interest, using interpolation between spectral types and redshifts if needed.

For example, let us suppose we have ACS/WFC photometry of an elliptical galaxy at redshift $z = 1$ with ACS/WFC ABMAG F606W − F814W = 1.82. If we want to know the F606W − F814W color in the HRC ABMAG system, from Table 29 we can read multi-instrument colors for $z = 1$ of $\mathrm{HRC}_{\mathrm{F606W}} - \mathrm{WFC}_{\mathrm{F606W}} = 0.04$ and $\mathrm{HRC}_{\mathrm{F814W}} - \mathrm{WFC}_{\mathrm{F606W}} = -1.87$.

Therefore, we can directly calculate the ACS/HRC ABMAG color for this galaxy: F606W–F814W = 1.91. Moreover, if we need to compare the ACS observations with ground-based observations, for example in the $R - I$ color, from Table 32 we derive for $z = 1$ $R - \mathrm{WFC}_{\mathrm{F606W}} = -0.59$ and $I - \mathrm{WFC}_{\mathrm{F606W}} = -1.59$, and therefore $R - I = 1.00$.

[27] See http://acs.pha.jhu.edu/~txitxo/bayesian.html.

[28] See http://acs.pha.jhu.edu/instrument/photometry.

TABLE 26
AB Colors of the E/So Template from Benítez et al. (2004) in the WFC Filter System

| $z$ | F435W−F606W | F475W−F606W | F555W−F606W | F625W−F606W | F775W−F606W | F814W−F606W | F850LP−F606W |
|---|---|---|---|---|---|---|---|
| 0.01 ..... | 1.06 | 0.63 | 0.24 | −0.16 | −0.52 | −0.58 | −0.74 |
| 0.06 ..... | 1.26 | 0.72 | 0.25 | −0.16 | −0.56 | −0.63 | −0.79 |
| 0.11 ..... | 1.46 | 0.80 | 0.27 | −0.17 | −0.61 | −0.68 | −0.86 |
| 0.16 ..... | 1.60 | 0.93 | 0.30 | −0.19 | −0.65 | −0.73 | −0.93 |
| 0.21 ..... | 1.76 | 1.06 | 0.34 | −0.23 | −0.71 | −0.80 | −1.01 |
| 0.26 ..... | 1.75 | 1.17 | 0.42 | −0.26 | −0.77 | −0.87 | −1.10 |
| 0.31 ..... | 1.79 | 1.25 | 0.52 | −0.29 | −0.84 | −0.94 | −1.19 |
| 0.36 ..... | 1.83 | 1.34 | 0.62 | −0.32 | −0.91 | −1.01 | −1.28 |
| 0.41 ..... | 1.90 | 1.39 | 0.70 | −0.33 | −0.96 | −1.07 | −1.36 |
| 0.46 ..... | 1.99 | 1.36 | 0.74 | −0.32 | −1.05 | −1.16 | −1.46 |
| 0.51 ..... | 2.10 | 1.37 | 0.74 | −0.30 | −1.16 | −1.28 | −1.58 |
| 0.56 ..... | 2.19 | 1.36 | 0.69 | −0.28 | −1.28 | −1.41 | −1.72 |
| 0.61 ..... | 2.28 | 1.36 | 0.62 | −0.27 | −1.39 | −1.52 | −1.84 |
| 0.66 ..... | 2.40 | 1.41 | 0.59 | −0.27 | −1.47 | −1.61 | −1.95 |
| 0.71 ..... | 2.50 | 1.48 | 0.58 | −0.27 | −1.53 | −1.69 | −2.06 |
| 0.76 ..... | 2.54 | 1.55 | 0.56 | −0.27 | −1.59 | −1.78 | −2.20 |
| 0.81 ..... | 2.57 | 1.61 | 0.60 | −0.32 | −1.59 | −1.82 | −2.30 |
| 0.86 ..... | 2.60 | 1.74 | 0.71 | −0.35 | −1.51 | −1.80 | −2.35 |
| 0.91 ..... | 2.57 | 1.84 | 0.82 | −0.35 | −1.46 | −1.80 | −2.40 |
| 0.96 ..... | 2.50 | 1.89 | 0.90 | −0.38 | −1.45 | −1.82 | −2.46 |
| 1.01 ..... | 2.44 | 1.94 | 0.98 | −0.39 | −1.44 | −1.82 | −2.50 |

TABLE 27
AB Colors of the Sbc Template from Benítez et al. (2004) in the WFC Filter System

| $z$ | F435W−F606W | F475W−F606W | F555W−F606W | F625W−F606W | F775W−F606W | F814W−F606W | F850LP−F606W |
|---|---|---|---|---|---|---|---|
| 0.01 ..... | 0.75 | 0.47 | 0.18 | −0.13 | −0.42 | −0.48 | −0.64 |
| 0.06 ..... | 0.86 | 0.52 | 0.19 | −0.13 | −0.45 | −0.51 | −0.66 |
| 0.11 ..... | 0.98 | 0.57 | 0.21 | −0.14 | −0.48 | −0.54 | −0.70 |
| 0.16 ..... | 1.11 | 0.65 | 0.22 | −0.15 | −0.51 | −0.58 | −0.74 |
| 0.21 ..... | 1.26 | 0.74 | 0.24 | −0.16 | −0.54 | −0.61 | −0.79 |
| 0.26 ..... | 1.38 | 0.82 | 0.27 | −0.18 | −0.58 | −0.66 | −0.85 |
| 0.31 ..... | 1.48 | 0.90 | 0.31 | −0.21 | −0.63 | −0.71 | −0.91 |
| 0.36 ..... | 1.54 | 1.00 | 0.37 | −0.23 | −0.67 | −0.75 | −0.96 |
| 0.41 ..... | 1.58 | 1.08 | 0.43 | −0.26 | −0.72 | −0.80 | −1.03 |
| 0.46 ..... | 1.58 | 1.12 | 0.49 | −0.27 | −0.78 | −0.87 | −1.10 |
| 0.51 ..... | 1.54 | 1.14 | 0.54 | −0.28 | −0.85 | −0.94 | −1.19 |
| 0.56 ..... | 1.47 | 1.13 | 0.58 | −0.29 | −0.93 | −1.03 | −1.27 |
| 0.61 ..... | 1.39 | 1.11 | 0.60 | −0.29 | −1.01 | −1.11 | −1.36 |
| 0.66 ..... | 1.30 | 1.07 | 0.61 | −0.29 | −1.08 | −1.18 | −1.44 |
| 0.71 ..... | 1.20 | 0.99 | 0.60 | −0.28 | −1.15 | −1.26 | −1.54 |
| 0.76 ..... | 1.10 | 0.91 | 0.57 | −0.25 | −1.22 | −1.34 | −1.63 |
| 0.81 ..... | 1.00 | 0.82 | 0.53 | −0.24 | −1.26 | −1.40 | −1.72 |
| 0.86 ..... | 0.91 | 0.74 | 0.48 | −0.22 | −1.28 | −1.44 | −1.80 |
| 0.91 ..... | 0.83 | 0.67 | 0.42 | −0.20 | −1.28 | −1.47 | −1.86 |
| 0.96 ..... | 0.76 | 0.60 | 0.38 | −0.19 | −1.27 | −1.47 | −1.90 |
| 1.01 ..... | 0.70 | 0.55 | 0.33 | −0.16 | −1.24 | −1.46 | −1.93 |

TABLE 28
AB Colors of the Im Template from Benítez et al. (2004) in the WFC Filter System

| $z$ | F435W−F606W | F475W−F606W | F555W−F606W | F625W−F606W | F775W−F606W | F814W−F606W | F850LP−F606W |
|---|---|---|---|---|---|---|---|
| 0.01 ..... | 0.36 | 0.19 | 0.06 | −0.04 | −0.20 | −0.23 | −0.31 |
| 0.06 ..... | 0.42 | 0.21 | 0.05 | −0.03 | −0.21 | −0.24 | −0.32 |
| 0.11 ..... | 0.50 | 0.28 | 0.05 | −0.04 | −0.22 | −0.25 | −0.33 |
| 0.16 ..... | 0.59 | 0.34 | 0.06 | −0.08 | −0.22 | −0.26 | −0.35 |
| 0.21 ..... | 0.68 | 0.40 | 0.10 | −0.10 | −0.23 | −0.27 | −0.36 |
| 0.26 ..... | 0.76 | 0.47 | 0.15 | −0.11 | −0.23 | −0.27 | −0.38 |
| 0.31 ..... | 0.87 | 0.52 | 0.18 | −0.13 | −0.24 | −0.28 | −0.40 |
| 0.36 ..... | 0.86 | 0.57 | 0.21 | −0.15 | −0.27 | −0.31 | −0.43 |
| 0.41 ..... | 0.84 | 0.60 | 0.24 | −0.14 | −0.35 | −0.37 | −0.47 |
| 0.46 ..... | 0.77 | 0.58 | 0.24 | −0.16 | −0.46 | −0.48 | −0.55 |
| 0.51 ..... | 0.72 | 0.60 | 0.27 | −0.20 | −0.52 | −0.54 | −0.59 |
| 0.56 ..... | 0.66 | 0.56 | 0.30 | −0.20 | −0.57 | −0.59 | −0.64 |
| 0.61 ..... | 0.60 | 0.52 | 0.32 | −0.19 | −0.62 | −0.64 | −0.69 |
| 0.66 ..... | 0.53 | 0.47 | 0.33 | −0.18 | −0.65 | −0.68 | −0.77 |
| 0.71 ..... | 0.47 | 0.42 | 0.30 | −0.17 | −0.66 | −0.72 | −0.87 |
| 0.76 ..... | 0.40 | 0.36 | 0.26 | −0.14 | −0.66 | −0.75 | −0.93 |
| 0.81 ..... | 0.34 | 0.31 | 0.23 | −0.12 | −0.68 | −0.78 | −0.97 |
| 0.86 ..... | 0.28 | 0.25 | 0.19 | −0.10 | −0.70 | −0.79 | −1.00 |
| 0.91 ..... | 0.22 | 0.19 | 0.13 | −0.06 | −0.72 | −0.82 | −1.03 |
| 0.96 ..... | 0.18 | 0.15 | 0.10 | −0.07 | −0.70 | −0.80 | −1.03 |
| 1.01 ..... | 0.16 | 0.13 | 0.09 | −0.05 | −0.64 | −0.75 | −1.02 |

TABLE 29

MULTI-INSTRUMENT COLORS OF THE E/So TEMPLATE FROM BENÍTEZ ET AL. (2004) IN THE HRC SYSTEM (AB MAG) AND WFC F606W (AB MAG)

| $z$ | $H_{F220W}-W_{F606W}$ | $H_{F250W}-W_{F606W}$ | $H_{F330W}-W_{F606W}$ | $H_{F435W}-W_{F606W}$ | $H_{F475W}-W_{F606W}$ | $H_{F555W}-W_{F606W}$ | $H_{F606W}-W_{F606W}$ | $H_{F625W}-W_{F606W}$ | $H_{F775W}-W_{F606W}$ | $H_{F814W}-W_{F606W}$ | $H_{F850LP}-W_{F606W}$ |
|---|---|---|---|---|---|---|---|---|---|---|---|
| 0.01 ..... | 5.42 | 4.08 | 2.54 | 1.06 | 0.61 | 0.24 | 0.01 | −0.15 | −0.51 | −0.59 | −0.76 |
| 0.06 ..... | 5.53 | 4.39 | 2.69 | 1.26 | 0.69 | 0.25 | 0.01 | −0.16 | −0.56 | −0.64 | −0.80 |
| 0.11 ..... | 5.61 | 4.64 | 2.88 | 1.45 | 0.77 | 0.27 | 0.01 | −0.16 | −0.60 | −0.68 | −0.87 |
| 0.16 ..... | 5.67 | 4.82 | 3.14 | 1.59 | 0.89 | 0.31 | 0.02 | −0.18 | −0.64 | −0.74 | −0.95 |
| 0.21 ..... | 5.70 | 4.92 | 3.39 | 1.76 | 1.02 | 0.34 | 0.02 | −0.22 | −0.70 | −0.81 | −1.03 |
| 0.26 ..... | 5.69 | 4.98 | 3.66 | 1.76 | 1.14 | 0.43 | 0.02 | −0.26 | −0.76 | −0.88 | −1.12 |
| 0.31 ..... | 5.64 | 5.00 | 3.91 | 1.79 | 1.22 | 0.53 | 0.03 | −0.28 | −0.83 | −0.95 | −1.21 |
| 0.36 ..... | 5.55 | 5.00 | 4.09 | 1.83 | 1.31 | 0.63 | 0.03 | −0.31 | −0.90 | −1.03 | −1.30 |
| 0.41 ..... | 5.46 | 4.99 | 4.17 | 1.90 | 1.36 | 0.71 | 0.03 | −0.32 | −0.95 | −1.09 | −1.38 |
| 0.46 ..... | 5.33 | 4.95 | 4.14 | 1.98 | 1.33 | 0.75 | 0.03 | −0.30 | −1.04 | −1.18 | −1.48 |
| 0.51 ..... | 5.17 | 4.87 | 4.05 | 2.10 | 1.33 | 0.75 | 0.04 | −0.28 | −1.16 | −1.30 | −1.61 |
| 0.56 ..... | 5.00 | 4.75 | 3.95 | 2.19 | 1.32 | 0.69 | 0.03 | −0.26 | −1.28 | −1.43 | −1.74 |
| 0.61 ..... | 4.84 | 4.62 | 3.87 | 2.27 | 1.32 | 0.62 | 0.03 | −0.25 | −1.38 | −1.54 | −1.87 |
| 0.66 ..... | 4.69 | 4.48 | 3.82 | 2.38 | 1.36 | 0.60 | 0.03 | −0.26 | −1.45 | −1.63 | −1.98 |
| 0.71 ..... | 4.55 | 4.34 | 3.78 | 2.48 | 1.43 | 0.59 | 0.03 | −0.26 | −1.52 | −1.71 | −2.09 |
| 0.76 ..... | 4.41 | 4.17 | 3.72 | 2.53 | 1.50 | 0.57 | 0.03 | −0.26 | −1.58 | −1.80 | −2.22 |
| 0.81 ..... | 4.29 | 4.03 | 3.66 | 2.57 | 1.57 | 0.61 | 0.03 | −0.32 | −1.57 | −1.85 | −2.33 |
| 0.86 ..... | 4.23 | 3.94 | 3.64 | 2.60 | 1.70 | 0.72 | 0.03 | −0.34 | −1.49 | −1.83 | −2.38 |
| 0.91 ..... | 4.16 | 3.83 | 3.57 | 2.58 | 1.81 | 0.83 | 0.04 | −0.34 | −1.44 | −1.85 | −2.44 |
| 0.96 ..... | 4.06 | 3.70 | 3.46 | 2.51 | 1.87 | 0.91 | 0.04 | −0.36 | −1.43 | −1.87 | −2.51 |
| 1.01 ..... | 3.98 | 3.59 | 3.35 | 2.44 | 1.91 | 1.00 | 0.04 | −0.37 | −1.43 | −1.87 | −2.56 |

TABLE 30

MULTI-INSTRUMENT COLORS OF THE Sbc TEMPLATE FROM BENÍTEZ ET AL. (2004) IN THE HRC SYSTEM (AB MAG) AND WFC F606W (AB MAG)

| $z$ | $H_{F220W}-W_{F606W}$ | $H_{F250W}-W_{F606W}$ | $H_{F330W}-W_{F606W}$ | $H_{F435W}-W_{F606W}$ | $H_{F475W}-W_{F606W}$ | $H_{F555W}-W_{F606W}$ | $H_{F606W}-W_{F606W}$ | $H_{F625W}-W_{F606W}$ | $H_{F775W}-W_{F606W}$ | $H_{F814W}-W_{F606W}$ | $H_{F850LP}-W_{F606W}$ |
|---|---|---|---|---|---|---|---|---|---|---|---|
| 0.01 ..... | 3.12 | 2.78 | 2.05 | 0.75 | 0.46 | 0.19 | 0.01 | −0.12 | −0.42 | −0.48 | −0.65 |
| 0.06 ..... | 3.10 | 2.79 | 2.20 | 0.86 | 0.50 | 0.19 | 0.01 | −0.13 | −0.45 | −0.51 | −0.67 |
| 0.11 ..... | 3.08 | 2.78 | 2.31 | 0.98 | 0.55 | 0.21 | 0.01 | −0.13 | −0.48 | −0.55 | −0.71 |
| 0.16 ..... | 3.06 | 2.76 | 2.35 | 1.11 | 0.62 | 0.22 | 0.01 | −0.14 | −0.51 | −0.58 | −0.75 |
| 0.21 ..... | 3.05 | 2.73 | 2.35 | 1.26 | 0.71 | 0.24 | 0.01 | −0.16 | −0.54 | −0.62 | −0.80 |
| 0.26 ..... | 3.04 | 2.68 | 2.33 | 1.38 | 0.79 | 0.27 | 0.02 | −0.18 | −0.58 | −0.67 | −0.86 |
| 0.31 ..... | 3.03 | 2.63 | 2.28 | 1.47 | 0.87 | 0.32 | 0.02 | −0.20 | −0.63 | −0.72 | −0.93 |
| 0.36 ..... | 3.03 | 2.58 | 2.23 | 1.53 | 0.97 | 0.38 | 0.02 | −0.23 | −0.66 | −0.76 | −0.98 |
| 0.41 ..... | 3.02 | 2.52 | 2.17 | 1.58 | 1.05 | 0.44 | 0.02 | −0.25 | −0.71 | −0.82 | −1.05 |
| 0.46 ..... | 3.00 | 2.47 | 2.10 | 1.58 | 1.10 | 0.50 | 0.02 | −0.26 | −0.77 | −0.88 | −1.12 |
| 0.51 ..... | 2.98 | 2.41 | 2.01 | 1.54 | 1.12 | 0.55 | 0.03 | −0.27 | −0.84 | −0.96 | −1.21 |
| 0.56 ..... | 2.94 | 2.35 | 1.91 | 1.47 | 1.12 | 0.59 | 0.03 | −0.27 | −0.92 | −1.04 | −1.30 |
| 0.61 ..... | 2.90 | 2.28 | 1.80 | 1.39 | 1.09 | 0.61 | 0.03 | −0.28 | −1.00 | −1.13 | −1.38 |
| 0.66 ..... | 2.86 | 2.23 | 1.70 | 1.30 | 1.05 | 0.62 | 0.03 | −0.27 | −1.07 | −1.20 | −1.47 |
| 0.71 ..... | 2.81 | 2.17 | 1.59 | 1.20 | 0.98 | 0.60 | 0.03 | −0.26 | −1.14 | −1.28 | −1.56 |
| 0.76 ..... | 2.76 | 2.11 | 1.49 | 1.10 | 0.90 | 0.57 | 0.03 | −0.24 | −1.21 | −1.35 | −1.66 |
| 0.81 ..... | 2.72 | 2.06 | 1.40 | 1.00 | 0.81 | 0.53 | 0.03 | −0.23 | −1.25 | −1.42 | −1.75 |
| 0.86 ..... | 2.69 | 2.02 | 1.33 | 0.91 | 0.73 | 0.48 | 0.03 | −0.21 | −1.27 | −1.46 | −1.82 |
| 0.91 ..... | 2.67 | 1.99 | 1.28 | 0.83 | 0.66 | 0.43 | 0.02 | −0.19 | −1.27 | −1.49 | −1.89 |
| 0.96 ..... | 2.66 | 1.98 | 1.25 | 0.76 | 0.59 | 0.38 | 0.02 | −0.18 | −1.25 | −1.50 | −1.93 |
| 1.01 ..... | 2.66 | 1.97 | 1.23 | 0.70 | 0.54 | 0.33 | 0.02 | −0.15 | −1.22 | −1.49 | −1.96 |

TABLE 31

MULTI-INSTRUMENT COLORS OF THE Im TEMPLATE FROM BENÍTEZ ET AL. (2004) IN THE HRC SYSTEM (AB MAG) AND WFC F606W (AB MAG)

| $z$ | $H_{F220W}-W_{F606W}$ | $H_{F250W}-W_{F606W}$ | $H_{F330W}-W_{F606W}$ | $H_{F435W}-W_{F606W}$ | $H_{F475W}-W_{F606W}$ | $H_{F555W}-W_{F606W}$ | $H_{F606W}-W_{F606W}$ | $H_{F625W}-W_{F606W}$ | $H_{F775W}-W_{F606W}$ | $H_{F814W}-W_{F606W}$ | $H_{F850LP}-W_{F606W}$ |
|---|---|---|---|---|---|---|---|---|---|---|---|
| 0.01 ..... | 1.41 | 1.34 | 1.12 | 0.36 | 0.18 | 0.06 | 0.00 | −0.03 | −0.20 | −0.24 | −0.32 |
| 0.06 ..... | 1.38 | 1.32 | 1.15 | 0.43 | 0.19 | 0.05 | 0.00 | −0.03 | −0.21 | −0.24 | −0.33 |
| 0.11 ..... | 1.36 | 1.30 | 1.17 | 0.50 | 0.27 | 0.05 | 0.00 | −0.04 | −0.21 | −0.25 | −0.34 |
| 0.16 ..... | 1.34 | 1.27 | 1.18 | 0.59 | 0.33 | 0.07 | 0.00 | −0.08 | −0.22 | −0.26 | −0.36 |
| 0.21 ..... | 1.33 | 1.23 | 1.16 | 0.68 | 0.39 | 0.10 | 0.01 | −0.10 | −0.23 | −0.27 | −0.37 |
| 0.26 ..... | 1.33 | 1.20 | 1.13 | 0.76 | 0.45 | 0.15 | 0.01 | −0.11 | −0.23 | −0.28 | −0.39 |
| 0.31 ..... | 1.32 | 1.17 | 1.10 | 0.87 | 0.51 | 0.18 | 0.01 | −0.13 | −0.24 | −0.29 | −0.41 |
| 0.36 ..... | 1.30 | 1.13 | 1.05 | 0.86 | 0.55 | 0.21 | 0.01 | −0.15 | −0.26 | −0.32 | −0.44 |
| 0.41 ..... | 1.28 | 1.08 | 0.99 | 0.84 | 0.59 | 0.25 | 0.02 | −0.13 | −0.35 | −0.38 | −0.48 |
| 0.46 ..... | 1.21 | 1.00 | 0.88 | 0.77 | 0.57 | 0.25 | 0.01 | −0.16 | −0.47 | −0.49 | −0.56 |
| 0.51 ..... | 1.18 | 0.95 | 0.81 | 0.72 | 0.59 | 0.28 | 0.01 | −0.19 | −0.52 | −0.54 | −0.60 |
| 0.56 ..... | 1.15 | 0.90 | 0.74 | 0.66 | 0.56 | 0.31 | 0.02 | −0.19 | −0.57 | −0.59 | −0.65 |
| 0.61 ..... | 1.12 | 0.86 | 0.68 | 0.60 | 0.51 | 0.32 | 0.02 | −0.18 | −0.61 | −0.64 | −0.70 |
| 0.66 ..... | 1.09 | 0.82 | 0.61 | 0.53 | 0.47 | 0.34 | 0.02 | −0.17 | −0.64 | −0.68 | −0.77 |
| 0.71 ..... | 1.07 | 0.78 | 0.55 | 0.47 | 0.41 | 0.30 | 0.02 | −0.16 | −0.65 | −0.72 | −0.86 |
| 0.76 ..... | 1.04 | 0.75 | 0.49 | 0.40 | 0.36 | 0.26 | 0.02 | −0.13 | −0.66 | −0.76 | −0.93 |
| 0.81 ..... | 1.03 | 0.72 | 0.45 | 0.34 | 0.30 | 0.23 | 0.01 | −0.11 | −0.67 | −0.79 | −0.97 |
| 0.86 ..... | 1.02 | 0.70 | 0.41 | 0.28 | 0.25 | 0.19 | 0.01 | −0.10 | −0.69 | −0.81 | −1.01 |
| 0.91 ..... | 1.00 | 0.66 | 0.36 | 0.22 | 0.19 | 0.13 | 0.01 | −0.06 | −0.72 | −0.84 | −1.05 |
| 0.96 ..... | 1.01 | 0.66 | 0.35 | 0.18 | 0.15 | 0.10 | 0.01 | −0.06 | −0.69 | −0.81 | −1.06 |
| 1.01 ..... | 1.04 | 0.68 | 0.35 | 0.16 | 0.13 | 0.09 | 0.01 | −0.05 | −0.63 | −0.76 | −1.04 |

TABLE 32

MULTI-INSTRUMENT COLORS OF THE E/So TEMPLATE FROM BENÍTEZ ET AL. (2004) IN THE LANDOLT SYSTEM (VEGAMAG) AND WFC F606W (VEGAMAG)

| $z$ | $U-$F606W | $B-$F606W | $V-$F606W | $R-$F606W | $I-$F606W |
|---|---|---|---|---|---|
| 0.01 ..... | 1.57 | 1.14 | 0.27 | −0.33 | −0.89 |
| 0.06 ..... | 1.65 | 1.30 | 0.27 | −0.34 | −0.94 |
| 0.11 ..... | 1.74 | 1.46 | 0.26 | −0.36 | −1.00 |
| 0.16 ..... | 1.86 | 1.61 | 0.27 | −0.38 | −1.04 |
| 0.21 ..... | 2.02 | 1.72 | 0.31 | −0.42 | −1.10 |
| 0.26 ..... | 2.22 | 1.80 | 0.37 | −0.47 | −1.17 |
| 0.31 ..... | 2.43 | 1.86 | 0.46 | −0.51 | −1.23 |
| 0.36 ..... | 2.65 | 1.90 | 0.56 | −0.54 | −1.31 |
| 0.41 ..... | 2.87 | 1.96 | 0.64 | −0.55 | −1.37 |
| 0.46 ..... | 3.03 | 2.01 | 0.68 | −0.57 | −1.44 |
| 0.51 ..... | 3.09 | 2.06 | 0.67 | −0.58 | −1.56 |
| 0.56 ..... | 3.05 | 2.12 | 0.62 | −0.61 | −1.68 |
| 0.61 ..... | 2.96 | 2.19 | 0.57 | −0.64 | −1.81 |
| 0.66 ..... | 2.86 | 2.28 | 0.53 | −0.66 | −1.91 |
| 0.71 ..... | 2.78 | 2.36 | 0.51 | −0.68 | −1.99 |
| 0.76 ..... | 2.70 | 2.41 | 0.49 | −0.72 | −2.07 |
| 0.81 ..... | 2.65 | 2.47 | 0.51 | −0.73 | −2.09 |
| 0.86 ..... | 2.66 | 2.54 | 0.60 | −0.70 | −2.03 |
| 0.91 ..... | 2.65 | 2.57 | 0.69 | −0.69 | −1.97 |
| 0.96 ..... | 2.59 | 2.55 | 0.76 | −0.70 | −1.95 |
| 1.01 ..... | 2.54 | 2.53 | 0.85 | −0.71 | −1.93 |

TABLE 33

MULTI-INSTRUMENT COLORS OF THE Sbc TEMPLATE FROM BENÍTEZ ET AL. (2004) IN THE LANDOLT SYSTEM (VEGAMAG) AND WFC F606W (VEGAMAG)

| $z$ | $U-$F606W | $B-$F606W | $V-$F606W | $R-$F606W | $I-$F606W |
|---|---|---|---|---|---|
| 0.01 ..... | 0.96 | 0.88 | 0.22 | −0.29 | −0.79 |
| 0.06 ..... | 1.15 | 0.97 | 0.22 | −0.30 | −0.83 |
| 0.11 ..... | 1.30 | 1.07 | 0.22 | −0.31 | −0.86 |
| 0.16 ..... | 1.42 | 1.19 | 0.23 | −0.32 | −0.89 |
| 0.21 ..... | 1.50 | 1.31 | 0.24 | −0.34 | −0.92 |
| 0.26 ..... | 1.52 | 1.42 | 0.26 | −0.37 | −0.96 |
| 0.31 ..... | 1.49 | 1.52 | 0.29 | −0.40 | −1.02 |
| 0.36 ..... | 1.46 | 1.60 | 0.34 | −0.42 | −1.06 |
| 0.41 ..... | 1.40 | 1.65 | 0.40 | −0.45 | −1.11 |
| 0.46 ..... | 1.34 | 1.66 | 0.45 | −0.48 | −1.17 |
| 0.51 ..... | 1.25 | 1.64 | 0.49 | −0.50 | −1.24 |
| 0.56 ..... | 1.16 | 1.60 | 0.53 | −0.53 | −1.32 |
| 0.61 ..... | 1.06 | 1.53 | 0.55 | −0.55 | −1.41 |
| 0.66 ..... | 0.96 | 1.46 | 0.57 | −0.55 | −1.49 |
| 0.71 ..... | 0.85 | 1.36 | 0.57 | −0.57 | −1.57 |
| 0.76 ..... | 0.74 | 1.26 | 0.55 | −0.58 | −1.64 |
| 0.81 ..... | 0.63 | 1.17 | 0.51 | −0.58 | −1.70 |
| 0.86 ..... | 0.54 | 1.08 | 0.48 | −0.57 | −1.73 |
| 0.91 ..... | 0.47 | 1.00 | 0.43 | −0.55 | −1.74 |
| 0.96 ..... | 0.41 | 0.93 | 0.39 | −0.53 | −1.73 |
| 1.01 ..... | 0.37 | 0.87 | 0.35 | −0.50 | −1.71 |

TABLE 34
MULTI-INSTRUMENT COLORS OF THE Im TEMPLATE FROM BENÍTEZ ET AL. (2004) IN THE LANDOLT SYSTEM (VEGAMAG) AND WFC F606W (VEGAMAG)

| $z$ | $U-$F606W | $B-$F606W | $V-$F606W | $R-$F606W | $I-$F606W |
|---|---|---|---|---|---|
| 0.01 ..... | 0.18 | 0.52 | 0.13 | −0.18 | −0.56 |
| 0.06 ..... | 0.34 | 0.57 | 0.09 | −0.17 | −0.57 |
| 0.11 ..... | 0.43 | 0.65 | 0.09 | −0.17 | −0.58 |
| 0.16 ..... | 0.46 | 0.73 | 0.12 | −0.22 | −0.58 |
| 0.21 ..... | 0.47 | 0.82 | 0.15 | −0.24 | −0.59 |
| 0.26 ..... | 0.46 | 0.90 | 0.18 | −0.25 | −0.60 |
| 0.31 ..... | 0.44 | 0.96 | 0.21 | −0.25 | −0.61 |
| 0.36 ..... | 0.40 | 1.00 | 0.21 | −0.27 | −0.63 |
| 0.41 ..... | 0.34 | 1.00 | 0.24 | −0.29 | −0.67 |
| 0.46 ..... | 0.24 | 0.94 | 0.25 | −0.34 | −0.79 |
| 0.51 ..... | 0.17 | 0.90 | 0.29 | −0.37 | −0.88 |
| 0.56 ..... | 0.10 | 0.85 | 0.32 | −0.39 | −0.94 |
| 0.61 ..... | 0.03 | 0.79 | 0.34 | −0.38 | −1.00 |
| 0.66 ..... | −0.04 | 0.73 | 0.34 | −0.37 | −1.05 |
| 0.71 ..... | −0.11 | 0.67 | 0.33 | −0.36 | −1.05 |
| 0.76 ..... | −0.17 | 0.61 | 0.31 | −0.35 | −1.04 |
| 0.81 ..... | −0.23 | 0.55 | 0.28 | −0.33 | −1.06 |
| 0.86 ..... | −0.28 | 0.49 | 0.24 | −0.32 | −1.08 |
| 0.91 ..... | −0.34 | 0.43 | 0.19 | −0.32 | −1.10 |
| 0.96 ..... | −0.36 | 0.39 | 0.17 | −0.30 | −1.11 |
| 1.01 ..... | −0.36 | 0.37 | 0.16 | −0.27 | −1.08 |

TABLE 35
S/N CALCULATION FOR DIFFERENT APERTURE RADII FOR WFC/F606W

| APERTURE RADIUS | | AREA | EE | SIGNAL | MAIN NOISE SOURCES (ADU) | | | OTHER NOISE (%) | | | |
|---|---|---|---|---|---|---|---|---|---|---|---|
| Pixels | Arcsec | (pixels) | (%) | (ADU) | Source | Read Noise | Background | Breathing | Aperture Correction | TOTAL NOISE | S/N |
| 1 ..... | 0.05 | 3.1 | 31.30 | 313.0 | 17.7 | 4.0 | 5.6 | 0.05 | 0.07 | 28.1 | 11.1 |
| 2 ..... | 0.10 | 12.6 | 65.60 | 656.0 | 25.6 | 7.9 | 11.2 | 0.04 | 0.03 | 37.9 | 17.3 |
| 3 ..... | 0.15 | 28.3 | 79.60 | 796.0 | 28.2 | 11.9 | 16.8 | 0.03 | 0.02 | 36.3 | 22.0 |
| 4 ..... | 0.20 | 50.3 | 84.50 | 845.0 | 29.1 | 15.9 | 22.4 | 0.02 | 0.02 | 35.6 | 23.7 |
| 5 ..... | 0.25 | 78.5 | 87.10 | 871.0 | 29.5 | 19.8 | 28.0 | 0.01 | 0.01 | 37.9 | 23.0 |
| 6 ..... | 0.30 | 113.1 | 89.00 | 890.0 | 29.8 | 23.8 | 33.6 | 0.00 | 0.01 | 43.0 | 20.7 |
| 7 ..... | 0.35 | 153.9 | 90.00 | 900.0 | 30.0 | 27.7 | 39.2 | 0.00 | 0.01 | 49.5 | 18.2 |
| 8 ..... | 0.40 | 201.1 | 90.80 | 908.0 | 30.1 | 31.7 | 44.8 | 0.00 | 0.01 | 56.1 | 16.2 |
| 9 ..... | 0.45 | 254.5 | 91.40 | 914.0 | 30.2 | 35.7 | 50.4 | 0.00 | 0.01 | 62.8 | 14.6 |
| 10 ..... | 0.50 | 314.2 | 92.00 | 920.0 | 30.3 | 39.6 | 56.0 | 0.00 | 0.01 | 69.5 | 13.2 |
| 15 ..... | 0.75 | 706.8 | 94.10 | 941.0 | 30.7 | 59.4 | 84.1 | 0.00 | 0.01 | 103.4 | 9.1 |
| 20 ..... | 1.00 | 1256.6 | 95.20 | 952.0 | 30.9 | 79.3 | 112.1 | 0.00 | 0.00 | 137.6 | 6.9 |

NOTE.—For this simulation we assumed a flux of 1000 $e$ in the infinite aperture and a background level of 10 $e$.

## APPENDIX F

## OPTIMAL APERTURE SIZE

There are several factors to take into account when selecting the size of the aperture when measuring the flux of stars. For stellar photometry, the largest S/Ns (i.e., the smallest photometric errors) are generally obtained with relatively small apertures (Howell 1989). Large apertures can have large photometric errors when the total signal from the source become comparable to the total background signal. They also can suffer from measurement errors arising from the back-

ground flux. On the other hand, very small apertures can suffer from small-number statistics because of the low measured signal.

There are a number of trade-offs to consider when selecting the optimal aperture size. The signal level of the source and the background noise are the main components. However, several other factors can also impact the choice of the aperture radius, such as the PSF spatial variations, the EE profile, the read noise, and the crowding. In order to provide a more quantitative analysis of the various dependencies, we can develop a case study (detailed calculations are provided in Table 35). Consider an isolated star that, in a given exposure, produces ~1000 $e$ in an image taken with WFC F606W. The default gain is 1 $e^-$ $ADU^{-1}$ and the background (sky+dark current) is ~10 ADU. The read noise is ~5 $e^-$. We can predict the S/N in different aperture radii by calculating the fraction of source flux enclosed in the aperture area and the total noise associated with the measurement. The total noise is obtained by adding in quadrature the Poisson noise of the star signal, the read noise, the Poisson noise of the background signal, plus two more noise contributions. The first is related to breathing and focus variations on orbital timescales, which can cause small variations in the aperture corrections. As an initial estimate, we used the data published for WFPC2 (Suchkov & Casertano 1997). The second noise contribution, ~10% of the aperture correction, is related to uncertainties in the aperture correction and its variation due to the PSF spatial variation across the chip. In both cases, we express their impact as percentage of the source flux in the aperture. They are included in the noise calculation in the form of additional Poisson noise.

According to this simulation, the highest S/N is obtained with a 4 pixel aperture radius. Small variations from the optimal radius by $\pm 1$ pixel make little difference. We repeated the same test for the F435W and F850LP filter and we find similar results. The slightly larger PSF in the F850LP tends to produce the highest S/N at slightly larger apertures. The comparison for these filters is shown in Figure 28. A similar test for HRC shows that an aperture of 4–5 pixels is also the optimal choice for the HRC, where the effect of the broadening of the PSF in the near-IR is more evident (Fig. 29). Brighter stars have larger optimal aperture sizes than do fainter stars. For a point-source object with signal >20,000 ADU, the optimal choice is a radius of ~1″. If one must use only one aperture size, it is clearly advantageous to chose an aperture size that produces the smallest photometric errors for the sources of most scientific interest.

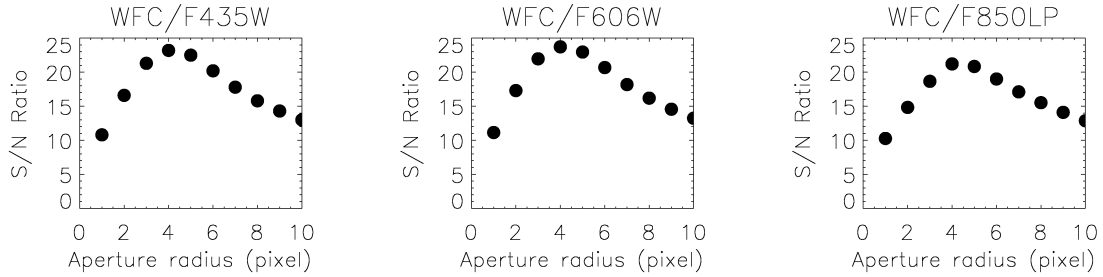


FIG. 28.—S/N as a function of the size of the photometric aperture for three filters in the WFC. A star that produces 1000 $e^-$ in the nominal infinite aperture and a background of 10 $e$ have been assumed for this test.

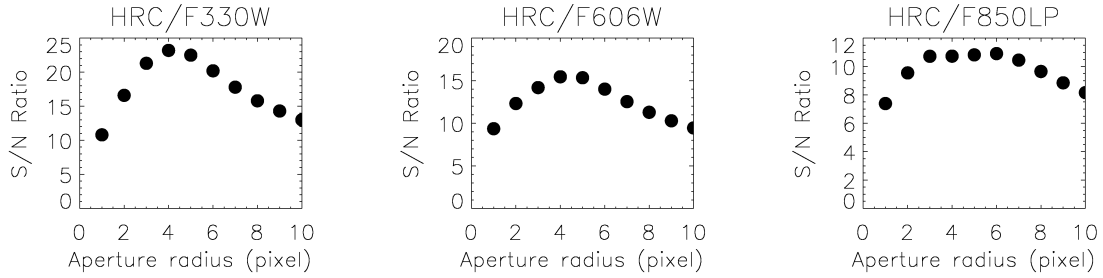


FIG. 29.—Same as Fig. 28, but for the HRC.

## REFERENCES


Anderson, J. 2002, in Proc. 2002 *HST* Calibration Workshop, ed. S. Arribas et al. (Baltimore: STScI), 13

Anderson, J., & King, I. 2004, Instrument Science Report (ACS 04-15; Baltimore: STScI)

Baggett, S., Casertano, S., Gonzaga, S., & Ritchie, C. 1997, Instrument Science Report (WFCP2 97-10; Baltimore: STScI)

Baggett, S., et al. 2001, Instrument Science Report (WFPC2 01-06; Baltimore: STScI)

Bedin, L. R., Cassisi, S., Castelli, F., Piotto, G., Anderson, J., Salaris, M., Momany, Y., & Pietrinferni, A. 2004, MNRAS, 357, 1038

Benítez, N. 2000, ApJ, 536, 571

Benítez, N., et al. 2004, ApJS, 150, 1 (B2004)

Bertin, E., & Arnouts, S. 1996, A&AS, 117, 393

Bessel, M. S. 1983, PASP, 95, 480

———. 1990, PASP, 102, 1181

Blakeslee, J. P., Anderson, K. R., Meurer, G. R., Benítez, N., & Magee, D. 2003a, in ASP Conf. Ser. 295, Astronomical Data Analysis Software and Systems XII, ed. H. E. Payne et al. (San Francisco: ASP), 257

Blakeslee, J. P., et al. 2003b, ApJ, 596, L143

Boffi, F., De Marchi, G., & Bohlin, R. C. 2004, Instrument Science Report (ACS 04-05; Baltimore: STScI)

Bohlin, R. C., & Gilliland, R. 2004, AJ, 127, 3508

Bohlin, R. C., Harris, A. W., Holm, A. V., & Gry, C. 1990, ApJS, 73, 413

Bohlin, R. C., Hartig, G. F., & Sparks, Wm. 2002, Instrument Science Report (ACS 02-03; Baltimore: STScI)

Bohlin, R. C., Hartig, G. F., & Tzvetanov, Z. 2001, Instrument Science Report (ACS 00-10; Baltimore: STScI)

Bohlin, R. C., Wheeler, T., & Mack, J. 2003, Instrument Science Report (ACS 03-11; Baltimore: STScI)

Bruzual, C., & Charlot, S. 2003, MNRAS, 344, 1000

Buser, R., & Kurucz, R. L. 1978, A&A, 70, 555

Cardelli, J. A., Clayton, G. C., & Mathis, J. S. 1989, ApJ, 345, 245

Casertano, S., & Wiggs, M. S. 2001, Instrument Science Report, (WFPC2 01-10; Baltimore: STScI)

Cawley, L., Goudfooij, P., Withmore, B., Stiavelli, M., & CTE Working Group 2001, Instrument Science Report (WFC3 01-05; Baltimore: STScI)

Clampin, M., et al. 1998, Proc. SPIE, 3356, 332

———. 2002, in Proc. 2002 *HST* Calibration Workshop 3, ed. S. Arribas et al. (Baltimore: STScI)

Coleman, G. D., Wu, C. C., & Weedman, D. W. 1980, ApJS, 43, 393

Colina, L., Bohlin, R., & Castelli, F. 1996, Instrument Science Report (CAL/SCS-008; Baltimore: STScI)

De Marchi, G., et al. 2004, Instrument Science Report (ACS 04-08; Baltimore: STScI)

Dolphin, A. E. 2000a, PASP, 112, 1383

———. 2000b, PASP, 112, 1397

Ford, H. C., et al. 1996, Proc. SPIE, 2807, 184

———. 1998, Proc. SPIE, 3356, 234

———. 2002, Proc. SPIE, 4854, 81

Fruchter, A. S., & Hook, R. N. 2002, PASP, 114, 144

Giavalisco, M. 2004a, Cross-Talk in the ACS WFC Detectors. I: Description of the Effect (ACS ISR04-12; Baltimore: STScI)

———. 2004b, Cross-Talk in the ACS WFC Detectors. II: Using GAIN = 2 to Minimize the Effect (ACS ISR04-13; Baltimore: STScI)

Gilliland, R. L. 2004, Instrument Science Report (ACS 04-01; Baltimore: STScI)

Gilliland, R. L., & Riess, A. 2002, in Proc. 2002 *HST* Calibration Workshop, ed. S. Arribas et al. (Baltimore: STScI), 61

Girardi, L., Bertelli, G., Bressan, A., Chiosi, C., Groenewegen, M. A. T., Marigo, P., Salasnich, B., & Weiss, A. 2002, A&A, 391, 195

Goudfrooij, P., & Kimble, R. A. 2002, in Proc. 2002 *HST* Calibration Workshop, ed. S. Arribas et al. (Baltimore: STScI), 105

Hack, W. J., Busko, I., & Jedrzejewski, R. I. 2003 in ASP Conf. Ser.295, Astronomical Data Analysis Software and Systems XII, ed. H. E. Payne, R. I., Jedrzejewski, & R. N. Hook (San Francisco: ASP), 453

Hack, W. J., & Greenfield, P. 2000, in ASP Conf. Ser. 216, Astronomical Data Analysis Software and Systems IX, ed. N. Manset et al. (San Francisco: ASP), 433

Harris, W. E., et al. 1997, AJ, 114, 1030

Hartig, G. F., Krist, J. E., Martel, A. R., Ford, H. C., & Illingworth, G. D. 2003, Proc. SPIE, 4854, 532

Hayes, D. S. 1985, in Proc. IAU Symp. 111, Calibration of Fundamental Stellar Quantities, ed. D. S. Hayes et al. (Dordrecht: Reidel), 225

Heyer, I., Richardson, M., Whitmore, B. C., & Lubin, L. M. 2002, in Proc. 2002 *HST* Calibration Workshop, ed. S. Arribas et al. (Baltimore: STScI), 333

———. 2004, Instrument Science Report (WFPC2 04-01; Baltimore: STScI)

Högbom, J. A. 1974, A&AS, 15, 417

Holtzman, J. A., et al. 1995, PASP, 107, 156

Hopkinson, G. R. 1991, in Proc. ESA Electronic Components Conf. (ESA SP-313; Paris: ESA), 301

Howell, S. B. 1989, PASP, 101, 616

Janesick, J. R. 2001, Scientific Charge-Coupled Devices (Bellingham: SPIE Press)

Janesick, J. R., Soli, G., Elliot, T., & Collins, S. 1991, Proc. SPIE, 1447, 87

Kimble, R. A., et al. 1998, Proc. SPIE, 3356, 188

Kinney, A. L., et al. 1996, ApJ, 467, 38

Koekemoer, A. M., Fruchter, A. S., Hook, R., & Hack, W. 2002, in Proc. 2002 *HST* Calibration Workshop, ed. S. Arribas et al. (Baltimore: STScI), 337

Koorneef, J., Bohlin, R., Buser, R., Horne, K., & Turnshek, D. 1986, in Proc. Nineteenth IAU General Assembly, ed. S.-P. Swinggs (Dordrecht: Reidel)

Krist, J. E. 2003a, Instrument Science Report (ACS 2003-06; Baltimore: STScI)

Krist, J. E., Hartig, G. F., Clampin, M., Golimowski, D. A., Ford, H. C., & Illingworth, G. D. 2003b, Proc. SPIE, 4860, 20

Kurucz, R. L. 1993, CD-ROM 13, ATLAS 9 Stellar Atmosphere Programs and 2 km/s Grid (Cambridge: SAO)

Mack, J., Bohlin, R. C., Gilliland, R. L., van der Marel, R., Blakeslee, J. P., & De Marchi, G. 2002a, Instrument Science Report (ACS 02-08; Baltimore: STScI)

Mack, J., Bohlin, R. C., Gilliland, R. L., van der Marel, R., De Marchi, G., & Blakeslee, J. P. 2002b, Proc. 2002 *HST* Calibration Workshop, ed. S. Arribas et al. (Baltimore: STScI), 23

Madau, P. 1995, ApJ, 441, 18

Maíz-Apellániz, J. 2002. Proc. 2002 *HST* Calibration Workshop, ed. S. Arribas et al. (Baltimore: STScI), 346

Manfroid, J., & Sterken, C. 1992, A&A, 258, 600

Manfroid, J., Sterken, C., & Gosset, E. 1992, A&A, 264, 345

Martel, A. R., & Hartig, G. F. 2001 (Baltimore: Johns Hopkins Univ.), http://acs.pha.jhu.edu/instrument/calibration/results/by_item/flat_fields/internal_lamps/d2tung

Martel, A. R., Hartig, G. F., & Sirianni, M. 2001a, WFC#4: Gain, Noise, Linearity, Saturation (Baltimore: Johns Hopkins University), http://acs.pha.jhu.edu/instrument/calibration/results/by_item/detector/wfc/build4/gain
———. 2001b, HRC#1: Gain, Noise, Linearity, Saturation (Baltimore: Johns Hopkins University), http://acs.pha.jhu.edu/instrument/calibration/results/by_item/detector/hrc/build1/gain
Meurer, G. R., et al. 2002, in Proc. 2002 *HST* Calibration Workshop, ed. S. Arribas et al. (Baltimore: STScI), 65
———. 2003, Proc. SPIE, 4854, 507
Michard, R. 2002, A&A, 384, 763
Mutchler, M., & Sirianni, M. 2005, Instrument Science Report (ACS 05-03; Baltimore: STScI)
Mutchler, M., Sirianni, M., Van Orsow, D., & Riess, A. 2004, Instrument Science Report (ACS-ISR04-07; Baltimore: STScI)
Oke, J. B. 1964, ApJ, 140, 689
Pavlovsky, C., et al. 2004, ACS Instrument Handbook, Ver. 5.0 (Baltimore: STScI) (AIHv5)
———. 2005, ACS Data Handbook, Ver. 4.0 (Baltimore: STScI) (ADHv4)
Pietrinferni, A., Cassisi, S., Salaris, M., & Castelli, F. 2004, ApJ, 612, 168
Quijano, K. J., et al. 2003, STIS Instrument Handbook, Ver. 7.0 (Baltimore: STScI)
Riess, A., 2000, Instrument Science Report (WFPC2 00-04; Baltimore: STScI)
———. 2002a, Instrument Science Report (ACS 02-07; Baltimore: STScI)
———. 2002b, in Proc. 2002 *HST* Calibration Workshop, ed. S. Arribas et al. (Baltimore : STScI), 47
———. 2003, Instrument Science Report (ACS 03-09; Baltimore: STScI)
Riess, A., & Mack, J. 2004, Instrument Science Report (ACS 03-06; Baltimore: STScI)
Saha, A., Dolphin, A. E., Thim, F., & Whitmore, B. 2005, PASP, 117, 37
Saha, A., Labhardt, L., & Prosser, C. 2000, PASP, 112, 163
Sirianni, M., & Clampin, M. 1999a, Device 98242MABR10-01 (Baltimore: Johns Hopkins University), http://acs.pha.jhu.edu/instrument/detectors/WFC/lot7b_1001/report1001.pdf
———. 1999b, Device 98242MABR10-02 (Baltimore: Johns Hopkins University), http://acs.pha.jhu.edu/instrument/detectors/WFC/lot7b_1002/report1002.pdf
Sirianni, M., De Marchi, G., Gilliland, R., Pavlovsky, C., & Mack, J. 2002a, in Proc. 2002 *HST* Calibration Workshop, ed. S. Arribas et al. (Baltimore: STScI), 31
Sirianni, M., Martel, A. R., & Hartig, G. F. 2001, WFC#4 Overscan Analysis and Bias Subtraction (Baltimore: Johns Hopkins University), http://acs.pha.jhu.edu/instrument/calibration/results/by_item/detector/wfc/build4/overscan
Sirianni, M., Martel, A. R., Jee, M. J., Van Orsow, D., & Sparks, W. B. 2002b in Proc. 2002 *HST* Calibration Workshop, ed. S. Arribas et al. (Baltimore: STScI), 82
Sirianni, M., Mutchler, M., Clampin, M., Ford, H. C., Illingworth, G., Hartig, G. F., Van Orsow, D., & Wheeler, T. 2004, Proc. SPIE, 5499, 173
Sirianni, M., Mutchler, M., & Lucas, R. 2005, ACS Instrument Science Report (Baltimore: STScI), in press
Sirianni, M., et al. 1998, Proc. SPIE, 3355, 608
———. 2000, Proc. SPIE, 4008, 669
———. 2003, Proc. SPIE, 4854, 496
Sterken, C., & Manfroid, J. 1992, Astronomical Photometry, A Guide (Dordrecht: Kluwer)
Stetson, P. B. 1992, JRASC, 86, 71
———. 1998, PASP, 110, 1448
Suchkov, A., & Casertano, S. 1997, in Proc. 1997 *HST* Calibration Workshop, ed. S. Casertano et al. (Baltimore: STScI), 378
Tonry, J. L., Blakeslee, J. P., Ajhar, E. A., & Dressler, A. 1997, ApJ, 475, 399
Tonry, J. L., Dressler, A., Blakeslee, J. P., Ajhar, E. A., Fletcher, A., Luppino, G. A., Metzger, M. R., & Moore, C. B. 2001, ApJ, 546, 681
Tran, H. D., et al. 2002a, Proc. SPIE, 4854, 686
———. 2002b, in Proc. 2002 *HST* Calibration Workshop, ed. S. Arribas et al. (Baltimore: STScI), 86
van der Marel, R. 2003, Instrument Science Report (ACS 03-10; Baltimore: STScI)
Walsh, J. R., Freudling, W., Pirzkal, N., & Pasquali, A. 2003, Instrument Science Report (ACS 03-12; Baltimore: STScI)
Walsh, J. R., Pirzkal, N., & Pasquali, A. 2002, in Proc. 2002 *HST* Calibration Workshop, ed. Arribas et al. (Baltimore: STScI), 90
Whitmore, B., & Heyer, I. 2002, Instrument Science Report (WFPC2 02-03; Baltimore: STScI)
Whitmore, B., Heyer, I., & Casertano, S. 1999, PASP, 111, 1559
Young, A. T. 1992a, in ASP Conf. Ser. 28, Automated Telescope for Photometry and Imaging, ed. S. J. Adelman et al. (San Francisco: ASP), 73
———. 1992b, A&A, 257, 366
———. 1993, in Precision Photometry, ed. D. Kilkenny et al. (Cape Town: SAAO), 25
———. 1994, A&A, 288, 683
Zoccali, M., et al. 2001, ApJ, 553, 733